

# **Surface-Micromachined Capacitive Accelerometers in Above-IC Integration Methods**

By

Ahmad Alfaifi

Electrical and Computer Engineering Department

McGill University, Montreal

2017



A thesis submitted to McGill University in partial fulfillment of the requirements  
of the degree of Doctor of Philosophy

©Ahmad Alfaifi, 2017

To my family

# Table of Contents

Table of Contents .....	iii
Abstract .....	vii
Sommaire.....	ix
Acknowledgements .....	xi
List of Abbreviations.....	xiii
Chapter 1     Introduction .....	14
1.1     Preface .....	14
1.2     Thesis Organization.....	16
1.3     MEMS and IC Integration .....	16
1.4     Motivation .....	20
1.5     Research Goals .....	21
1.6     Contributions .....	22
1.6.1     Accelerometer Designs Optimization in 2D Fabrication Processes .....	22
1.6.2     Novel Dual-Axis Capacitive Accelerometers with Low Cross-Axis Sensitivity ..	22
1.6.3     In-Plane Capacitive Accelerometer in a 3D Surface Micromachining Process ....	23
1.6.4     3D Surface Micromachining Process for Above-IC Integration .....	23
1.7     References .....	24
Chapter 2     Overview of Accelerometers .....	26
2.1     Introduction .....	26
2.2     Historical Background.....	27
2.3     Types of Accelerometers .....	28
2.3.1     Force Balance Accelerometers .....	30
2.3.2     Deflection Accelerometers .....	30
2.4     Accelerometers' Performance Characterization.....	31
2.5     Sensing Mechanisms in MEMS Accelerometers .....	33
2.5.1     Piezoelectric Accelerometers .....	33
2.5.2     Piezoresistive Accelerometers .....	34
2.5.3     Capacitive Accelerometers .....	35
2.5.4     Performance Assessment.....	35
2.6     MEMS Capacitive Accelerometers .....	36
2.7     MEMS Accelerometer Applications .....	38
2.8     MEMS Accelerometer Market Review .....	40

2.8.1	Safran Colibrys SA Single-Axis Tactical-Grade Accelerometer .....	41
2.8.2	mCube 3-Axis Accelerometer for Consumer Applications.....	41
2.9	Conclusion.....	42
2.10	References .....	42
Chapter 3	Accelerometer Design Optimization in 2D Fabrication Processes.....	45
3.1	Introduction .....	45
3.2	Model Derivation.....	46
3.3	Accelerometer Design and Fabrication Process .....	49
3.4	Method Verification .....	51
3.5	Discussion .....	54
3.6	Conclusion.....	55
3.7	References .....	55
Chapter 4	Dual-Axis Capacitive Accelerometer with Low Cross-Sensitivity .....	57
4.1	Introduction .....	57
4.2	Design Overview .....	59
4.3	Device Fabrication.....	63
4.4	Device Characterization .....	66
4.4.1	Simulation Results.....	66
4.4.2	The Test Setup and Digital Interface Integration .....	69
4.4.3	Test Results .....	71
4.5	Discussion .....	72
4.6	Conclusion.....	74
4.7	References .....	75
Chapter 5	In-Plane Capacitive Accelerometer in a 3D Surface Micromachining Process ....	77
5.1	Introduction .....	77
5.2	Accelerometer Design Model.....	79
5.2.1	Capacitances .....	80
5.2.2	Proof Mass and Sensitivity.....	81
5.2.3	Enhanced 3D Suspension Beam.....	82
5.2.4	Noise Analysis and Optimum Gap .....	88
5.2.5	Bandwidth and Damping Ratio .....	90
5.3	Accelerometer Design .....	92
5.3.1	Target Specifications .....	92

5.3.2	Design Process.....	93
5.4	Device Fabrication.....	96
5.5	Accelerometer Testing.....	99
5.6	Discussion .....	101
5.7	Design Improvements.....	102
5.7.1	Addition of Mechanical Stoppers .....	102
5.7.2	Closed-Loop System Design .....	103
5.8	Conclusion.....	104
5.9	References .....	105
Chapter 6	3D Surface Micromachining Process for Above-IC Integration .....	109
6.1	Introduction .....	109
6.2	Materials Selection .....	111
6.3	Process Flow.....	113
6.4	Resolving Fabrication Challenges and Issues .....	117
6.4.1	Platforms Detaching and Unwanted Etching.....	118
6.4.2	Unetched Structural Layer on the Platforms' Sidewalls.....	119
6.4.3	Increased Spacing on the Platforms and CD Degrade.....	121
6.5	Comparison with Other 3D Surface Micromachining Processes .....	123
6.6	Process Improvement by Chaining its Parameters .....	124
6.7	Conclusion.....	125
6.8	References .....	125
Chapter 7	Conclusion.....	128
7.1	Summary .....	128
7.2	Future Development.....	129
7.2.1	2D Single-Axis Capacitive Accelerometers .....	129
7.2.2	2D Dual-Axis Capacitive Accelerometers .....	129
7.2.3	3D Single-Axis Capacitive Accelerometers .....	130
7.2.4	3D Fabrication Process.....	130
7.3	References .....	131
Appendix A	Characterization and Test Setup of the Capacitive Accelerometers.....	132
A.1	Introduction .....	132
A.2	System Overview.....	134
A.3	System Design .....	136

A.3.1	PC Communications and Logging Tool .....	136
A.3.2	PCB Design .....	137
A.3.3	Data Filtering.....	138
A.3.4	Arduino Code .....	140
A.4	References .....	141

# Abstract

This thesis proposes a methodology to optimize the design of capacitive accelerometers. This is achieved through a systematic improvement procedure of the closing-gaps accelerometers design. This is used to find the optimum electrode dimensions that would result in the highest sensitivity, within a specified area. The method is verified through the simulation and fabrication of different variations of two designs, then comparing the results with the expected values from analytical optimization methods. The prototypes are fabricated in a commercial process, which imposed limitations on the sizes of the possible accelerometer designs. A survey of prior published works shows the importance of the optimization technique suggested here to increase the performance of these types of sensors, when no fabrication restrictions exist.

The thesis also introduces a novel low cross-sensitivity dual-axis capacitive accelerometer design. The device is fabricated in a silicon-on-insulator (SOI) process and its fabrication is finalized by an in-house release step. The device measures  $1\text{ mm} \times 1\text{ mm}$ , with four (4) proof masses that are able to sense accelerations in the X- and Y-axes independently. Two commercial capacitance-to-digital converters are used to read the outputs of both axes of the device in a system in package implementation. The fabricated device exhibits a sensitivity of 16.83 fF/g, while keeping the measured cross-sensitivity to less than 1 % throughout the  $\pm 4\text{ g}$  linear range. The rotational motion and Z accelerations have no impact on the device X and Y readings, thanks to the device's particular geometry and differential nature.

In addition, the thesis presents a novel design of a 3D high-sensitivity lateral capacitive accelerometer. The accelerometer design utilizes the whole area of the sensor for both the sensing and proof masses, which cancels the tradeoff needed in conventional 2D designs. The design model of the accelerometer is developed to target the highest possible performance. A Z-shaped innovative design of the supporting beams is developed to limit the vertical displacement within the used submicron gap. The accelerometer measures  $500 \times 500\text{ }\mu\text{m}^2$  and achieves 58 fF/g sensitivity in a  $\pm 4\text{ g}$  range in an open-loop system. Suggestions are provided to decrease the 1.4 mg noise floor of the device.

Finally, the thesis describes a 3D surface micromachining platform process for above-IC integration. This method uses non-conductive materials with attractive mechanical properties to fabricate micro-electromechanical systems (MEMS) devices. The fixed structures are created using a polyimide layer, while the moving structures are built using silicon nitride (SiN). A 240-nm thin parylene-N polymer layer is used as a sacrificial layer to largely define the capacitive gaps and enable dry release. The photolithography steps are limited to four, in order to ensure a simple and low-cost process. The process has a thermal budget of 300 °C, which should be safe for processing above CMOS integrated circuits. While the used materials provide good results, this process is not limited to these specific materials, and others can be used if needed.



# Sommaire

Cette thèse propose une méthode pour optimiser la conception des accéléromètre capacitifs avec un interstice pouvant se fermer. La méthode peut être utilisée pour trouver les dimensions optimales qui permettent une sensibilité maximale dans une zone spécifiée. La méthode est vérifiée en simulant et en fabriquant différentes variantes de deux dispositifs et en comparant les résultats avec les valeurs obtenues de la méthode d'optimisation analytique. Les variations sont fabriquées dans un processus commercial, ce qui limite le nombre et la taille des dispositifs testés. Une revue des travaux publiés montre l'importance de l'optimisation pour augmenter les performances de ces dispositifs dans le cas où aucune restriction de fabrication n'existe.

La thèse présente également un nouveau concept d'accéléromètre capacitif à double axe et à faible sensibilité croisée. Le dispositif est fabriqué dans un procédé d'oxyde sur silicium (SOI) et sa fabrication est finalisée par une étape de relâche dans nos laboratoires. Le dispositif mesure 1 mm x 1 mm et a quatre masses capables de détecter les accélérations dans les axes X et Y indépendamment. Deux convertisseurs de capacité numériques commerciaux sont utilisés pour lire les sorties des deux axes du dispositif dans un système mis en boîtier. Le dispositif fabriqué présente une sensibilité de 16,83 fF / g tout en maintenant la sensibilité croisée mesurée à moins de 1% dans la gamme linéaire de  $\pm 4$  g. Le mouvement de rotation et les accélérations en Z n'ont aucun impact sur les lectures en X et en Y du dispositif. Cela est possible grâce à la géométrie particulière et à la nature différentielle de l'appareil.

De plus, la thèse présente un nouveau concept d'un accéléromètre capacitif latéral à haute sensibilité avec électrodes 3D. La conception de l'accéléromètre utilise toute la surface du capteur pour la détection du mouvement de la masse, ce qui mitige le compromis typiquement nécessaire dans les dispositifs 2D. L'accéléromètre est développé pour cibler les performances les plus élevées possibles. Un design innovant en forme de Z des supports mécaniques est développé pour limiter le déplacement vertical dans l'interstice submicronique utilisé. L'accéléromètre mesure  $500 \times 500 \mu\text{m}^2$  et atteint 58 fF / g de

sensibilité dans une gamme  $\pm 4$  g dans un système de mesure à boucle ouverte. Des solutions sont suggérées pour diminuer le bruit de fond de 1,4 mg de l'appareil de mesure.

Finalement, la thèse décrit un processus de plate-forme de microfabrication en surface 3D pour intégration sur circuits intégrés. Cette méthode utilise des matériaux non conducteurs avec des propriétés mécaniques attrayantes pour la construction de dispositifs MEMS. Les plates-formes fixes sont créées à l'aide d'une couche de polyimide, tandis que la structure mobile est faite en nitrure de silicium. Une couche de parylène-N de 240 nm d'épaisseur est utilisée comme couche sacrificielle pour définir l'interstice capacitif et pour permettre la relâche à sec. Les étapes de photolithographie sont limitées à quatre pour assurer un processus simple. Le procédé a un budget thermique de 300 ° C, ce qui est adéquat pour l'intégration du procédé sur circuits intégrés. Bien que les matériaux utilisés fournissent de bon résultats, ce processus n'est pas limité à ceux-ci et d'autres matériaux peuvent être utilisés si nécessaire.

# Acknowledgements

First of all, I would like to thank Prof. Mourad N. El-Gamal for his great support during my studies at McGill University. He was such a great inspiration to me and his advice was always very helpful and to the point. He believed in me and increased my self-confidence in the research field to whole new levels that I would never have been able to reach without him.

I also would like to thank Prof. Frederic Nabki, who was always there when I needed advice in the design and fabrication stages. He encouraged and supported me to reach my limits and gave remarkable recommendations that helped me significantly. Moreover, I highly appreciate the information and recommendations given to me by my advisory committee Prof. Mourad N. El-Gamal, Prof. Dennis Giannacopoulos, and Prof. Mounir Boukadoum.

This research would not have been possible without the enormous help I received from my colleagues. I thank Dr. Karim Allidina, who transferred to me most of the knowledge in practical PCB design and integration to test my work. I also offer my deepest thanks to Dr. Mohannad El-Sayed, who never hesitated to offer precious advice and answer my questions during the fabrication stage. Furthermore, Prof. Paul-Vahé Cicek's help in the layout design and fabrication is greatly appreciated, as is Eng. Hani Tawfik's cooperation and help during fabrication.

I thank the King Abdulaziz City for Science and Technology (KACST) for the scholarship and for giving me the opportunity to pursue my graduate studies in some of the best graduate schools in the world. I also thank Dr. Abdul-Rahman Almuhanha for directing me since I joined KACST, and for his help and guidance before and during my graduate studies. I also very much appreciate the support of Dr. Ibrahim Alhomoudi of KACST.

Simulation tools and test fabrication in commercial processes were provided by the Canadian Microelectronics Corporation (CMC). I would also like to acknowledge the support of the Infrastructure of Nanostructures and Femtoscience (INF), the McGill Nanotool Microfab (MNM), NanoQAM, the Electronic Microsystems Assembly and

Encapsulation Laboratory (LASEM), and their staff for providing the fabrication, bonding, and characterization support and equipment.

# List of Abbreviations

ASIC	Application-Specific Integrated Circuit
BNEA	Brownian Noise Equivalent Acceleration
CDC	Capacitance to Digital Converter
CMOS	Complementary Metal-Oxide Semiconductor
CVD	Chemical Vapor Deposition
DUT	Device Under Test
EMI	Electro Magnetic Interference
ENIG	Electroless Nickel Immersion Gold
g	gravitational acceleration of the Earth
HID	Human Interface Device
I <sup>2</sup> C	Inter-Integrated Circuit (communication protocol)
IC	Integrated Circuit
IMU	Inertial Measurement Unit
IoT	Internet of Things
LCC	Leaded Chip Carrier
LSB	Least Significant Bit
MEMS	Micro Electro Mechanical System
MUMP <sup>®</sup>	Multi User MEMS Process
NEMS	Nano Electro Mechanical System
PCB	Printed Circuit Board
PECVD	Plasma Enhanced Chemical Vapor Deposition
RIE	Reactive Ion Etching
SEM	Scanning Electron Microscope
SiC	Silicon Carbide
SiN	Silicon Nitride
SiP	System in Package
SoC	System on Chip
SOI	Silicon on Insulator
UV	Ultra Violet

---

# Chapter 1

## Introduction

---

### 1.1 Preface

In the present information and automation era, human beings are leaning towards new technologies that help them monitor and control their lives. Smart systems are taking over the control of reading and analyzing data, to generate fused information for the end-user. These smart systems are used to promote ingenuity and safety in homes, transportation, industry, consumer electronics, etc. Micro electro mechanical systems (MEMS) are microscale smart systems that read a parameter of interest by converting one energy type (e.g. mechanical) to another that can be easily processed (e.g. electrical energy) [1, 2]. As the name suggests, MEMS use the electrical and mechanical properties of a device to interact with various types of parameters, directly and indirectly. For instance, bolometers detect infrared signals (optical) by using temperature-dependent resistive materials (thermo-mechanical). These devices have attractive features, starting from their small size to their low power consumption, making them some of the most ubiquitous technologies in our lives.

MEMS can be classified into three main categories according to their interaction with their environment [3]: first, the environmental sensors which are exposed directly to their environment to allow fast and reliable sensing, e.g. humidity sensors; second, the optical sensors that use transparent material to permit the chosen spectrum of light to reach the sensor, e.g., infrared detectors; finally, the inertial motion sensors which are used to detect motion, while enclosed and isolated in a closed-package. Occasionally, multiple sensors of one type are integrated within one package to provide full information to the system, e.g., humidity plus pressure sensors. This creates a virtuous cycle for combo sensors over discrete units, since it ultimately saves area and power, and simplifies data communication.

Inertial motion sensors are among the most successful MEMS devices sold worldwide today. For instance, they comprised more than one third of the MEMS market that was estimated at \$14 billion in 2016 [3]. These sensors provide information about tilt angle or motion acceleration (accelerometer), rotation speed (gyroscope), or the earth magnetic field (magnetometer). Their usage has spread across the automotive industry, entertainment systems, wearable electronics, and medical applications (Figure 1.1). As these applications grow and new ones emerge, new demands and specifications must be met, specifically in terms of size, power consumption, and performance. Heretofore, the MEMS development challenges mainly concerned consumer volume, cost, and size; in contrast, the forthcoming challenges are power consumption, more sensors fusion, and readiness for user applications [3]. Accelerometers are the most mature MEMS inertial sensors. They represent a highly competitive market that sold more than 80 million units (along with gyroscopes and their combos) in 2016, and this number is expected to double by 2018 [4].



(a) Crash detection [Chevrolet]



(b) Virtual reality headset [Oculus VR]



(c) Camera drone [DJI]



(d) Tablet computer [Apple Inc.]

Figure 1.1: Different applications that use accelerometers for motion detection

## **1.2 Thesis Organization**

This thesis details research conducted in developing MEMS capacitive accelerometers with high sensitivity, which can be built above their integrated circuits (IC). The remainder of this chapter discusses the motivation behind this work, based on the current technologies used in MEMS accelerometers' fabrication. It also specifies the research goals and the contributions of the research work reported here. Chapter 2 provides an overview of the accelerometers' principle of operation and sensing mechanisms in general. It then focuses on the MEMS accelerometers' different sensing types and explains why capacitive accelerometers were chosen for the work in this thesis. Subsequently, the different applications of accelerometers and their markets are briefly discussed. Chapters 3 and 4 present the research conducted on two-dimensional (2D) accelerometers. Chapter 3 describes a method to optimize the 2D design of capacitive accelerometers, and chapter 4 details a dual-axis accelerometer design in a commercial process. A novel three-dimensional (3D) single-axis accelerometer is presented in chapter 5, along with its design model. Next, chapter 6 describes the used 3D fabrication process and how it was developed to overcome the limitations present in its 2D counterparts. Finally, chapter 7 concludes the description of the research with a summary of the accomplished work and the possible future developments of the research topics. An appendix at the end of the thesis provides insight into the test setup and the electronics that were built to characterize the performance of the fabricated accelerometers.

## **1.3 MEMS and IC Integration**

One of the most important features of modern sensors is the integration of MEMS and IC's within one package. This promotes size reduction by co-deploying both components in one package, while preserving the quality of the signals because of the short interconnects between the two components. These electronic components are needed to acquire the signal, filter it, and send it through communication lines. The available MEMS and IC integration technologies use either hybrid multi-chip integration or monolithic system-on-chip (SoC) integration. The main reason to separate the MEMS and IC fabrication is because they often use different fabrication processes. Moreover, the



aluminum used in the IC wafer deteriorates at temperatures higher than 400-450 °C, while many MEMS fabrication processes require higher temperatures [5].

In the hybrid integration method, the electronics are fabricated on one wafer and the MEMS on another, and they are then assembled together or placed inside the same

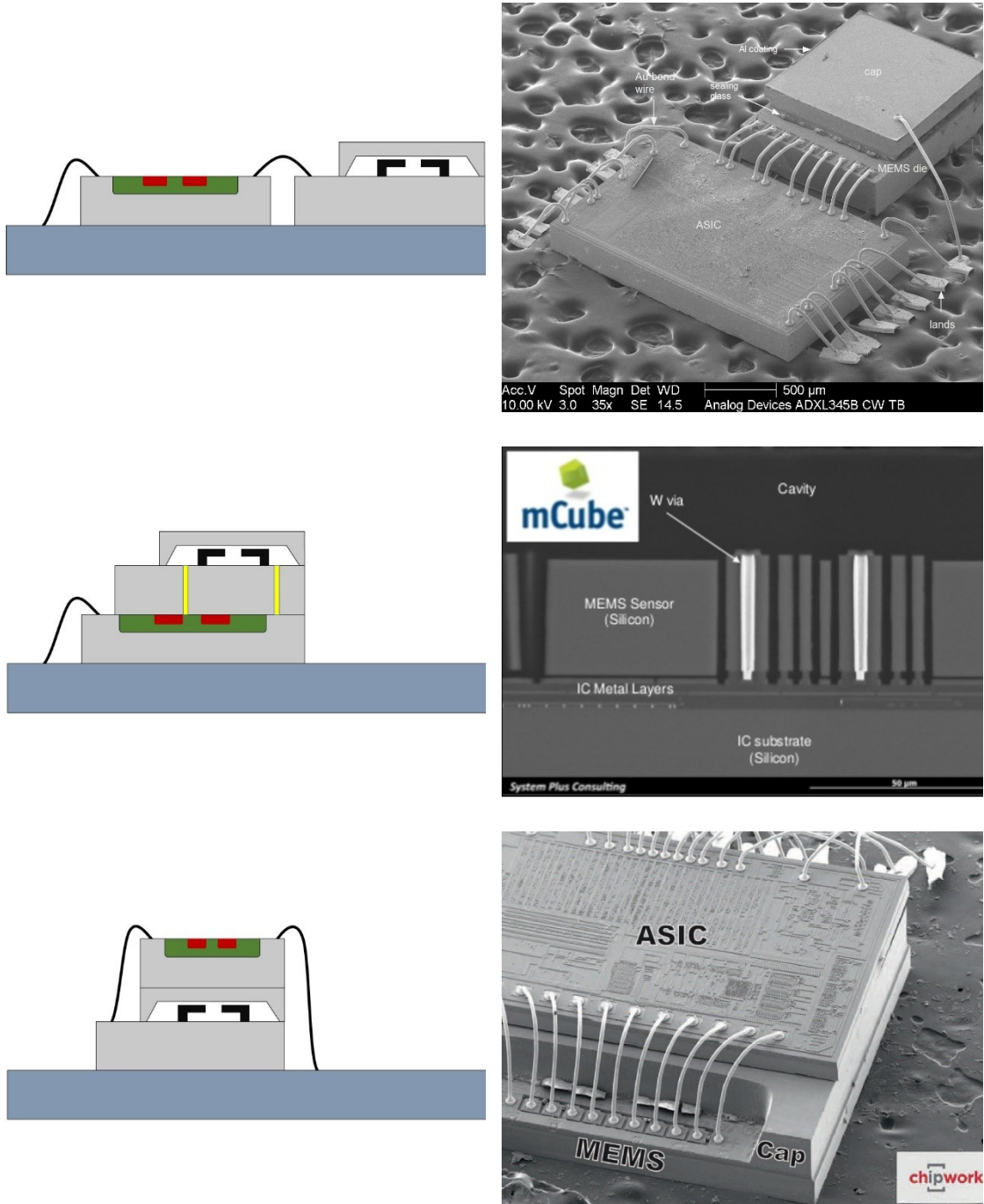


Figure 1.2: Different MEMS and IC hybrid integration methods [6, 7].

package separately. This assembly method is used in many of the MEMS-based products available on the market today. Figure 1.2 depicts different hybrid MEMS and IC integration methods. Placing the two dies next to each other is the simplest integration method, but it uses a larger footprint. Stacking the dies on top of each other eliminates that problem, but it is more complicated, as it needs precise die manipulation and alignment. In the hybrid integration method, the MEMS and IC are electrically connected to each other using bonding wires or Through-Silicon Vias (TSV) [8]. Hence, this method requires the use of a cap to encapsulate the MEMS components inside the package cavity to protect them during the dicing and integration steps and/or provide hermetic sealing [9-11].

The monolithic integration can be realized using various approaches, depending on the MEMS fabrication process (Figure 1.3). The main advantage of this integration method is that it uses the fabrication process to connect the MEMS to the IC, which reduces manufacturing complexity and enhances signal quality. The first approach uses a

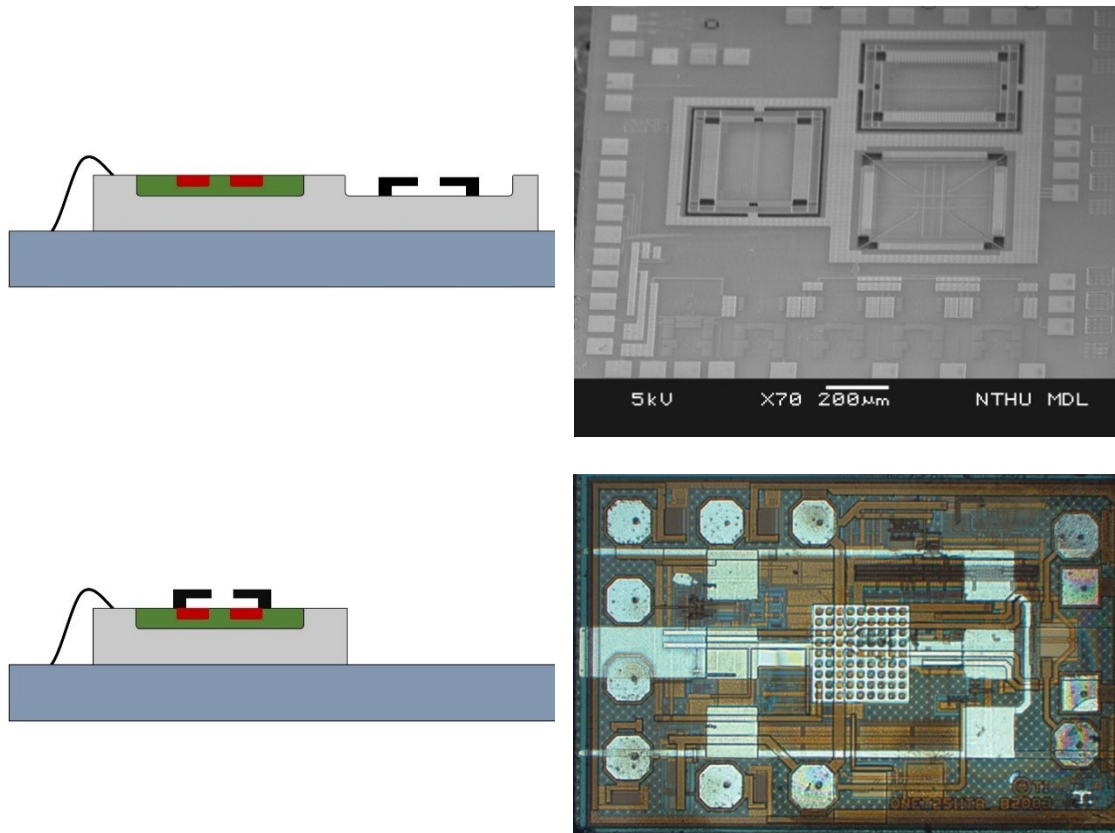


Figure 1.3: Monolithic MEMS and IC integration methods [12, 13].

complementary metal-oxide-semiconductor (CMOS) technology to fabricate the IC prior to the MEMS. Therefore, the approach is called MEMS-first or pre-CMOS integration, where the MEMS part is fabricated first on one side of the die and then the IC is later fabricated next to it [6, 14]. This method relieves the restrictions on the MEMS fabrication process but requires a larger die area, as the IC cannot be fabricated above the MEMS. The second approach uses interleaving integration to fabricate the MEMS and IC in the same process, with minimum or no post-processing release step for the MEMS part [12]. This method also needs a large area, because the two designs cannot be stacked. Moreover, it may result in inferior performance because of the limited mass created using the CMOS process. The post-CMOS or MEMS-last approach uses a CMOS-compatible process to build the MEMS above the IC, which minimizes the needed die footprint [15]. The ultimate challenge in using the latter integration approach is to develop a MEMS fabrication process with a low enough thermal budget, while yielding good device performances, and with no conflicts in any of the chemicals used with the underlying CMOS wafer. One advantage of this method is that it does not necessarily require encapsulation, as the MEMS is already assembled with its readout circuit on the same die.

In the inertial motion sensors market for consumer applications, combo sensors are becoming more dominant and they are expected to grow until they match their discrete counterpart by 2018 (Figure 1.4) [16]. This increases the importance of finding new methods to integrate more than one sensor on the same die and within the same package.

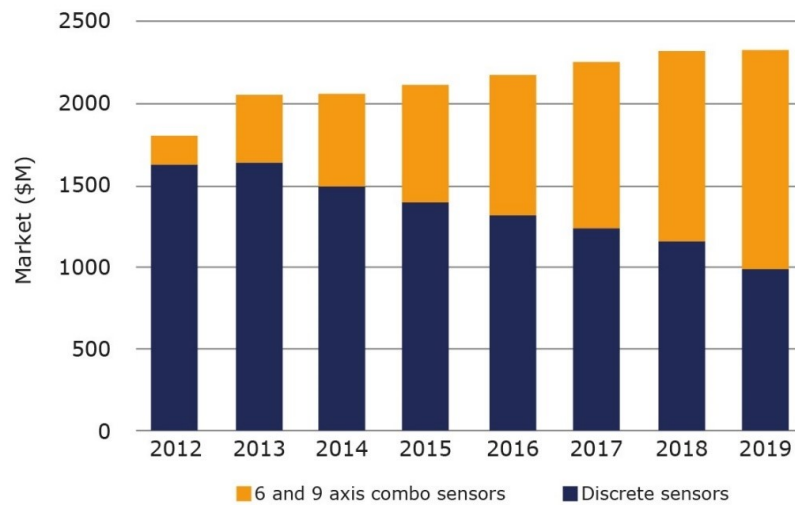


Figure 1.4: Consumer inertial motion sensors market [16].

It also marks the importance of decreasing the sensor size, as packages decreased from  $3 \times 5 \text{ mm}^2$  in 2009 to  $1.1 \times 1.1 \text{ mm}^2$  in 2015 [17, 18].

#### 1.4 Motivation

Ever since consumer electronics started using inertial motion sensors, there have been obvious improvements in their design and packaging. While sizes continue to shrink, new applications are being developed that have stricter requirements. In particular, new miniature appliances are being designed with even harder to meet requirements, especially for health or medical applications [19]. The necessity of integrating other MEMS devices onboard adds to the importance of minimizing the occupied space by finding new methods to reduce the number of used packages. One way to achieve this is already applied in inertial measurement units (IMU), which can include sensors of up to 9 axes [20].

The strategy of incorporating two sensors to balance power consumption and performance has been used in many battery-powered devices. For example, Apple Inc. unveiled its wireless headset AirPods in 2016. Aboard the electronics of each individual part, there are two MEMS accelerometer packages with different tasks (Figure 1.5). The first accelerometer is the Bosch BMA280, which is used for speech detection, while the second accelerometer is from STMicroelectronics and is used for motion detection [21]. The reason to include two devices with the same functionality is that they have different power consumption and performance. This issue raises three main challenges in the device

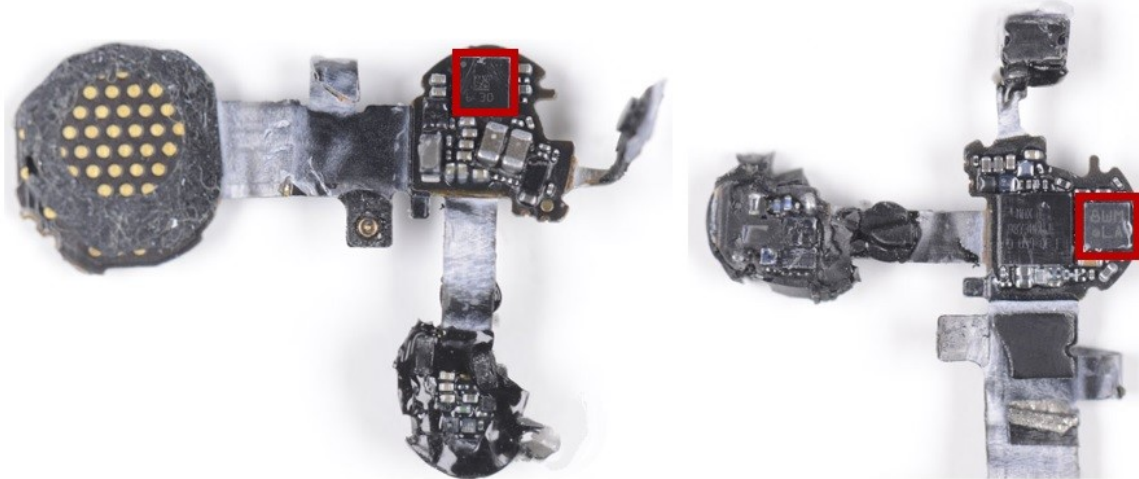


Figure 1.5: Apple AirPods components with two accelerometers highlighted in red [21].

design: the use of more space on small boards, increased power consumption, and more complex routing of boards' connection lines.

Most automated solutions today use controller systems. The packages of these systems are usually the largest components on the printed circuit board (PCB). With the increased dependence on MEMS in such systems, finding a simple technique that enables MEMS to be built above the controller IC will mark a new generation for these controllers. Such controllers will include the application specific integrated circuits (ASIC) for closed-package MEMS in their design, then build the required MEMS above them, e.g. inertial sensors, resonators, etc. This integration will cut the complexity of the final product design and assembly, as it will lower the number of soldering steps needed. It will also cut the number of PCB lines required to communicate with the MEMS, which is at least four lines for each sensor (i.e. power, ground, and two communication lines). As shown in the previous section, the monolithic SoC above-IC integration combines the advantages of small size and simple assembly, with no encapsulation requirements. This emphasizes the importance of focusing on that approach in developing future MEMS.

## 1.5 Research Goals

Above-IC fabrication, higher performance designs, and miniature 3D integration can be leveraged to achieve the size reduction seen as a major challenge for consumer applications [4]. This research aims to develop methods and fabrication processes that enable building MEMS devices of high quality above their ASICs. The first goal is to build capacitive accelerometers with high performance for consumer applications, using surface micromachining. The approaches used to achieve this goal follow two main paths: improving the current 2D design, and creating a 3D design that eliminates or reduces the 2D design limitations. Generally, surface micromachined processes produce devices with small proof masses, they exhibit limited performance in terms of sensitivity, and the case worsens for devices with sizes smaller than  $1 \text{ mm}^2$ . The approaches pursued here focus on increasing the sensitivity-to-area ratios of the sensors, then to verify the effectiveness of the solutions proposed. Devices with  $500 \times 500 \text{ }\mu\text{m}^2$  dimensions were fabricated and tested. These sizes were chosen to match/compete with the minute-size accelerometers available

on the market today. Mathematical models and finite element methods (FEM) are used to prove the hypotheses behind the new designs, before final fabrication.

The research also aims to develop CMOS-compatible surface micromachining processes to enable above-IC MEMS integration. The developed fabrication processes utilize materials that can be deposited at low temperatures, while not affecting the performance of the ASIC underneath it, i.e. less than 400 °C [22-24]. The scope of this research only covers the fabrication of the MEMS accelerometers, and not the entire system with the ASIC. Thus, the capacitance measurement electronic circuit needed had to be carefully designed with commercial components to meet the requirements of the fabricated devices. In addition, a test setup capable of simulating different acceleration values has to be built to test and characterize the fabricated accelerometers.

## **1.6 Contributions**

This research aimed to improve and propose new MEMS capacitive accelerometers. It delivers four main contributions, which are described below.

### **1.6.1 Accelerometer Designs Optimization in 2D Fabrication Processes**

MEMS capacitive accelerometers have conventionally been designed and fabricated as 2D components, with a tradeoff between the sensing electrodes' lengths and the proof mass widths. This part of the research proposes a method to optimize their designs to achieve the maximum possible performance within a certain area, as the method maximizes the sensitivity-to-area ratio. The optimum electrode lengths for different designs are found analytically using this method. For each design, various layouts (each within  $500 \times 500 \mu\text{m}^2$  area) are made with different electrode lengths [25]. The method is then proven by fabricating the different devices in a commercial Multi-User MEMS Process (MUMP), then evaluating their performance experimentally. The author did all the work here, with guidance from Dr. Alhomoudi regarding simulation.

### **1.6.2 Novel Dual-Axis Capacitive Accelerometers with Low Cross-Axis Sensitivity**

This work introduces a novel design for a dual-axis capacitive accelerometer to achieve low cross-sensitivity between the two input acceleration axes. It utilizes four

moving electrodes formed by four proof masses, each suspended using a supporting beam sharing one central anchor. The anchor also forms a pad for the moving electrodes. The capacitance is measured between the anchor and four fixed electrodes, with each being much more sensitive in one direction of the axis. Thus, the structure creates differential sensing in the two axes. The device measures  $1 \times 1 \text{ mm}^2$  and is fabricated in a commercial process to demonstrate the feasibility of the new design. It achieves a sensitivity of 16.86 fF/g and shows less than 1% cross-sensitivity, thereby proving the theory behind the improved design [26, 27]. The author did all the work here with guidance from Dr. Allidina regarding test set up and device characterization.

#### 1.6.3 In-Plane Capacitive Accelerometer in a 3D Surface Micromachining Process

This work introduces a novel design for a single-axis capacitive accelerometer. The design uses a platform process to create a 3D design with narrow sensing gaps to overcome the limitations currently present in 2D accelerometers. It enables the use of the entire device area for proof mass and sensing simultaneously, eliminating the necessity to make tradeoffs between the two. Moreover, the platform is also used to create novel L-shaped and Z-shaped supporting beams. Since this is a novel design in many aspects, a design model is developed to account for the narrow gaps noise and the supporting beam spring constant, in order to be able to predict the final performance of the accelerometer. For a 2D device with similar structural layer thickness, this design can outperform the conventional 2D design more than six times (based on the design parameters). A capacitive accelerometer is fabricated within a  $500 \times 500 \text{ }\mu\text{m}^2$  area and delivers 58 fF/g sensitivity. This design is the first reported to use a non-conductive material as the structural layer for capacitive in-plane acceleration sensing. This work has been submitted for a patent application [28], and is also in the publication review process [29]. The author did all the work described in this section.

#### 1.6.4 3D Surface Micromachining Process for Above-IC Integration

In this part of the research, a new CMOS-compatible surface micromachining process is developed to enable the realization of MEMS structures with narrow lateral gaps. This simple 3D fabrication process enables MEMS structures to be created using semi-

conductive or non-conductive materials, e.g., silicon nitride, to benefit from their mechanical properties. The process uses polyimide and aluminum layers to create one conductive set of the electrodes, and aluminum with silicon nitride to create the second set. A parylene layer is used to create the sacrificial layer between the two conductive parts, so that the structure can be released in a dry etching step. This work is also included in the filed patent [28] and the journal paper listed in the previous subsection [29]. The author did all the work described in this section.

## 1.7 References

- [1] S. Beeby, *MEMS mechanical sensors*. Artech House, 2004.
- [2] J. E. Brignell and N. M. White, *Intelligent Sensor Systems: 2nd*. institute of Physics Publishing, 1996.
- [3] Yole Développement, "Status of the MEMS Industry," Aug. 2016.
- [4] Yole Développement, "Status of the MEMS Industry 2014," August 2014.
- [5] M. J. Madou, *Fundamentals of microfabrication: the science of miniaturization*. CRC press, 2002.
- [6] A. C. Fischer *et al.*, "Integrating MEMS and ICs," *arXiv preprint arXiv:1604.04843*, 2016.
- [7] Yole Développement, "Sensors for Cellphones and Tablets 2016 report," Jun. 2016.
- [8] M. Motoyoshi, "Through-silicon via (TSV)," *Proceedings of the IEEE*, vol. 97, no. 1, pp. 43-48, 2009.
- [9] P.-V. C. Q. Zhang, F. Nabki, M. E. Gamal, "Thin-film wafer-level encapsulation for above-IC MEMS packaging," *Journal of Micromechanics and Microengineering*, vol. 23, no. 12, p. 125012, 2013.
- [10] M. Tilli, T. Motooka, V.-M. Airaksinen, S. Franssila, M. Paulasto-Krockel, and V. Lindroos, *Handbook of silicon based MEMS materials and technologies*. William Andrew, 2015.
- [11] M. Gad-el-Hak, *MEMS: applications*. CRC press, 2005.
- [12] M.-H. Tsai, Y.-C. Liu, K.-C. Liang, and W. Fang, "Monolithic CMOS—MEMS Pure Oxide Tri-Axis Accelerometers for Temperature Stabilization and Performance Enhancement," *Journal of Microelectromechanical Systems*, vol. 24, no. 6, pp. 1916-1927, 2015.
- [13] P.-V. Cicek *et al.*, "A novel prototyping method for die-level monolithic integration of MEMS above-IC," *Journal of Micromechanics and Microengineering*, vol. 23, no. 6, p. 065013, 2013.
- [14] G. K. Fedder, R. T. Howe, T.-J. K. Liu, and E. P. Quevy, "Technologies for cofabricating MEMS and electronics," *Proceedings of the IEEE*, vol. 96, no. 2, pp. 306-322, 2008.
- [15] F. Nabki, P.-V. Cicek, T. A. Dusatko, and M. N. El-Gamal, "Low-stress CMOS-compatible silicon carbide surface-micromachining technology—Part II: Beam resonators for MEMS above IC," *Journal of Microelectromechanical Systems*, vol. 20, no. 3, pp. 730-744, 2011.



- [16] Yole Développement, "6&9-Axis Sensors Consumer Inertial Combos," Nov. 2014.
- [17] Yole Développement & System Plus Consulting, "Inertial MEMS Manufacturing Trends 2014 - Volumes 1 & 2," March 2014.
- [18] mCube Inc., "mCube Redefines MEMS Sensor Innovation by Unveiling the World's Smallest 1x1mm Accelerometer," 2015.
- [19] A. Avci, S. Bosch, M. Marin-Perianu, R. Marin-Perianu, and P. Havinga, "Activity recognition using inertial sensing for healthcare, wellbeing and sports applications: A survey," in *Architecture of computing systems (ARCS), 2010 23rd international conference on*, 2010, pp. 1-10: VDE.
- [20] InvenSense Inc., "World's Lowest Power 9-Axis MEMS MotionTracking™ Device," 2017.
- [21] J. Morrison and D. Yang. "AirPods and the W1 wireless SoC: Squeezing innovative technology inside very small packages" [Online]. Available: <http://www.techinsights.com/about-techinsights/overview/blog/airpods-airpods-and-the-W1-wireless-SoC-squeezing-innovative-technology-inside-very-small-packages> [Accessed July 1, 2017]
- [22] F. Nabki, E.-G. Mourad, T. A. Dusatko, and S. Vengallatore, "Low temperature ceramic microelectromechanical structures," U.S. Patent 8,071,411, Dec 6, 2011.
- [23] F. Nabki, T. A. Dusatko, S. Vengallatore, and M. N. El-Gamal, "Low-stress CMOS-compatible silicon carbide surface-micromachining technology—Part I: Process development and characterization," *Journal of Microelectromechanical Systems*, vol. 20, no. 3, pp. 720-729, 2011.
- [24] M. Martyniuk, J. Antoszewski, C. Musca, J. Dell, and L. Faraone, "Stress in low-temperature plasma enhanced chemical vapour deposited silicon nitride thin films," *Smart Materials and Structures*, vol. 15, no. 1, p. S29, 2005.
- [25] A. Alfaifi, I. A. Alhomoudi, and M. N. El-Gamal, "Optimization of in-plane SiC capacitive accelerometers design parameters," in *New Circuits and Systems Conference (NEWCAS), 2016 14th IEEE International*, 2016, pp. 1-4: IEEE.
- [26] A. Alfaifi, F. Nabki, and M. N. El-Gamal, "A dual-axis bulk micromachined accelerometer with low cross-sensitivity," in *Electronics, Circuits and Systems (ICECS), 2012 19th IEEE International Conference on*, 2012, pp. 733-736: IEEE.
- [27] A. Alfaifi, K. Allidina, F. Nabki, and M. N. El-Gamal, "A low cross-sensitivity dual-axis silicon-on-insulator accelerometer integrated as a system in package with digital output," *Analog Integrated Circuits and Signal Processing*, vol. 77, no. 3, pp. 345-354, 2013.
- [28] A. Alfaifi, I. A. Alhomoudi, and M. N. El-Gamal, "High Sensitivity Capacitive Accelerometer in a CMOS-Compatible Fabrication Process," *US Provisional Patent Application*, filed December 2017.
- [29] A. Alfaifi, I. A. Alhomoudi, F. Nabki, and M. N. El-Gamal, "In-Plane High Sensitivity Capacitive Accelerometer in a 3D CMOS-Compatible Surface Micromachining Process," *Journal of Microelectromechanical Systems*, pp. 1-10, submitted December 2017.

---

# Chapter 2

## Overview of Accelerometers

---

### 2.1 Introduction

Accelerometers are devices that are used to sense static or dynamic motions or gravitational accelerations. The most accurate description of accelerometers' function is that they determine the acceleration or deceleration experienced by a certain mass, by sensing or measuring the input acceleration forces and comparing them to a known calibrated force. These measurements are determined in proportion to Newton's laws of motion. By combining an accelerometer with a gyroscope and a magnetometer, the system orientation can be precisely detected.

Many applications in our lives use accelerometers, and the list is continuously expanding. Few decades ago, they were mainly used in structure monitoring and aircraft systems. Today, they are used in many systems, from space satellites to electronic toys. Their vital importance is in applications where other systems cannot provide similar information, e.g., the drilling bit tilt angle in oil wells. They can also be used to measure seismic earth vibrations, which are small dynamic accelerations. In recent years, accelerometers have also found their way into heart implant systems.

This chapter presents a general overview of accelerometers. First, it reviews the history of the accelerometers' early usages and their development from their original sizes to MEMS. The next section then discusses accelerometers' general operation principles and explains their key performance characteristics. Subsequently, the main acceleration sensing mechanisms are briefly reviewed in the following sections, and their strengths and weaknesses are evaluated. The two following sections then discuss MEMS capacitive accelerometers and their applications. Finally, the work revises figures of the MEMS accelerometer markets, and reviews some state-of-the-art MEMS accelerometers available on the market today.

## 2.2 Historical Background

Fueled by two world wars and rapid scientific advances, the 20<sup>th</sup> century saw the creation of many tools that were not previously realizable, including acceleration meters or accelerometers. Burton McCollum and O. S. Peters developed a strain gauge in 1924, calling it “a new electrical telemeter” ( Figure 2.1 (a)) [1]. It was capable of making types of measurements, such as strain, pressure, small displacement, and acceleration. It took three more years before it was commercialized in 1927 to be used in aircraft, bridges, and dynamometers. It is considered to be the first accelerometer, and this sensing method was so successful that it led in the following two decades to acceleration and vibration sensing. Per Bruel and Viggo Kjaer started their B&K company in 1942 in Denmark, and in the following year they launched “Type 4301”, the first commercial piezoelectric accelerometer in the world (Figure 2.1 (b)) [2].

In 1959, Richard Feynman presented his famous lecture “There is Plenty of Room at the Bottom” during the American Physical Society annual meeting [3]. In his talk, Feynman encouraged further usage of material at the smallest possible scale. In the conclusion of his talk, Feynman gave the audience two challenges with \$1,000 prize each, one of which was to construct a functional electric motor smaller than  $\frac{1}{4}$  cubic inch. That challenge was met the following year by William McLellan who built the desired solution

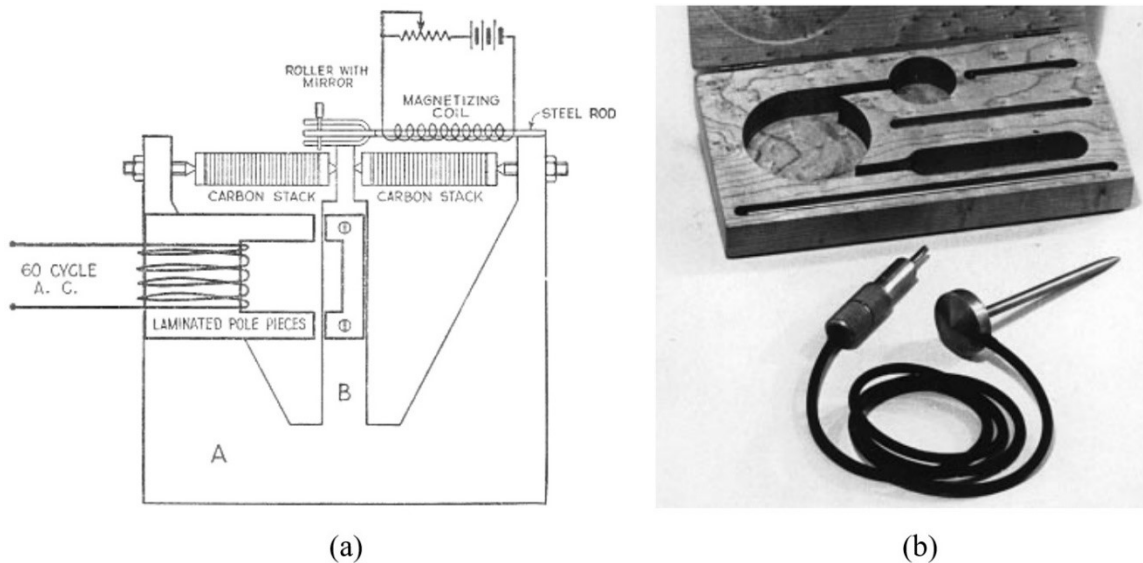


Figure 2.1: (a) Diagram of the first strain gauge accelerometer, and (b) photo of the first piezoelectric accelerometer [1, 2].

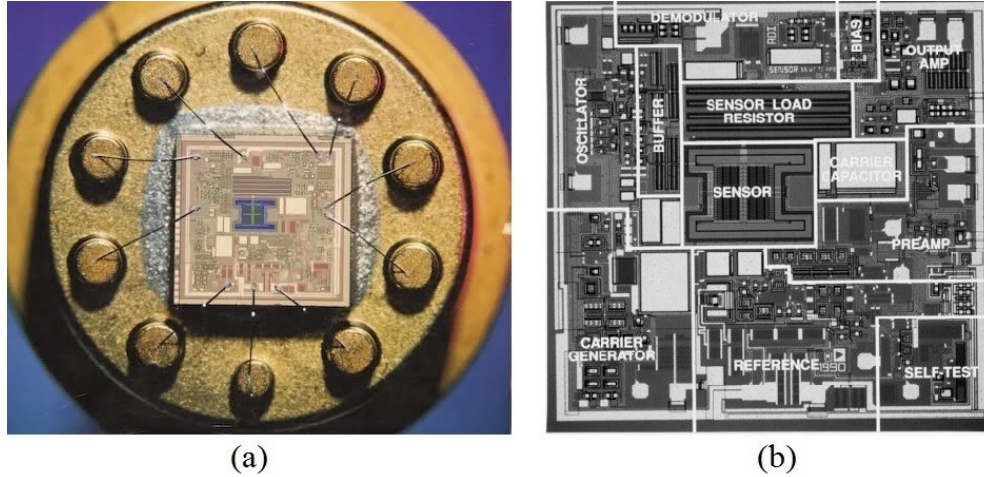


Figure 2.2: ADXL50 accelerometer (a) package and (b) die components [6].

using conventional tools. Four years later, H. C. Nathanson and his team built what can be described as the first MEMS device, a resonant gate transistor [4]. Ever since, researchers have been developing new solutions and sensors using a top-down approach to create a solid ground for the MEMS sensors. In 1979, the first MEMS accelerometer was built at Stanford University [5].

The year 1991 marks a key milestone for accelerometers. Analog Devices introduced the ADXL50 as the first commercial surface micromachined monolithic MEMS accelerometer (Figure 2.2) [6, 7]. It was a capacitive sensor designed for vehicle crash detection, and it could measure accelerations up to  $\pm 50$  g. It included a self-test feature that relieved the doubts about using this new technology in the automotive industry. It turned out to be highly reliable and each unit was sold for \$5, which was a quarter of the price of previously used macro sensors. Its success opened the door for more MEMS sensors in the automotive industry (especially accelerometers), which later found their way to consumer products.

### 2.3 Types of Accelerometers

The general mechanical model of accelerometers is composed of three basic elements: a proof mass, a spring, and a damper (Figure 2.3). The motion of the proof mass due to an applied acceleration is described by Newton's second law of motion and can be detected or measured using various means. When the system with a total mass  $M$  undergoes

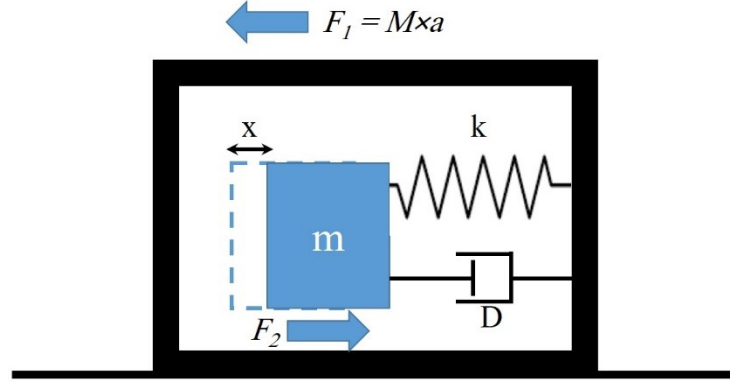


Figure 2.3: Accelerometer system model.

an  $F_1$  acceleration force, the accelerometer's proof mass  $m$  experiences an equal  $F_2$  force in the opposite direction. The equation of motion of the proof mass can be expressed as:

$$F_1 = F_2, \text{ and} \quad (2.1)$$

$$M\ddot{x}_M = m\ddot{x} + D\dot{x} + kx, \quad (2.2)$$

where  $\ddot{x}_M$  is the system's acceleration;  $D$  is the proof mass damping; and  $\ddot{x}$ ,  $\dot{x}$ , and  $x$  are the proof mass acceleration, velocity, and displacement, respectively. When an input acceleration is experienced (or when it ends), the proof mass needs to reach a steady state quickly. Thus, the proof mass should be in an environment with a damping factor that hastens the stabilization process. It usually needs to work in an environment with a controlled damping factor, e.g., air sealed packages.

In an inertial system of a specific reference, and according to Newton's second law of motion, the sum of forces experienced by a certain object equals its mass multiplied by the experienced acceleration. There are three way to measure that force [8]:

1. Compare the unknown force to a force resulting from a known mass under a known acceleration, e.g. a weighing scale;
2. Compare the unknown force to a calibrated force, e.g. the force balance accelerometers; and
3. Compare the unknown force to a known force resulting in a beam deflection per Hooke's law, e.g. MEMS accelerometers with proof mass deflection.

### 2.3.1 Force Balance Accelerometers

The force balance accelerometer is a closed-loop system that is also known as servo accelerometer. In such accelerometers, a proof mass is suspended between two electromagnetic coils with opposite signals. When there is no acceleration, the mass is held at equilibrium position with no signals applied to it. When it moves as it senses acceleration, one of the coils applies electromagnetic force to restore it to equilibrium position. The amount of this feedback signal is then used to output the experienced force and hence a measure of the acceleration [8, 9]. These systems are usually bulky and require high power compared to MEMS accelerometers. They are preferred in systems that require high reliability and ruggedness, such as nuclear reactors and dams.

### 2.3.2 Deflection Accelerometers

In a deflection accelerometer, the mass is suspended using a beam that bends due to the acceleration force exerted on the mass. The bend causes some physical characteristics of the beam to change, indicating the applied force value. The changes are reversible and the original values are regained as the mass moves to its neutral position. Some of these characteristics are displacement, stress, and strain. The main drawback to this type of accelerometers is their poor repeatability, which makes them deficient for sensitive applications. In general, MEMS accelerometers are of this type.

Based on their feedback structure and readout systems, deflection accelerometers can be classified into open-loop and closed-loop systems [10]. The open-loop accelerometers measure the mass displacement using different sensing methods. The new position of the mass is then converted into a signal that can be amplified for more accurate results (Figure 2.4 (a)). These accelerometers have limited ranges and linearities, but a simpler mechanical structure, and their readout circuitry are easier to design. On the other hand, closed-loop accelerometers keep the mass at equilibrium position using different actuation methods (similar to the force balance accelerometers). They outperform the open-loop accelerometers but they require more sophisticated control and readout circuitry (Figure 2.4 (b)).

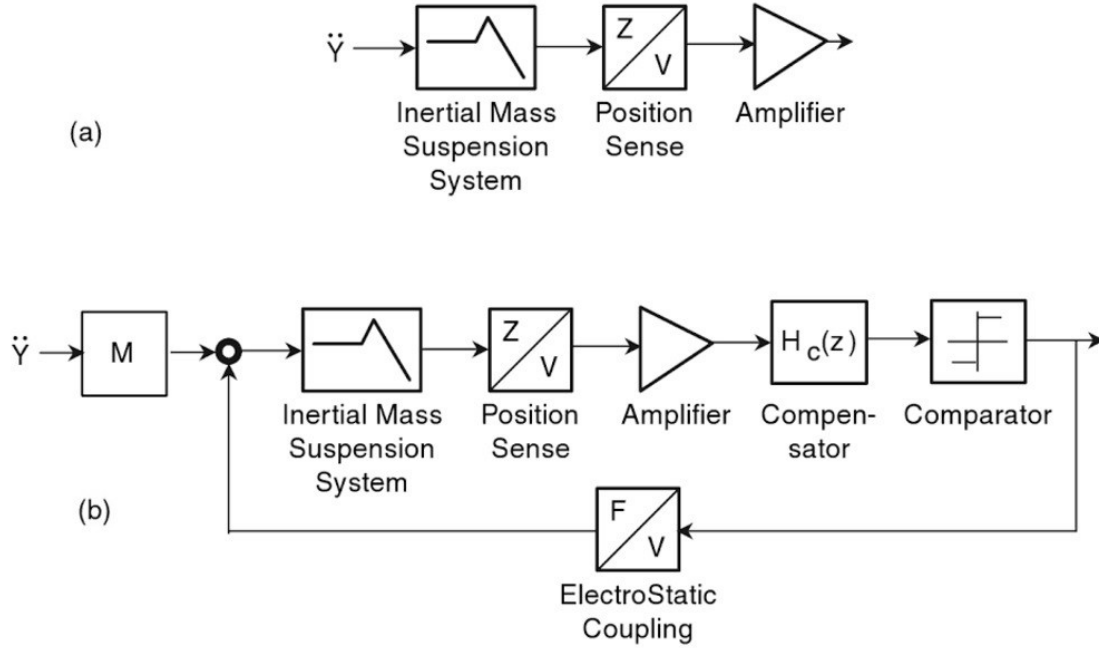


Figure 2.4: Block diagram of (a) open-loop, and (b) closed-loop accelerometer systems [10].

## 2.4 Accelerometers' Performance Characterization

Transducers are devices that convert one form of energy to another form that can be easily measured or detected [8, 11]. Sensors and actuators are the most common types of transducers, because they convert from or to electrical energy that can be controlled or measured with high accuracy. Sensors convert one form of energy to electrical energy (or signals), while actuators convert electrical energy to another form of energy. Among the most famous sensors are acceleration sensors or accelerometers, which convert mechanical energy resulting from the acceleration force to electrical signals.

Accelerometers are widely used in many applications, and since each application has its specific requirements, their characteristics or performance differ according to the needs of each application. For a specific application, one needs to pick an accelerometer that can sustain the living conditions in that application, e.g., a cellphone accelerometer will not be suitable for car accident detection. Several terms are used to describe accelerometers' performance, and some of these terms are correlated with each other. Hence, it is critical to understand the influence of each of these terms before beginning the

design process, as they have a direct impact on the accelerometer performance. Some of these important terms are defined below [12, 13].

Sensitivity: the rate of output change per unit change in input acceleration; also called the scale factor. It is usually given in [V/g] in accelerometers with analog voltage output, and in [LSB/g] (Least Significant Bit) in their digital counterparts.

Range: also known as full-scale; it is the maximum acceleration input for the accelerometer specified performance, and is usually evaluated in [g].

Accuracy: the closeness of the measured parameter to the actual input and its unit is [g], e.g., an accelerometer reading 1.001 g for an input of 1 g has 1 mg accuracy. This difference results from the accelerometer combined errors, e.g. nonlinearity and noise.

Resolution: minimum detectable acceleration difference; expressed in [g]. For acceleration differences that are smaller, the resolution will not be recognized and the output will be rounded to the previous or next resolved acceleration.

Bandwidth: the frequency range of measurable accelerations; can be measured [Hz].

Bias: the sensor output when there is no input acceleration; has the same unit as the sensitivity, i.e. [V/g] or [LBS/g].

Cross-axis sensitivity: the sensitivity of an accelerometer to an acceleration that is applied to an axis perpendicular to its sensing axis; for example, the change in the X-axis acceleration reading in response to an acceleration in the Y-axis. Sometimes, it is called the “transverse” sensitivity. It is expressed as a percentage [%] of the sensing axis sensitivity.

Noise: the minimum acceleration that can be detected; it is measured in [g/ $\sqrt{\text{Hz}}$ ]. It is mainly set by the noise density of the mechanical structure in combination with the noise in the electronic reading circuitry. Sometimes, it is referred to as the minimum detectable signal or noise floor. It can be improved by explicitly lowering the bandwidth.

Linearity: the maximum deviation of the output sensitivity from a line of best fit between zero and full-scale. The linearity is expressed as a percentage with respect to the full-scale output [%FS].



## 2.5 Sensing Mechanisms in MEMS Accelerometers

Researchers have built MEMS accelerometers using different sensing mechanisms. Some of these mechanisms are piezoelectric, piezoresistive, capacitive, resonant, tunneling, and optical [14, 15]. The first three sensing mechanisms have made their way into most MEMS accelerometers on the market, thanks to their remarkable performance. Below is a brief review of each of these sensing mechanisms [16-20].

### 2.5.1 Piezoelectric Accelerometers

In piezoelectric acceleration sensing, a proof mass that undergoes input acceleration applies force on a micromachined film (mostly quartz). Due to its unique properties, the film generates an electrical signal when it experiences a stress difference from the applied force load (Figure 2.5). For a piezoelectric film with thickness  $t$  and area  $A$ , the output voltage,  $V$ , is given by:

$$V = g_{33} \frac{t}{A} ma, \quad (2.3)$$

where  $g_{33}$  is the piezoelectric coefficient,  $m$  is the proof mass, and  $a$  is the input acceleration.

Piezoelectric accelerometers can operate in harsh conditions and have the highest bandwidth range of all sensing types. They can be used to measure acceleration in temperatures up to 350 °C, before experiencing losses beyond that temperature; still, they can sense acceleration up to 1000 °C with degraded performance. Inherited from their sensing mechanism, the range of these accelerometers can reach up to 6000 g, which makes them suitable for high-shock applications. As a disadvantage, the piezoelectric

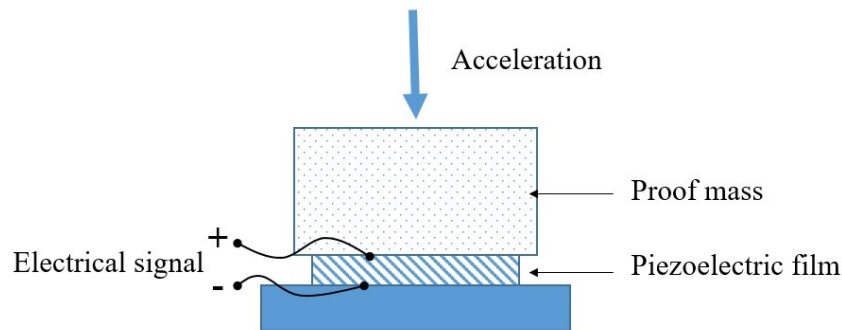


Figure 2.5: Simplified diagram of piezoelectric accelerometer

accelerometer cannot be used for static sensing applications, e.g., tilt detection. It needs high-performance electrical connections and its sensitivity can be altered by environmental variables, i.e. humidity and temperature.

### 2.5.2 Piezoresistive Accelerometers

Piezoresistive accelerometers are built with one or more supporting beams that hold a proof mass. Piezoresistors are placed on top of the supporting beam using selective doping. When the proof mass endures acceleration, it causes the supporting beam to bend and hence changes the resistance (Figure 2.6). The difference in the resistance can be measured by simply placing this piezoresistor in a Wheatstone bridge readout circuit. The ratio of the resistance change to the original resistance is given by:

$$\frac{dR}{R} = \frac{d\rho}{\rho} + (1 + 2\nu)\varepsilon, \quad (2.4)$$

where  $R$  is the resistance,  $\rho$  is the resistivity,  $\nu$  is Poisson's ratio, and  $\varepsilon$  is the strain.

Piezoresistive accelerometers are also useful for sensing accelerations under difficult conditions, and they have a wide bandwidth down to DC sensing (0 Hz). Their

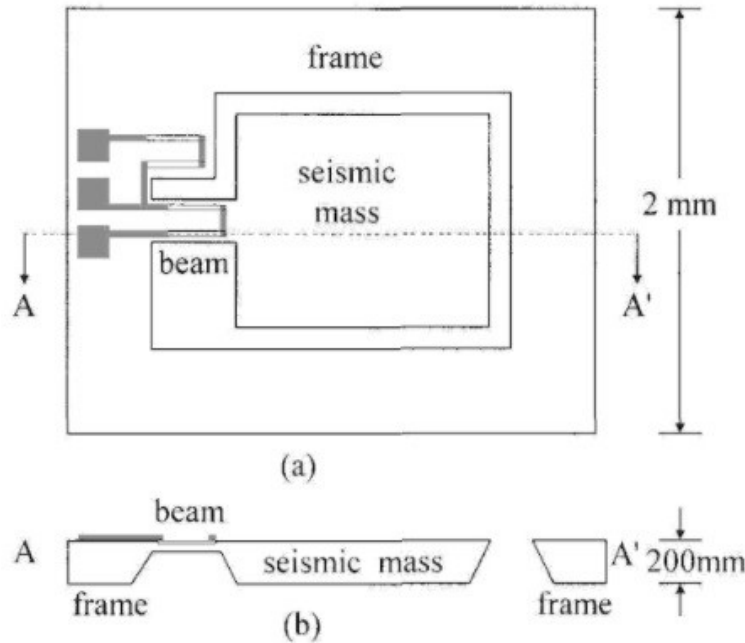


Figure 2.6: Schematic of the first silicon piezoresistive accelerometer; (a) top view, and (b) cross-section view [21].

readout circuits are simple and can be easily fabricated. Because resistance is affected by temperature, piezoresistive accelerometers show poor stability with temperature variations. The length-to-area changing ratio causes these accelerometers to exhibit curved linearity, and high-power consumption and moderate sensitivity are other known drawbacks of these accelerometers.

### 2.5.3 Capacitive Accelerometers

Capacitive accelerometers consist of three main parts: i) a moving proof mass supported by ii) an anchored beam and iii) a fixed electrode. When the input acceleration causes the proof mass (that also acts as a moving electrode) to bend the supporting beams, the capacitive gap separating it from the fixed electrode changes. The input acceleration can be determined by measuring the resulting capacitance change. This is explained in more detail in the next section.

While capacitive accelerometers are not the best solution for high temperatures, they have very good stability in temperature varying conditions. They can be fabricated in miniature sizes and have low power consumption and DC sensing. However, capacitive accelerometers are sensitive to electromagnetic fields and their bandwidth is not as wide as that of piezoelectric or piezoresistive accelerometers. They also have limited input ranges and require more complex readout circuits. Capacitive accelerometers are susceptible to electromagnetic fields and hence require proper shielding packages.

### 2.5.4 Performance Assessment

As seen above, piezoelectric and piezoresistive accelerometers are superior for high-end applications, while capacitive accelerometers dominate where low-cost, low-power, and fair performance is needed. However, many applications require miniature-sized accelerometers. When size is minimized to build MEMS accelerometers, piezoelectric and piezoresistive accelerometers fall behind capacitive accelerometers in many aspects (Figure 2.7). One of the most important aspects is the DC response, which is essential for many applications. Thus, large piezoelectric accelerometers led high-end applications where DC response is not needed, while MEMS capacitive accelerometers

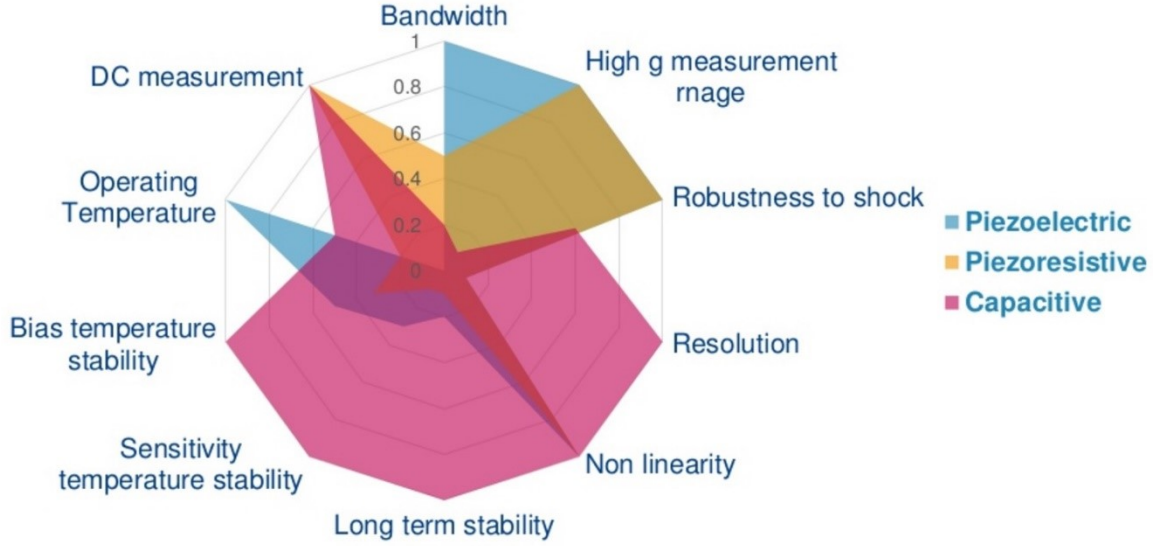


Figure 2.7: Performance comparison between the piezoelectric, piezoresistive, and capacitive MEMS accelerometers [24].

dominated consumer applications, leaving a small share to the piezoresistive accelerometers in either markets [22, 23].

## 2.6 MEMS Capacitive Accelerometers

Using a surface micromachining process, MEMS capacitive sensors can be built with a moving electrode and one or more fixed electrodes. The design depends on creating at least one capacitance that has a value given by:

$$C = \epsilon \frac{A}{d}, \quad (2.5)$$

where  $\epsilon$  is the permittivity,  $A$  is the capacitive area, and  $d$  is the capacitive gap. The amount of capacitance change is caused by the variation in either the gap or the area. Since the capacitance change is usually small, a differential capacitance scheme is favored over a single-ended scheme, because the former leads to better linearity. The differential scheme also cancels out the parasitic capacitance in the wire bonds and the connection wires, leading to more accurate output.

Figure 2.8 shows a simple schematic of differential varying overlap and varying gap-sensing schemes. In a differential varying gap accelerometer with no input,  $C_1$  and  $C_2$

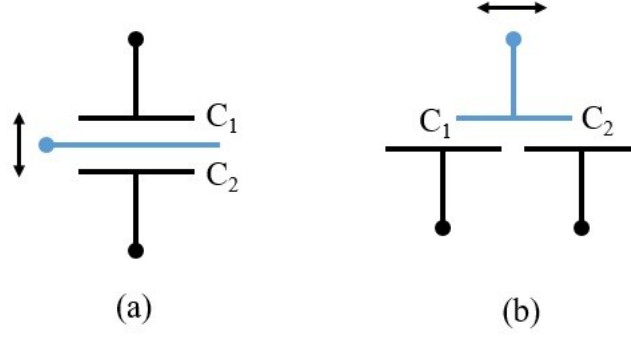


Figure 2.8: Schemes of differential (a) varying gap and (b) varying overlap, with the moving electrode shown in blue.

will have equal capacitance values. When the moving electrode moves an  $x$  distance towards  $C_1$ , the capacitance change becomes:

$$\Delta C = C_1 - C_2 = \frac{\epsilon A}{(d - x)} - \frac{\epsilon A}{(d + x)} = \frac{2\epsilon Ax}{d^2 - x^2}. \quad (2.6)$$

Consequently, the capacitance change per displacement, or the sensitivity, can be expressed as:

$$S = \frac{dC}{dx} = \frac{2\epsilon Ax(d^2 - x^2)}{(d^2 - x^2)^2} \approx \frac{2\epsilon A}{d^2} \text{ when } d \gg x. \quad (2.7)$$

The sensitivity is nonlinear in the aforementioned expression, leading to different sensitivities for different input accelerations. Yet, if the displacement resulting from the maximum input is less than one third of the initial gap, the sensitivity would have acceptable linearity [25].

In the differential varying overlap scheme, the moving electrode moves parallel to the two fixed electrodes. This motion increases the capacitance area with one of them while reducing it with the other. For an  $a \times b$  rectangular electrode that moves a distance  $x$  parallel to  $b$ , the capacitance change is:

$$\Delta C = C_1 - C_2 = \frac{\epsilon a(b + x)}{d} - \frac{\epsilon a(b - x)}{d} = \frac{2\epsilon ax}{d}. \quad (2.8)$$

Thus, the sensitivity for a differential varying overlap accelerometer is given by:

$$S = \frac{dC}{dx} = \frac{2\epsilon a}{d}, \quad (2.9)$$

where we observe is a linear relationship between the sensitivity and the displacement or the input acceleration.

Both schemes are used to sense in-plane and out-of-plane accelerations. The sensing scheme is chosen based on the needed performance, sensing axis, and fabrication process. In general, the varying overlap is used for high open-loop ranges where the closing gap does not obstruct the sensing range, while the varying gap is prioritized when high sensitivity is required for shorter ranges, or with closed-loop control. Figure 2.9 (a) depicts a varying gap differential capacitive accelerometer [26]. As the proof mass moves due to input acceleration, this decreases the distance to one set of fixed electrodes while increasing the distance to the other. A torsional capacitive accelerometer that rotates when experiencing an input acceleration is shown in Figure 2.9 (b) [27]. The proof mass rotates around the supporting beam due to the resulting torque, resulting in a change in the capacitance overlap area, and hence the detection of the input acceleration value.

## 2.7 MEMS Accelerometer Applications

MEMS accelerometers are used in a wide variety of applications. They can be found in many of the electronics that people use on a daily basis, and the list continues to

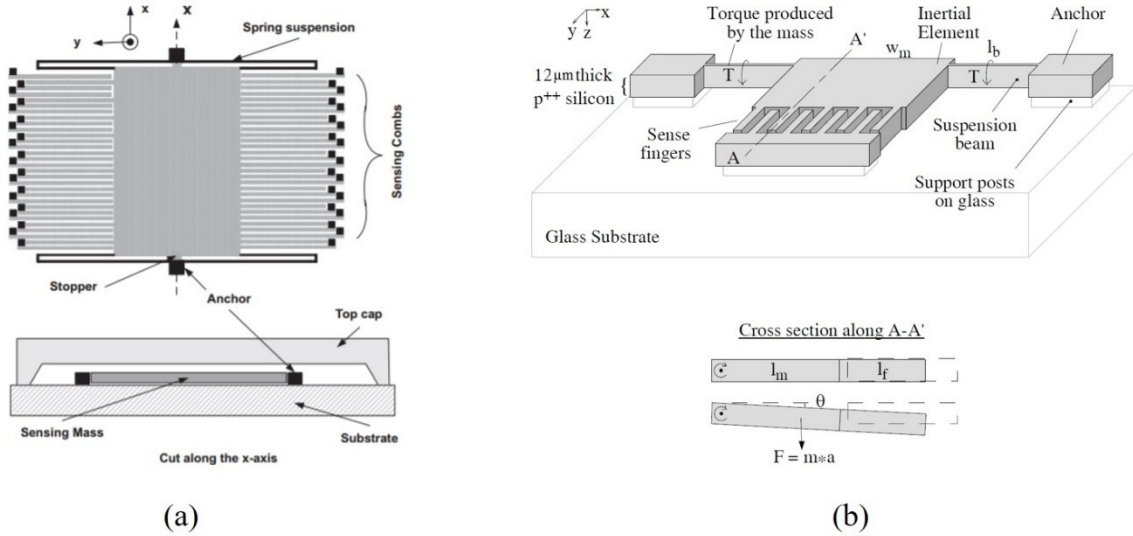


Figure 2.9: Examples of fabricated (a) varying gap and (b) varying overlap capacitive accelerometers [26, 27].

grow. Consumer electronics and automotive applications incorporate the clear majority of MEMS accelerometers with 54.5% and 34.1% shares, respectively (Figure 2.10). However, accelerometers are also used in other areas, including industrial, medical, and aerospace and defense applications, together representing about 11.4% of the inertial motion sensors market [28]. The following discusses the MEMS accelerometers used in consumer electronics and automotive applications in more detail [29-31].

1. Consumer electronics is by far the largest market for MEMS accelerometers nowadays, with billions used in different electronics to determine the inclination or acceleration of a system. They are used in cellphones to set screen orientation or to measure hand motion acceleration for some applications. Gaming consoles use accelerometers to find the hand orientation, and fitness trackers count footsteps by reading the shock signals. Hobby drones use accelerometers to determine the frame tilt and correct it according to the flying commands. Other applications include but are not limited to computer hard disks, printers, and optical stabilization of digital cameras. These applications have relatively the same accelerometer requirements, which can easily be achieved in surface micromachining processes.
2. Automotive is the second largest market for accelerometers, allegedly using many millions of them. Multiple accelerometers are strategically placed in the electronics system of modern vehicles. However, broader ranges of accelerometer specs are

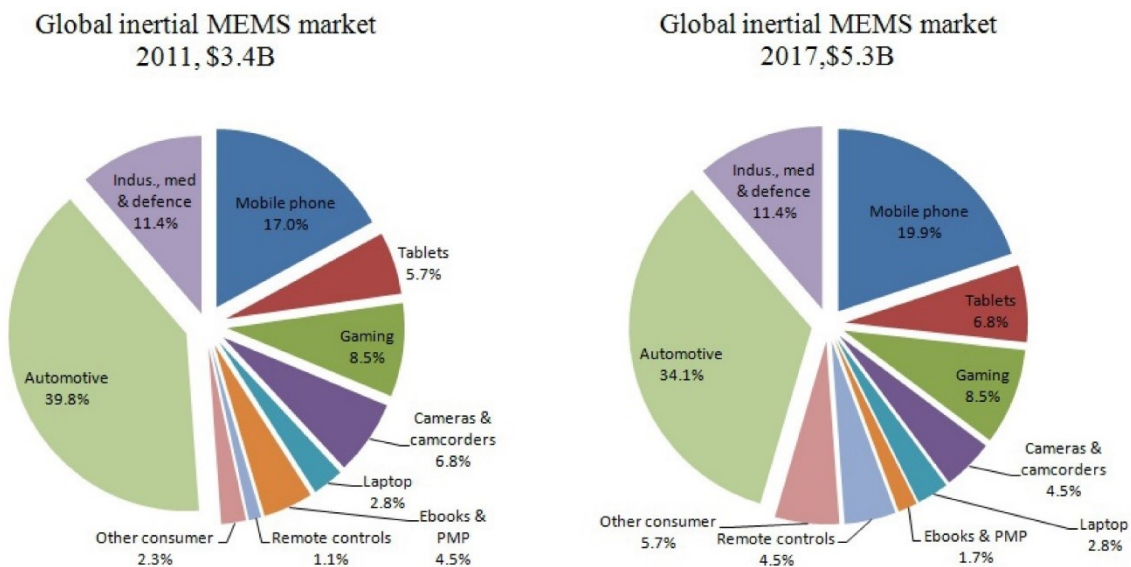


Figure 2.10: Applications market share in 2011 and 2017 [28].

required here, as their functions are different. For example, airbag deployment systems need multiple accelerometers around the frame of the vehicle with high-g shock since the impacts usually cause deceleration in tens of g's. On the other hand, vehicle dynamic control (VDC) systems use multiple accelerometers with low-g's and gyroscopes to regain control when the vehicle starts skidding.

Some applications remain interesting targets for new MEMS accelerometer developments, such as aerospace, oil and gas, and different types of electronic processors with integrated sensors. Aerospace is the market least targeted by MEMS accelerometers, because of its highly demanding specifications, especially in terms of reliability [32]. MEMS in space are susceptible to high doses of radiation that make them fail after a short life span, which is not desirable for systems intended for many years of usage.

## 2.8 MEMS Accelerometer Market Review

The MEMS market is one of the most competitive markets in the electronics industry. Few years can shuffle the order of the top manufacturing companies and introduce new players into the market [34]. For example, Texas Instruments was the largest MEMS manufacturer in 2010, but its sales volume decreased and it became the third in 2015, while Bosch tripled its MEMS sales in those five years to become the top MEMS manufacturer with sales of more than \$1.2 billion [33, 35]. Currently, inertial motion sensors make up

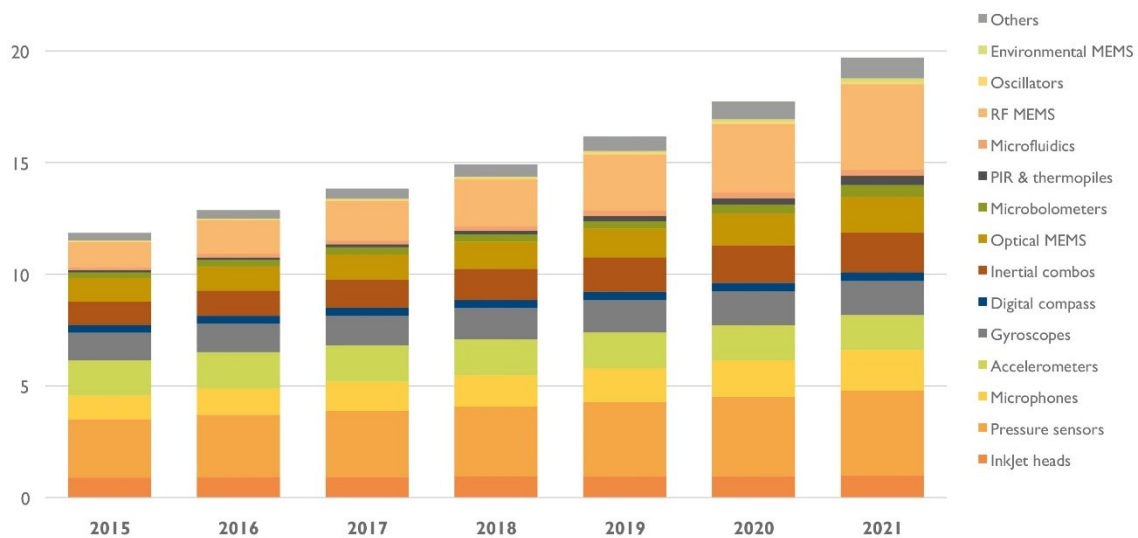


Figure 2.11: 2012 to 2021 MEMS market forecast in US\$ billions [33].



the lion's share of the MEMS markets, with a percentage exceeding 30% of the total MEMS sensors, estimated at a \$12.5 billion.

Even though the discrete accelerometer markets are not expected to exhibit noticeable growth in the short term, the combined market for combo and discrete motion sensors is expected to reach \$2.3 billion for consumer applications alone (Figure 2.11) [23, 33]. Moreover, inertial motion sensors are used in several applications in the new emerging markets of the internet of things (IoT) and wearables. The IoT hardware sector is expected to grow from \$35 billion in 2016 to \$70 billion in 2018, while the wearables market is expected to reach \$100 billion in 2020 [36, 37]. Hence, these new markets are expected to boost MEMS inertial sensor sales dramatically and lead to another MEMS manufacturing wave similar to that created by smart phones and tablets.

Every year, companies release competitive MEMS accelerometers onto the market, targeting different specifications. Below is a brief review of two state-of-the-art MEMS accelerometers that target high-end and consumer applications.

#### 2.8.1 Safran Colibrys SA Single-Axis Tactical-Grade Accelerometer

Honeywell, Northrop Grumman Litef, and Sagem lead the market of accelerometers for high-end applications, producing different non-MEMS accelerometers. Recently, Safran Colibrys SA started targeting that same market by developing new MEMS accelerometer solutions. One of its solutions is the tactical-grade MS1000 family of MEMS accelerometers that can be used for aerospace and defense applications [38]. It is fabricated using bulk micromachining to build a “sandwiched” proof mass that uses varying gap capacitive sensing to output an analog signal. It has extremely low noise of  $2 \mu\text{g}/\sqrt{\text{Hz}}$  and can detect resolutions down to  $7 \mu\text{g}$  with  $240 \mu\text{g}$  long-term repeatability in a package that is  $9 \times 9 \text{ mm}^2$ . These are very aggressive specifications.

#### 2.8.2 mCube 3-Axis Accelerometer for Consumer Applications

With the rising trend of building combo inertial measurement units instead of discrete accelerometers, mCube chose to manufacture a 3-axis accelerometer with high sensitivity for consumer applications. MC3213 is intended to be part of consumer applications, e.g., cellphones, gaming controllers, etc. [39]. It is a low-noise accelerometer

with digital output that enables it to be easily integrated with other digital components. It has 4 mg sensitivity for a range up to  $\pm 8$  g and an impressively small footprint of  $3 \times 3$  mm<sup>2</sup>.

## 2.9 Conclusion

This chapter has provided a general overview of the history of accelerometers, working principles, types, applications, and market status and potential. As shown, acceleration sensing is moving towards building miniature and low-power sensors, making MEMS technologies the optimum approach for future accelerometers. The automotive and consumer products represent the largest MEMS accelerometer markets, and they mainly depend on the capacitive sensing scheme due to its substantial advantages over other sensing mechanisms. The research in this thesis focuses on how to solve the challenges of existing designs and fabrication technologies of MEMS capacitive accelerometers, and how they can be improved.

## 2.10 References

- [1] B. McCollum and O. S. Peters, *A new electrical telemeter*. US Government Printing Office, 1924.
- [2] P. L. Walter, "Review: Fifty years plus of accelerometer history for shock and vibration (1940–1996)," *Shock and Vibration*, vol. 6, no. 4, pp. 197-207, 1999.
- [3] R. P. Feynman, "There's plenty of room at the bottom," *Engineering and science*, vol. 23, no. 5, pp. 22-36, 1960.
- [4] J. A. Pelesko and D. H. Bernstein, *Modeling Mems and Nems*. CRC press, 2002.
- [5] L. M. Roylance and J. B. Angell, "A batch-fabricated silicon accelerometer," *IEEE Transactions on Electron Devices*, vol. 26, no. 12, pp. 1911-1917, 1979.
- [6] B. Riedel, "Surface-machined Monolithic Accelerometer," *Analog Dialogue*, vol. 27, no. 2, pp. 3-7, 1993.
- [7] B. Bhushan, *Springer handbook of nanotechnology*. Springer Science & Business Media, 2010.
- [8] D. M. Stefanescu, *Handbook of force transducers: principles and components*. Springer Science & Business Media, 2011.
- [9] Z. Zhou, Z. Wang, and L. Lin, *Microsystems and nanotechnology*. Springer, 2012.
- [10] J. J. Allen, *Micro electro mechanical system design*. CRC Press, 2005.
- [11] M. J. Madou, *Fundamentals of microfabrication: the science of miniaturization*. CRC press, 2002.
- [12] "IEEE Standard for Inertial Sensor Terminology," *IEEE Std 528-2001*, 2001.
- [13] J. G. Webster and H. Eren, *Measurement, instrumentation, and sensors handbook: electromagnetic, optical, radiation, chemical, and biomedical measurement*. CRC press, 2014.

- [14] T. Li and Z. Liu, "Outlook and Challenges of Nano Devices, Sensors, and MEMS," ed: Springer, 2017.
- [15] S. Beeby, *MEMS mechanical sensors*. Artech House, 2004.
- [16] X. Jiang, K. Kim, S. Zhang, J. Johnson, and G. Salazar, "High-temperature piezoelectric sensing," *Sensors*, vol. 14, no. 1, pp. 144-169, 2013.
- [17] M. Vijaya, *Piezoelectric materials and devices: applications in engineering and medical sciences*. CRC Press, 2012.
- [18] J. C. Doll and B. L. Pruitt, *Piezoresistor design and applications*. Springer, 2013.
- [19] M.-H. Bao, *Micro mechanical transducers: pressure sensors, accelerometers and gyroscopes*. Elsevier, 2000.
- [20] W. Y. Du, *Resistive, capacitive, inductive, and magnetic sensor technologies*. CRC Press, 2014.
- [21] M. Bao, *Analysis and design principles of MEMS devices*. Elsevier, 2005.
- [22] Yole Développement, "High-End Gyroscopes, Accelerometers and IMUs for Defense, Aerospace & Industrial Report," Feb. 2015.
- [23] Yole Développement, "6&9-Axis Sensors Consumer Inertial Combos," Nov. 2014.
- [24] Colibrys, "Advantage of capacitive MEMS accelerometers vs other technologies," 2015.
- [25] E. K. Chan and R. W. Dutton, "Electrostatic micromechanical actuator with extended range of travel," *Journal of microelectromechanical Systems*, vol. 9, no. 3, pp. 321-328, 2000.
- [26] V. Kempe, *Inertial MEMS: principles and practice*. Cambridge University Press, 2011.
- [27] A. Selvakumar, F. Ayazi, and K. Najafi, "A high sensitivity z-axis torsional silicon accelerometer," in *Electron Devices Meeting, 1996. IEDM'96., International*, 1996, pp. 765-768: IEEE.
- [28] D. Xia, C. Yu, and L. Kong, "The development of micromachined gyroscope structure and circuitry technology," *Sensors*, vol. 14, no. 1, pp. 1394-1473, 2014.
- [29] S. S. Bhattacharyya, E. F. Deprettere, R. Leupers, and J. Takala, *Handbook of signal processing systems*. Springer Science & Business Media, 2013.
- [30] J. Turner, *Automotive sensors*. Momentum Press, 2009.
- [31] B. Wilamowski and J. D. Irwin, *The Industrial Electronics Handbook: Fundamentals of Industrial Electronics*. CRC Press, 2011.
- [32] H. R. Shea, "Reliability of MEMS for space applications," in *Moems-mems 2006 micro and nanofabrication*, 2006, pp. 61110A-61110A-10: International Society for Optics and Photonics.
- [33] Yole Développement, "Status of the MEMS Industery," Aug. 2016.
- [34] Yole Développement, "Status of the MEMS Industery," Apr. 2015.
- [35] Yole Développement, "Top 30 MEMS Companies 2010: Big four capture a third of the total MEMS market," Apr. 2011.
- [36] Yole Développement, "Technologies & Sensors for the Internet of Things," Jun. 2016.
- [37] Yole Développement, "Sensors for Wearable Electronics & Mobile Healthcare," Jul. 2015.

- [38] P. Zwahlen *et al.*, "Open-loop and closed-loop high-end accelerometer platforms for high demanding applications," in *Position, Location and Navigation Symposium (PLANS), 2016 IEEE/ION*, 2016, pp. 932-937: IEEE.
- [39] mCube Inc., "MC3216 3-Axis Accelerometer," 2014.

---

# Chapter 3

## Accelerometer Design Optimization in 2D Fabrication Processes

---

### 3.1 Introduction

Surface micromachined accelerometers are usually limited by their thin structures and light proof masses, and thus feature lower sensitivities compared to the devices fabricated using bulk micromachining. However, they still have attractive characteristics such as being easier to fabricate, high yields, and cost effectiveness, which keep them competing with bulk micromachined accelerometers for some key high-volume applications [1]. Surface micromachining also enables accelerometers to be integrated on the same die with their IC's, thereby reducing packaging complexity. Most of the MEMS accelerometers use the capacitive sensing scheme. This is because of this scheme's attractive features such as low power consumption, low voltage circuits, low dependency on temperature variations, and high sensitivity [2, 3].

For a device of a given fixed width, increasing the length of the sensing electrode will increase the capacitive sensing area. At the same time, however, it will reduce the area available for the proof mass responsible for bending the supporting beams and closing the capacitive gap between the electrodes. An optimum electrode length can provide improvement in the accelerometer sensitivity, at no cost in terms of fabrication process or layout. Several reported accelerometers use electrode lengths with rounded unexplained values (e.g. [4-6]). Reverse calculations of some reported designs reveal that the optimum electrode length has not been used and that achieving better sensitivities is feasible. In some cases, reaching the optimum length of the electrode of a capacitive accelerometer may be limited by the process characteristics, e.g., the residual stress limits. Otherwise, if no limitation is present, this optimum value method can be used to improve the sensitivity of the accelerometer.

This chapter introduces a method to achieve the best sensitivity when designing an in-plane differential varying gap capacitive accelerometer, especially for surface micromachined devices where the thickness limits the device sensitivity. The aim of this work is not to build high-performance accelerometers, but rather to demonstrate the feasibility and value of the proposed methodology. Moreover, since different and well-established surface micromachined 2D processes exist, the fabrication process is not developed here. The following section derives the model needed to optimize the variable parameters to achieve the maximum sensitivity, within a given sensor area. Next, a description is given of the commercial fabrication process used to verify the methodology. Then, the chapter reports simulations and test results that show the optimization and performance for different designs. Finally, the optimization method and the fabrication process are discussed, followed by conclusions in the last section.

### 3.2 Model Derivation

Figure 3.1 shows the design of a simple in-plane differential double-sided capacitive accelerometer. The main structure consists of anchored beams that support the proof mass. The sensing electrodes are long and thin beams that form two equal varying

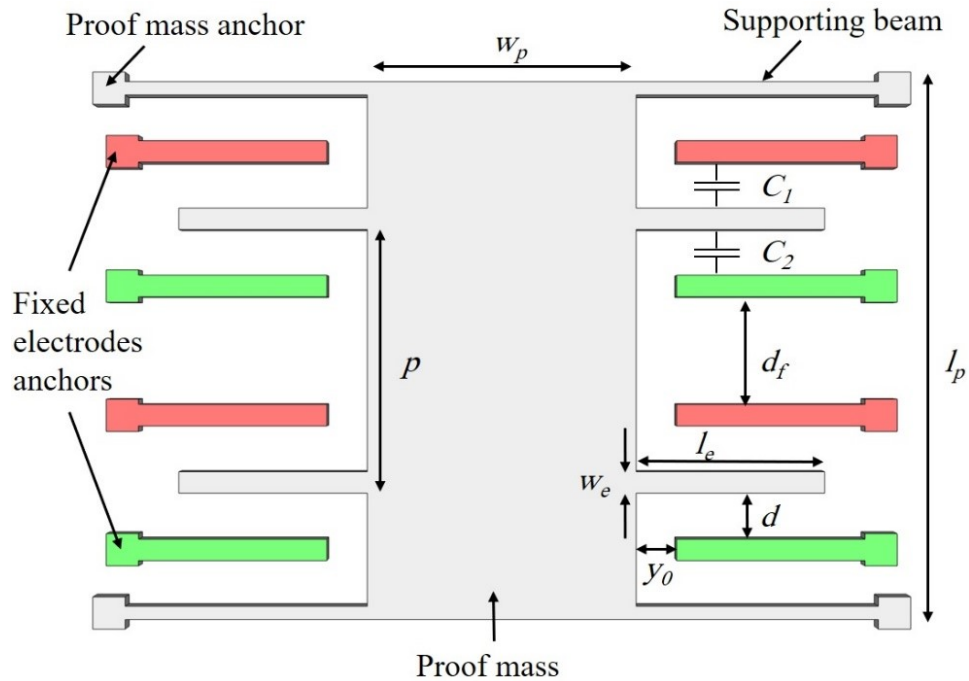


Figure 3.1: Differential double-sided capacitive accelerometer shape.

gap differential sensing capacitors,  $C_1$  and  $C_2$ . For a double-sided differential device with the same initial gap, and when ignoring the fringing field effects, the capacitive difference is given by:

$$C(x) = C_2 - C_1 = 2\varepsilon A \frac{x}{d^2 - x^2}, \quad (3.1)$$

where  $\varepsilon$  is the permittivity of the medium between the electrodes,  $A$  is the capacitive area,  $d$  is the initial gap, and  $x$  is the displacement after acceleration. By taking the derivative of (3.1), the capacitance change per unit displacement, or the capacitive sensitivity  $S_C$  is:

$$S_C = \frac{\Delta C(x)}{\Delta x} = 2\varepsilon A \frac{d^2 + x^2}{(d^2 - x^2)^2}. \quad (3.2)$$

The displacement per unit acceleration, or mechanical sensitivity  $S_M$ , can be found using Hooke's law:

$$S_M = \frac{\Delta x}{\Delta a} = \frac{m}{k}, \quad (3.3)$$

where  $\Delta x$  is the displacement change,  $\Delta a$  is the acceleration change,  $m$  is the proof mass, and  $k$  is the spring constant. The device proof mass is given by:

$$m = \rho h(l_p w_p + 2N l_e w_e), \quad (3.4)$$

where  $\rho$  is the density;  $h$  is the thickness;  $N$  is the number of sensing electrodes per side; and  $l_p$ ,  $w_p$ ,  $l_e$ , and  $w_e$  are the lengths and widths of the proof mass and any of the sensing electrodes, respectively. The total spring constant,  $k$ , for four parallel clamped-guided straight supporting beams with length  $l_k$  and width  $w_k$  is given by [7]:

$$k = \frac{E w_k^3 h}{l_k^3}. \quad (3.5)$$

For simplicity of derivation, the offset  $y_0$  between the proof mass and the sensing electrodes is ignored, and all of the electrode length is used in computing the capacitance change. For more accurate results, however, the term  $l_e$  should be equal to the actual sensing length. When the device contains structure release holes, their areas and effects should also be included in the proof mass expression described in (3.4). The capacitance

change due to the input acceleration is then obtained by multiplying the capacitive sensitivity by the mechanical sensitivity ( $A=2Nhl_e$ ):

$$S = S_C S_M = \frac{\Delta C(x)}{\Delta x} \frac{\Delta x}{\Delta a} = 4N\epsilon h l_e \frac{d^2 + x^2}{(d^2 - x^2)^2} \frac{m}{k}. \quad (3.6)$$

The total sensitivity is the capacitance change per unit input acceleration. It is possible to express the displacement change in terms of acceleration to remove the unknown  $x$  in the equation. When  $d$  is much larger than  $x$ , the capacitive sensitivity per unit acceleration  $a$  can be approximated to:

$$S = \frac{4N\epsilon h l_e}{d^2} \frac{m}{k}. \quad (3.7)$$

The capacitive sensitivity and the mechanical sensitivity are inversely correlated, and increasing the electrodes lengths will decrease the total proof mass. For a certain total device width,  $w_T$ , there exists an optimum electrode length,  $l_{opt}$ , which yields the highest sensitivity. The maxima of (3.7) can be found by taking the derivative with respect to  $l_e$  and then solving for  $l_e$  (notice in (3.4) that  $m$  depends on  $l_e$ ).

When the spring constant is independent of the electrode length and  $y_0$  is much smaller than  $l_e$ , the electrode length that gives the maximum sensitivity for a single or double-sided device can be given by:

$$l_{opt} = \frac{w_T p}{4(p - w_e)}, \quad (3.8)$$

where  $p$  is the pitch between the sensing electrodes, and the total width,  $w_T$ , is:

$$w_T = w_p + 2l_e. \quad (3.9)$$

For devices with any number of straight spring beams that have the exact same lengths as the sensing electrode, and where  $y_0$  is much smaller than  $l_e$ , the best sensitivity can be achieved when the electrode length is set to:

$$l_{opt} = \frac{2w_T p}{5(p - w_e)}. \quad (3.10)$$

For other configurations, the optimum value can be found by sweeping  $l_e$  versus  $S$  in (3.11) below, then finding the optimum value from the obtained curve.



$$S = \frac{4N\varepsilon h l_e}{d^2} \frac{m(l_e)}{k(l_e)}. \quad (3.11)$$

The other parameter to be optimized is the width of the electrode, which also controls the pitch value. The pitch value can be evaluated as:

$$p = 3w_e + d + d_f, \quad (3.12)$$

where  $d$  is the sensing gap between any fixed electrode and the moving electrode, and  $d_f$  is the gap between the two adjacent fixed electrodes, as shown in Figure 3.1. The electrode width may be minimized to increase the number of electrodes and hence the sensitivity. Yet, it should not reach a value that allows the electrode to bend due to the applied voltage. Furthermore, the electrode length should not reach the value at which the electrodes snap down to each other due to the electric potential of the readout circuit. As a sanity check, their lengths should not reach the maximum allowed electrode length for a certain electric potential [8]:

$$l_e = l_a + w_e d \sqrt{\frac{E}{18l_a \varepsilon V^2}}, \quad (3.13)$$

where  $l_a$  is the electrodes' overlap length and  $V$  is the electric potential. If the optimized value is larger than the maximum length before snap-down, the electrodes' width can be increased or their lengths can be decreased.

### 3.3 Accelerometer Design and Fabrication Process

To confirm the optimization method proposed, two accelerometer designs with five different variations of each design were fabricated in the commercial process PolyMUMPs provided by MEMSCAP [9]. Table 3.1 lists the main design parameters used in these variations. All designs occupied the same area of  $500 \times 500 \mu\text{m}^2$  with a 2- $\mu\text{m}$  structural layer thickness. There were 13 differential capacitive electrodes on each side, with 2  $\mu\text{m}$  capacitive gaps and a 35- $\mu\text{m}$  pitch between the sensing electrodes. The proof mass was suspended using four supporting beams, and each beam measured 2  $\mu\text{m}$  in width. The first design had four supporting beams that had the same length as the sensing electrodes. The

Table 3.1: Summary of the main design parameters.

Device size ( $\mu\text{m}^2$ )	$500 \times 500$
Device thickness ( $\mu\text{m}$ )	2
Gap, $d$ ( $\mu\text{m}$ )	2
Electrode width, $w$ ( $\mu\text{m}$ )	8
Number of sense electrodes per side	13
Pitch, $p$ ( $\mu\text{m}$ )	35
Supporting beam width, $w_k$ ( $\mu\text{m}$ )	2

second was a proof mass suspended by four supporting beams each with a length equivalent to half the width of the proof mass.

PolyMUMPs is a 3D surface micromachining process that utilizes three polysilicon layers for structures and interconnects. It also has two sacrificial oxide layers and a metallic layer that is used to bond or probe the devices. Because the design is simple, only two polysilicon layers and one sacrificial layer were used to build the devices. Figure

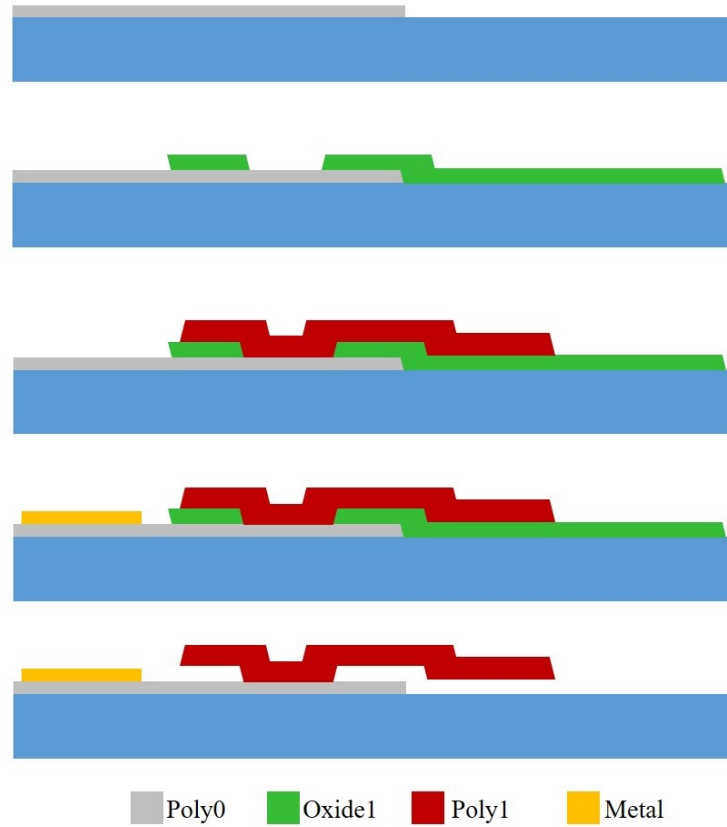


Figure 3.2: The used steps from the PolyMUMPs process.

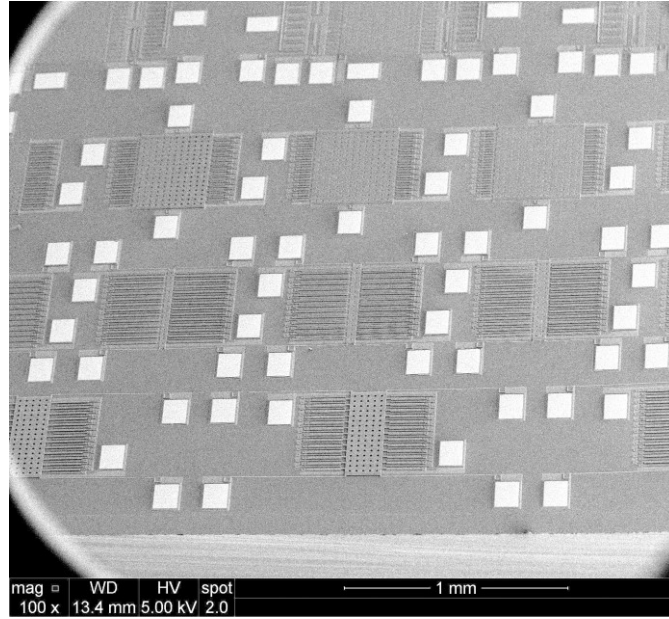


Figure 3.3: SEM image of the different variations.

3.2 shows the process flow of the used layers. To make the interconnects, the Poly0 layer was deposited on a wafer covered with an insulating nitride layer. After patterning it, the first oxide layer was then used to define anchors and create a sacrificial layer. Poly1 is the main structural layer used in this process, and the whole accelerometer structure was created within this layer. Finally, the metal layer was used to create bonding pads for the three electrode sets. To release the structure, post-processing wet etching was needed; this was done by immersing the chips in a 49% HF solution to etch the oxide layers. Figure 3.3 shows a scanning electron microscope (SEM) image of the variations for the two designs.

### 3.4 Method Verification

The fabricated devices were tested using a rotary motion simulator that created a fixed centripetal force. The resulting differential capacitance was measured using an AD7746 capacitance to digital converter (CDC) [10]. The applied acceleration was increased gradually to acquire readings that were clearly resolvable from each other. As an additional confirmation method, FEM simulations for all the variations were performed using Comsol. Some readings were measured on different dies because the wet release of the devices had caused visible deformation for some devices.

Figure 3.4 (a) shows one device of the first design that had five variations with the following electrode lengths: 210, 220, 230, 235, and 240  $\mu\text{m}$ . Because of the small mass and the low sensitivity, high accelerations were needed to deliver readings that could be differentiated from each other. At 10 g acceleration, all five variations yielded distinguishable readings that followed the expected trend, as shown in Figure 3.4 (b).

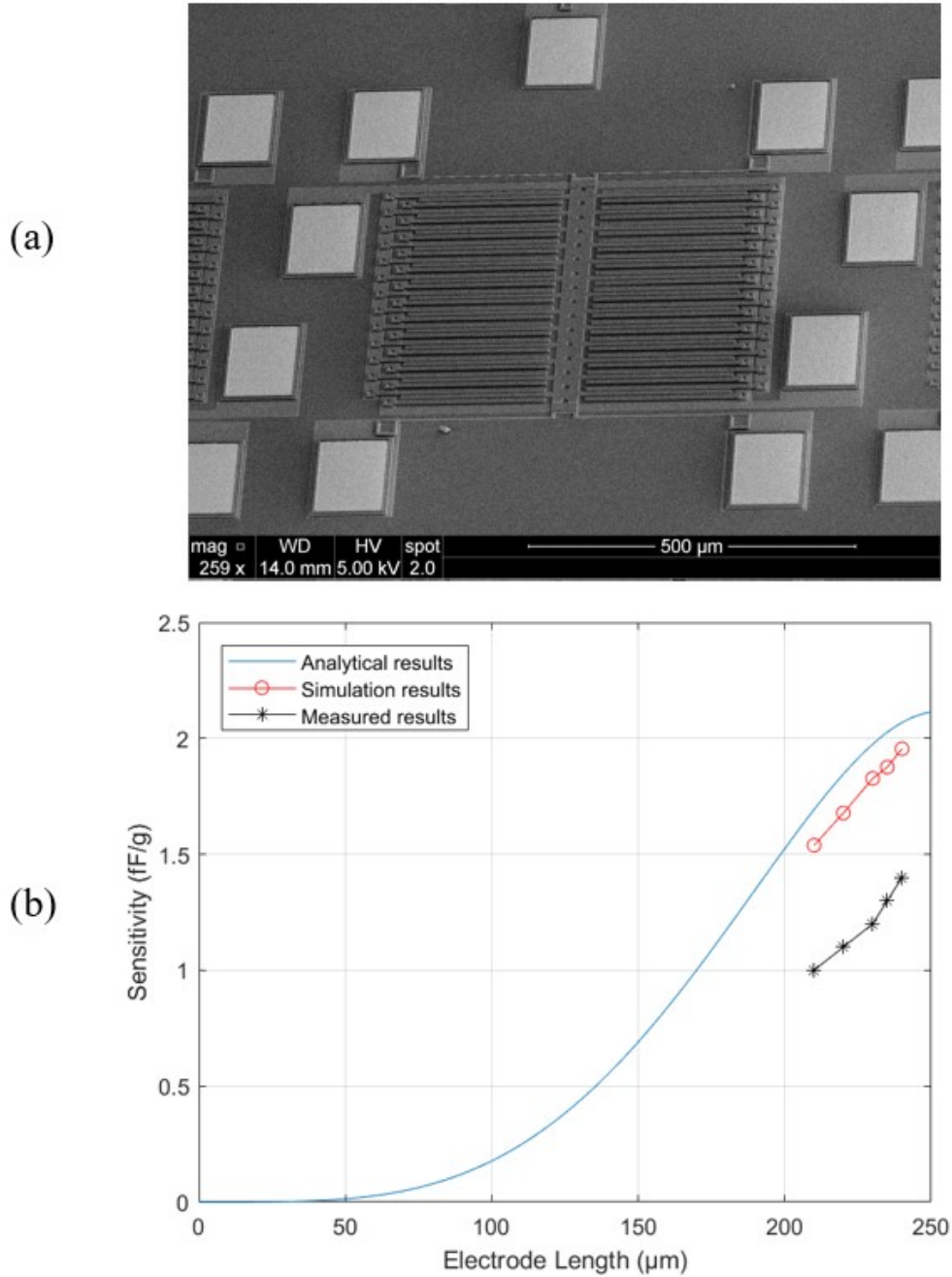


Figure 3.4: The first design (a) SEM image, and (b) optimization curve.

The second design shown in Figure 3.5 (a) has stiffer suspension beams and a smaller capacitive sensing area, and hence was expected to have lower sensitivity than the first design. The different variations had the following electrode lengths: 40, 50, 60, 80 and 100  $\mu\text{m}$ . Even after applying a 10-g acceleration, it was possible to see a resolvable output from only four out of the five variations (Figure 3.5 (b)).

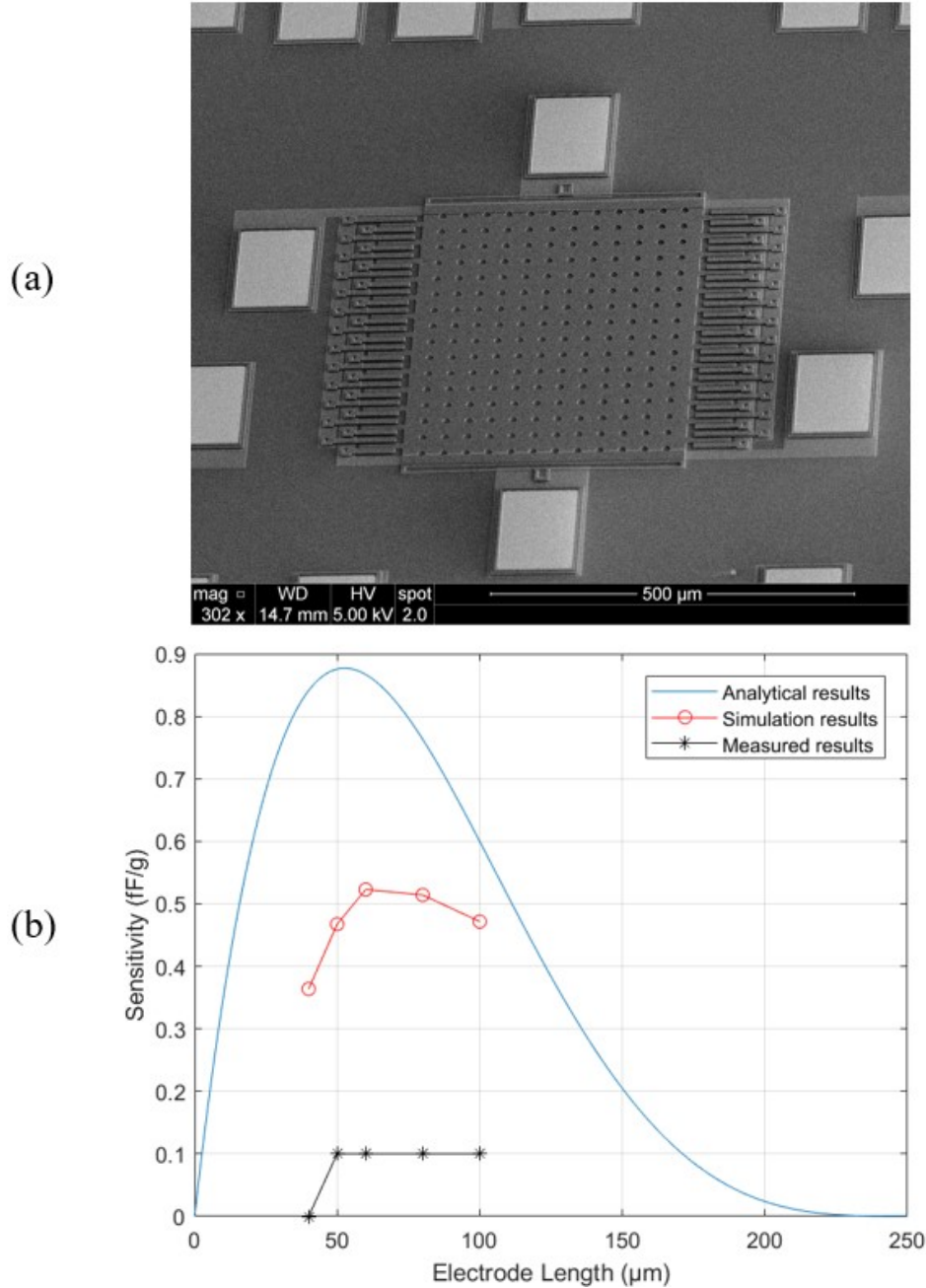


Figure 3.5: The second design (a) SEM image, and (b) optimization curve.

### 3.5 Discussion

The first design simulations and readings showed the sensitivity trends expected when the electrode length was increased. For the second design, however, the readings could only be obtained from four variations that reported the same value because of the limited resolution of the reading electronic CDC (capacitance-to-digital converter). However, the simulations showed the projected trends for sensitivity curve from the five variations. It is also noted that the analytical model is not precise in terms of the resulting sensitivity values for both the simulations and measurements. This issue is attributed to the parallel-plate formula used to calculate the capacitance, which does not take into account the fringing fields [11, 12]. Even though the optimum length value found using this formula remains valid, the Palmer formula could be used for a more accurate sensitivity projection [12, 13]. The measured sensitivities were lower than the simulated ones, probably due to the ideal material properties that were used in simulations, e.g. it was assumed that there were no residual stresses in the different layers.

To impart the improvement that could be obtained using the method proposed here, it was applied to some designs using their reported parameters. Table 3.2 lists the design parameters and performances of five published works that used electrode lengths rounded to the nearest hundred. As shown, some devices did not use the optimum electrode length that would have given the maximum sensitivity from the used area. It can also be seen that, depending on the design and the sensor size, the improvement can be important. As the

Table 3.2: Sensitivity improvement of published designs when optimized.

Parameter	[14]	[15]	[16]	[17]	[18]
Device area (mm <sup>2</sup> )	0.09	10.8	25	2	2
Device thickness (μm)	4	25	50	25	20
Gap, $d$ (μm)	0.5	2.25	2.2	2.5	8
Electrode length (μm)	90	600	500	300	300
<b>Sensitivity (fF/g)</b>	<b>1.73</b>	<b>82.68</b>	<b>913</b>	<b>109.7</b>	<b>0.539</b>
Optimum electrode length (μm)	93	814	762	313	332
<b>Optimized sensitivity (fF/g)</b>	<b>1.78</b>	<b>88.23</b>	<b>1035</b>	<b>109.9</b>	<b>0.544</b>
<b>Sensitivity improvement (%)</b>	<b>2.9</b>	<b>6.8</b>	<b>13.4</b>	<b>0.18</b>	<b>0.91</b>

accelerometer size and gap decrease, using the optimum value could be critical, and a 3- $\mu\text{m}$  difference could bring about 3% improvement to the design described in [14]. On the other hand, a 32- $\mu\text{m}$  difference from the optimum value reduced the sensitivity in [18] by less than 1% because of the accelerometer's larger size and wide gap. The electrode length in the unoptimized designs might be restricted by the layers stress such that if longer electrodes are used they would curl and, hence, do not create the expected capacitance with the fixed electrodes.

### 3.6 Conclusion

This chapter has presented a methodology to achieve the maximum sensitivity for an in-plane closing-gap capacitive accelerometer. By using this method, the time and effort needed to find the optimum design parameters are reduced. Different variations of two designs were fabricated in a commercial PolyMUMPs process. Due to the limited area in the fabricated dies, it was not feasible to add other designs to be tested. However, measurements and simulations confirmed the effectiveness of the methodology to find the optimum electrode length at which the highest sensitivity is obtained. The testing could be made easier by using smaller finger widths or by using another process with a thicker structural layer for more accurate readings.

### 3.7 References

- [1] M. J. Madou, *Fundamentals of microfabrication: the science of miniaturization*. CRC press, 2002.
- [2] J. Chae, H. Kulah, and K. Najafi, "A hybrid silicon-on-glass (SOG) lateral micro-accelerometer with CMOS readout circuitry," in *Micro Electro Mechanical Systems, 2002. The Fifteenth IEEE International Conference on*, 2002, pp. 623-626: IEEE.
- [3] N. Maluf, "An introduction to microelectromechanical systems engineering," ed: IOP Publishing, 2002.
- [4] M. Benmessaoud and M. M. Nasreddine, "Optimization of MEMS capacitive accelerometer," *Microsystem Technologies*, vol. 19, no. 5, pp. 713-720, 2013.
- [5] P. Monajemi and F. Ayazi, "Design optimization and implementation of a microgravity capacitive HARPSS accelerometer," *IEEE Sensors Journal*, vol. 6, no. 1, pp. 39-46, 2006.
- [6] H. Hamaguchi, K. Sugano, T. Tsuchiya, and O. Tabata, "A differential capacitive three-axis SOI accelerometer using vertical comb electrodes," in *Solid-State Sensors, Actuators and Microsystems Conference, 2007. TRANSDUCERS 2007. International*, 2007, pp. 1483-1486: IEEE.

- [7] W. C. Young and R. G. Budynas, *Roark's formulas for stress and strain*. McGraw-Hill New York, 2002.
- [8] B. Konoplev, I. Lysenko, and O. Ezhova, "Assessment criterion of rigidity of comb electrodes fingers of microelectromechanical converters," *Modern Applied Science*, vol. 10, no. 2, p. 52, 2015.
- [9] A. Cowen, B. Hardy, R. Mahadevan, and S. Wilcenski, "PolyMUMPs design handbook," *Memscap Inc*, vol. 13, 2011.
- [10] Analog Devices Inc., "24-bit Capacitance-to-Digital Converter with Temperature Sensor, AD7745/AD7746," 2005.
- [11] S. Catalan-Izquierdo, J.-M. Bueno-Barrachina, C.-S. Cañas-Peñuelas, and F. Cavallé-Sesé, "Capacitance evaluation on parallel-plate capacitors by means of finite element analysis," in *International Conference on Renewable Energies and Power Quality (ICREPQ)*, 2009.
- [12] M. Hosseini, G. Zhu, and Y.-A. Peter, "A new formulation of fringing capacitance and its application to the control of parallel-plate electrostatic micro actuators," *Analog Integrated Circuits and Signal Processing*, vol. 53, no. 2, pp. 119-128, 2007.
- [13] H. B. Palmer, "The capacitance of a parallel-plate capacitor by the Schwartz-Christoffel transformation," *Electrical Engineering*, vol. 56, no. 3, pp. 363-368, 1937.
- [14] A. R. Chaudhuri, S. Severi, M. A. Erismis, L. Francis, and A. Witvrouw, "SiGe MEMS accelerometers combining a large bandwidth with a high capacitive sensitivity," *Procedia Engineering*, vol. 47, pp. 742-745, 2012.
- [15] B. Mukherjee, K. Swamy, T. D. Krishnan, and S. Sen, "A simple low cost scheme for closed loop operation of MEMS capacitive accelerometer," in *Students' Technology Symposium (TechSym), 2014 IEEE*, 2014, pp. 111-115: IEEE.
- [16] B. V. Amini and F. Ayazi, "Micro-gravity capacitive silicon-on-insulator accelerometers," *Journal of micromechanics and microengineering*, vol. 15, no. 11, p. 2113, 2005.
- [17] K. K. Mistry, K. Swamy, and S. Sen, "Design of an SOI-MEMS high resolution capacitive type single axis accelerometer," *Microsystem technologies*, vol. 16, no. 12, pp. 2057-2066, 2010.
- [18] P. Qu and H. Qu, "Design and characterization of a fully differential MEMS accelerometer fabricated using MetalMUMPs technology," *Sensors*, vol. 13, no. 5, pp. 5720-5736, 2013.



---

# Chapter 4

## Dual-Axis Capacitive Accelerometer with Low Cross-Sensitivity

---

### 4.1 Introduction

Single-axis accelerometers have sufficient performance for many applications. However, when multi-axis accelerations need to be measured, several single-axis accelerometers have to be integrated together onto the same chip, leading to an increase in chip size and cost. There are several applications for dual-axis accelerometers, ranging from smartphones to automotive applications. Specifically, these devices are mostly used to sense the presence or absence of motion in a reference plane, e.g., detection of tilt for a stationary object (Figure 4.1) [1]. In such systems, sensitivity in the two in-plane axes is usually more important than in the third out-of-plane axis. A proposed application for the device introduced here is in land and other planetary navigation, where acceleration is usually measured in two dimensions and it is thus more appropriate to use dual-axis accelerometers. In such applications, the use of tri-axis accelerometers would be more costly than necessary. One of the lowest cost land navigation configurations consists of using a single-axis gyroscope and a dual-axis accelerometer [2-4].

In general, in multi-axis accelerometers, the sensing electrodes have one degree-of-freedom (DOF) while the proof mass has multiple DOFs. Accordingly, a design challenge in multi-axis accelerometers concerns the cross-sensitivity between different inputs. Some designs have overcome this challenge by utilizing more than one proof mass [5, 6]. Notably, single-axis accelerometers have been demonstrated to achieve low cross-sensitivity measurements, typically less than 1%, while the cross-sensitivities of multi-axis accelerometers are larger, usually in the order of 2% or more [7-10]. This difference is inherently due to the structural design of these multi-axis accelerometers, making them

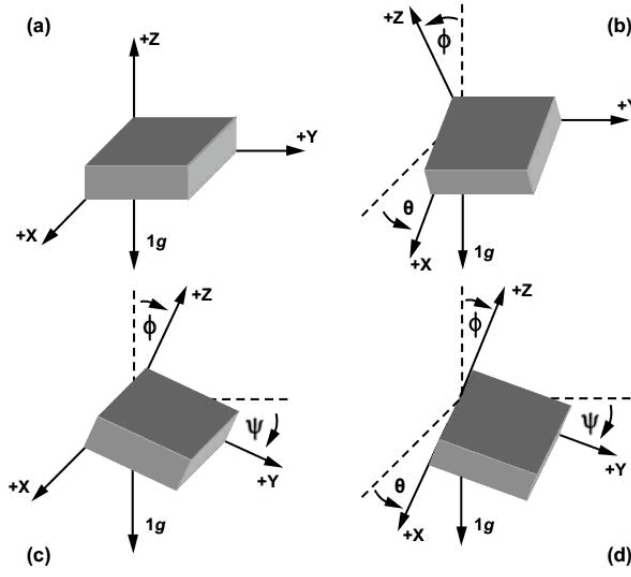


Figure 4.1: Inclination angle detection using a dual accelerometer [1].

sensitive in more than one axis. The device presented in this work aims to minimize such cross-sensitivity in dual-axis accelerometers.

This chapter introduces an integrated accelerometer system that uses a novel low cross-sensitivity dual-axis sensing accelerometer structure. The accelerometer is interfaced with commercial CDCs to achieve digital outputs for both axes within a system in package (SiP) solution. The accelerometer structure mechanically decouples the X- and Y-axes' input accelerations, enabling acceleration magnitude and angle sensing while not being affected by Z-axis accelerations. The device is fabricated in the silicon-on-insulator (SOI) technology offered by MEMSCAP, namely the SOIMUMPs process [11]. A 4-g linear range is targeted, along with a <1% cross-sensitivity. These specs are well suited for applications such as automotive stability systems that can require a  $\pm 2$  g range, <10 mg minimum detectable signal, and <5% cross-sensitivity [12, 13]. First, the chapter provides an overview of the design and operating principle of the device for both acceleration and angle sensing, along with the relevant design parameters. Next, the device fabrication in a commercial process is discussed with SEM photographs of the fabricated device. Then the chapter presents the simulation and test results, followed by a discussion of the device performance. Finally, the feasibility of porting the design to an in-house surface micromachining process is reviewed in the conclusion.

## 4.2 Design Overview

The mechanical structure of the accelerometer proposed here consists of four fixed electrodes with comb fingers and four proof masses anchored at the center, as shown in Figure 4.2. The proof mass fingers are slightly shifted from the center of the gap between the fixed electrode fingers, as shown in Figure 4.3. This shift is important because, if the moving electrodes were centered, the amount of capacitance change would be the same on both sides of the moving electrodes, and the direction of acceleration could not be determined. Under no acceleration, the gap between the electrodes is uniform, as shown in Figure 4.3 (a). As the device is subjected to acceleration, the proof masses exhibit a small rotational displacement which can be approximated to be similar to a linear motion. Due to this motion, the gap between the electrodes will vary, as shown in Figure 4.3 (b). Since the sensing scheme is based on a variable-gap capacitance, the capacitance value will be integrated over the whole gap of the electrode for each comb finger.

The SOIMUMPs fabrication technology was selected because its device layer is made of highly doped silicon, which provides good electrical and mechanical properties for use in implementing moving capacitive electrodes. The silicon thickness is also relatively large (i.e. 25  $\mu\text{m}$ ), which enhances the capacitance area of the device and thus its sensitivity. The capacitive gap between the proof mass and the fixed electrode fingers is 3  $\mu\text{m}$ . This gap size is limited by the fabrication process through specific design rules. The device is limited by design to an overall size of 1 mm  $\times$  1 mm, to minimize its footprint.

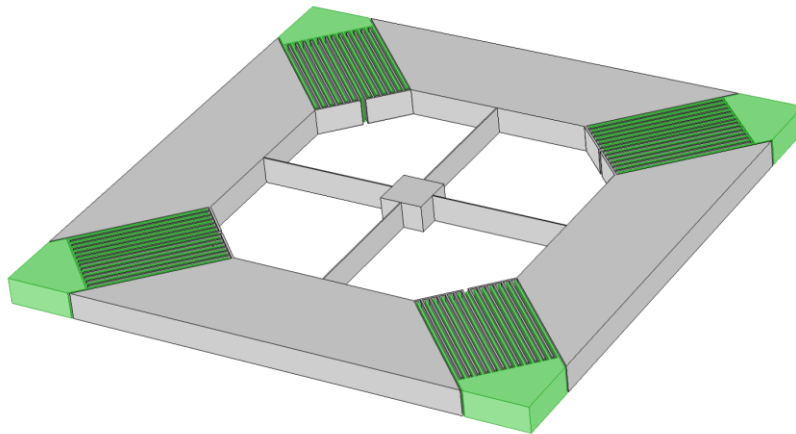


Figure 4.2: 3D model of the device where the fixed electrodes are shown in green.

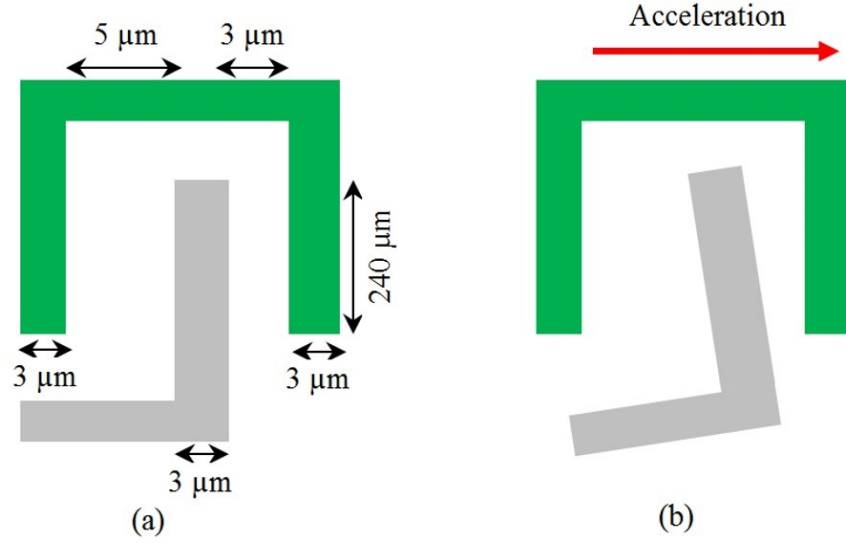


Figure 4.3: Representation of a fixed electrode (green) and the proof mass electrode (grey) (a) before, and (b) after movement.

Pads are present on the central anchor and at the device corners, to ensure electrical connections to the proof masses and to the fixed electrodes, respectively.

The proof masses move only in the lateral directions (i.e. the X- or Y-axis, as shown in Figure 4.4). Each proof mass will exhibit a force caused by the acceleration given by:

$$F = ma = kx, \quad (4.1)$$

where  $m$  is the mass,  $a$  is the acceleration,  $k$  is the spring constant, and  $x$  is the beam's tip displacement.

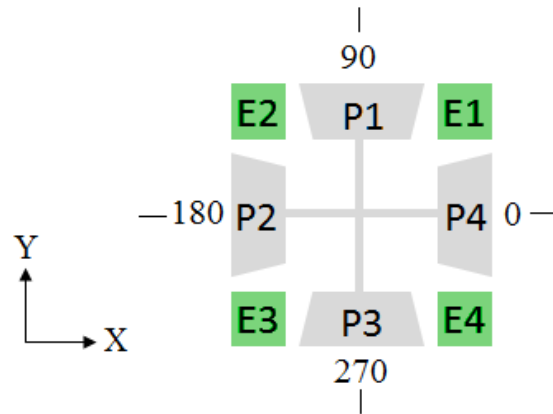


Figure 4.4: Simplified representation of the accelerometer.

The spring constant of each beam in the lateral direction is given by [14, 15]:

$$k = \frac{Ew^3h}{4l^3}, \quad (4.2)$$

where  $E$  is Young's modulus,  $w$  is the width of the beam,  $h$  is its thickness, and  $l$  is its length.

Figure 4.4 shows a simplified model of the device where the proof masses (in grey) are denoted with the letter  $P$  and numbered from 1 to 4. Note that these are electrically connected through the silicon central beams. The fixed electrodes are denoted with the letter  $E$  and numbered from 1 to 4.

Under acceleration, the proof masses will tend to move in a circular trajectory because of the design geometry. When the device experiences acceleration in the X-axis, the lateral X displacements of  $P1$  and  $P3$  will be much larger than their Y displacements. Therefore, the overall displacement can be considered to be in the X direction only. The same applies to the Y acceleration and the displacements of  $P2$  and  $P4$ .

When the device exhibits acceleration in the X-axis,  $P1$  and  $P3$  will be subjected to the same force and will have the same displacement in the X-axis. The resulting differential capacitance,  $\Delta C_X$ , is:

$$\Delta C_X = (C_{P1E1} + C_{P3E4}) - (C_{P1E2} + C_{P3E3}), \quad (4.3)$$

where  $C_{PIEI}$  denotes the capacitance between  $PI$  and  $EI$ . Any capacitance changes resulting from the displacements of  $P2$  and  $P4$  in the Y-axis will not affect  $\Delta C_X$ , because this capacitance variation will be equal for both of these masses, and will therefore be cancelled by the differential measurement setup. Similarly, for the acceleration in the Y-axis,  $\Delta C_Y$  is given by:

$$\Delta C_Y = (C_{P2E2} + C_{P4E1}) - (C_{P2E3} + C_{P4E4}). \quad (4.4)$$

Table 4.1: Summary of the design parameters and noise performance.

Nominal capacitance per axis, $C_0$ (pF)	1.05
Gap, $d$ ( $\mu\text{m}$ )	3
Beam length, $l$ ( $\mu\text{m}$ )	260
Beam width, $w$ ( $\mu\text{m}$ )	3
Lateral spring constant per beam, $k$ (N/m)	1.6
BNEA (at 27° C) ( $\mu\text{g}/\sqrt{\text{Hz}}$ )	3.48

The total differential capacitance,  $\Delta C_{TOTAL}$ , resulting from an arbitrary acceleration will be the resultant vector from the X and Y capacitances. The acceleration angle  $\theta$  can then be calculated using vector relations, i.e.:

$$\Delta C_{TOTAL} = \sqrt{\Delta C_X^2 + \Delta C_Y^2}, \text{ and} \quad (4.5)$$

$$\theta = \tan^{-1} \left( \frac{\Delta C_Y}{\Delta C_X} \right). \quad (4.6)$$

By using a softer beam (e.g. a thinner structure), the proof mass can be made smaller such that the overall area of the device can be minimized. A constraint of a maximum device size of 1 mm<sup>2</sup> was imposed here. The major design parameters and resulting performance metrics are listed in Table 4.1.

The Brownian noise equivalent acceleration (BNEA) of this device at room temperature and under atmospheric air pressure is lower than the targeted minimum sensitivity, thereby ensuring that the sensitivity specification will be met and will not be deteriorated [16]:

$$BNEA = \sqrt{\frac{4k_B T D}{m^2}}, \quad (4.7)$$

where  $k_B$  is the Boltzmann constant,  $T$  is the temperature in Kelvin,  $D$  is the damping coefficient, and  $m$  is the mass.

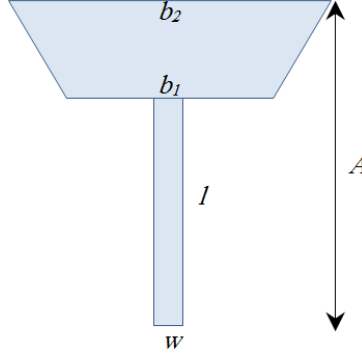


Figure 4.5: Top view of a beam and proof mass design parameters.

Starting from the recommended minimum feature size of  $3\text{ }\mu\text{m}$  for the beam width, the design parameters are found using equation (4.1) and illustrated in Figure 4.5, such that:

$$ma = \rho \left( \frac{1}{2} h[b_1 + b_2] \cdot [A - l] \right) a = kx, \quad (4.8)$$

where  $\rho$  is the density of the device layer,  $b_1$  and  $b_2$  are the sides of the trapezoid, and  $A$  is half of the device side length. Using (4.2), equation (4.8) can be rewritten as:

$$\rho \left( \frac{1}{2} h[b_1 + b_2] \cdot [A - l] \right) a = \left( \frac{Ew^3h}{4l^3} \right) x. \quad (4.9)$$

For a  $1 \times 1\text{ mm}^2$  device size, all the known parameters except for  $x$  and  $l$  are defined. By rearranging the equation to isolate  $x$  as a function of  $l$ , i.e.  $x(l)$ , and taking the derivative of  $x(l)$  and solving for  $l$ , the optimal beam length,  $l_{opt}$ , that gives maximum deflection,  $x$ , can be calculated.

### 4.3 Device Fabrication

The device reported here was fabricated in the SOIMUMPs process. This process is based on a  $25\text{ }\mu\text{m}$  silicon layer insulated by a  $2\text{ }\mu\text{m}$  oxide layer above the  $400\text{ }\mu\text{m}$  silicon substrate. A phosphosilicate glass (PSG) layer is then deposited and the wafer is annealed to drive phosphorous dopants into the  $25\text{ }\mu\text{m}$  silicon layer. This makes the layer sufficiently conductive. The gold pad layer is then deposited and patterned to make contacts for the device.

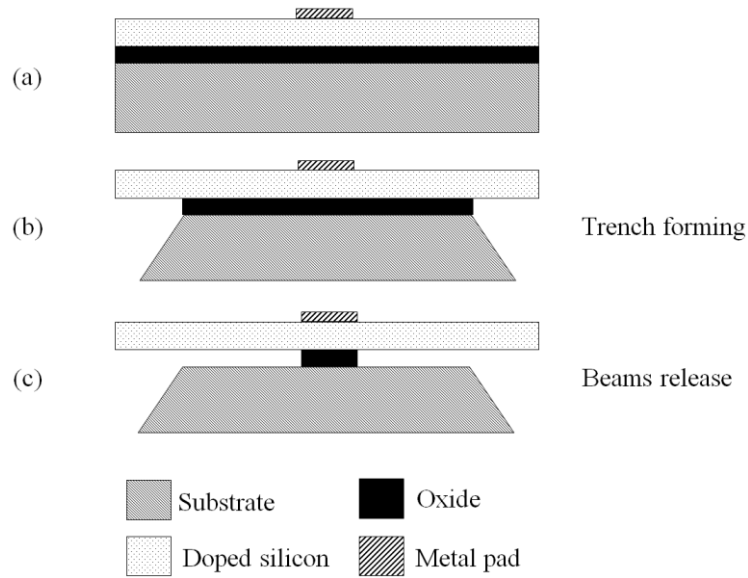


Figure 4.6: Cross-section of the beam release process.

For this device, the fixed electrodes, the beams, and the central anchor are formed using the 25  $\mu\text{m}$  silicon layer. The proof masses are released by forming a trench in the underlying substrate area. This exposes the oxide to a vapor HF release at the manufacturing facility. However, the SOIMUMPs process does not allow for a trench to be created under the entire structure, namely under the central beams. As such, a post-processing step is performed in-house to ensure the release of the central beams by etching the oxide laterally using an HF-based liquid etchant [17]. This step enables the free movement of the beams and the proof masses. Since the oxide area underneath the central anchor is much larger than that under the beams, it will only be etched partially if the release time is selected appropriately, allowing for the proof masses to remain supported at the center after this release, as shown in Figure 4.6. Figure 4.6 (a) shows the device after the deposition and patterning of all of the layers and pads. The substrate and oxide underneath the proof masses is then removed by a dry process, as shown in Figure 4.6 (b). The post-processing etching step is shown in Figure 4.6 (c), where the 2- $\mu\text{m}$  oxide underneath the support beams is removed.



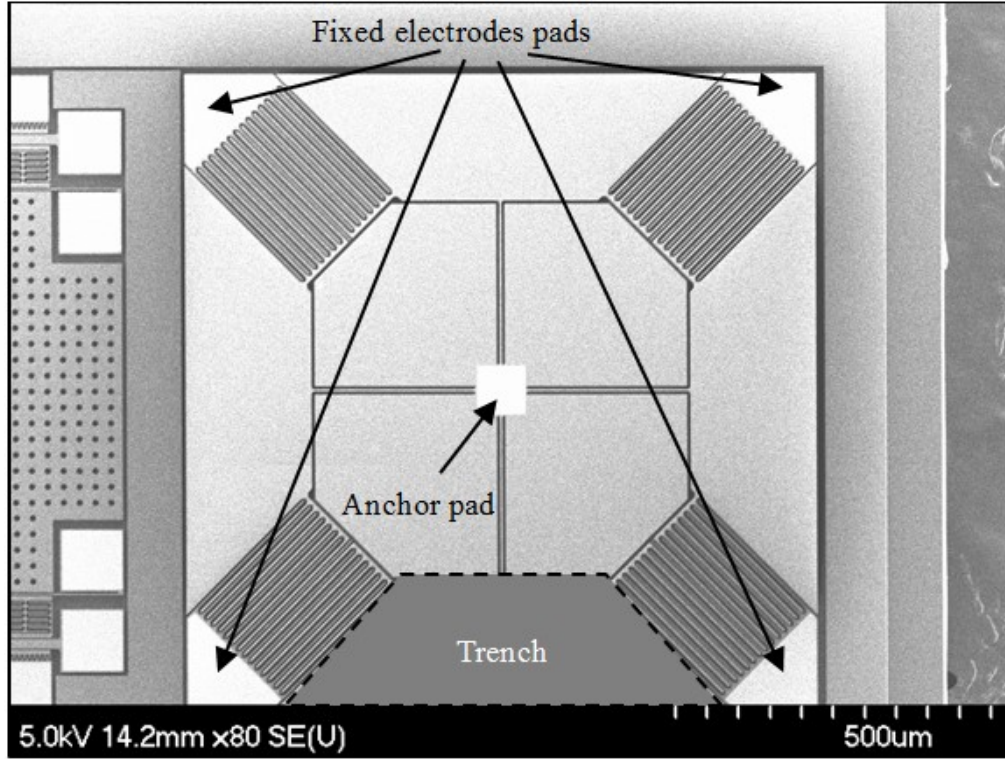


Figure 4.7: SEM image of the fabricated accelerometer.

Figure 4.7 shows the device after fabrication. The metal pads used for device-to-interface connections are placed at each corner of the device to contact the fixed electrodes, and at its center to contact the electrodes of the proof masses. The dotted grey area is the trench location under each proof mass (only shown for the bottom proof mass). Notably, the areas around the central anchor and between the central beams were filled with silicon to prevent it from being under etched during the in-house HF post-release step.

To check the release of the structure, a positive DC voltage was applied to the electrodes of the accelerometer to examine the free movement of its parts. Current was limited by putting a resistor in series with the voltage source, protecting against the destruction of the device in case of direct contact between the electrodes. The transmission coefficient ( $S_{21}$ ) of the device at two different voltages is plotted in Figure 4.8, showing that the device was properly released and thus responded to a DC voltage. As the frequency increased from 500Hz, the transmission coefficient increased until it reached a peak at the natural resonance frequency of the device. Transmission then decreased back as the frequency increased and moved away from the resonance peak, until the parasitic

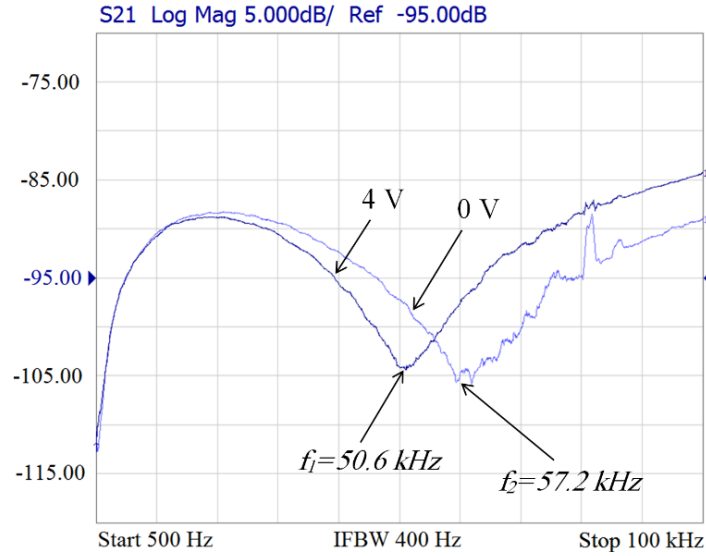


Figure 4.8: Forward transmission coefficient (S21) plot at different accelerometer bias voltages outlining proof mass motion.

feedthrough capacitances started dominating (@ 50.6 kHz), resulting in a monotonic increase in S21 at higher frequencies. Stiction was sometimes observed between the moving electrodes and the fixed electrodes due to the applied electrostatic force. That could be resolved by simply applying a negative voltage for a short time to eliminate the accumulated trapped charges.

## 4.4 Device Characterization

### 4.4.1 Simulation Results

The design introduced here was simulated using finite element methods via the CoventorWare suite of tools. Table 4.2 shows simulated device characteristics at different

Table 4.2: Simulation results.

Parameter	Acceleration Angle (°)		
	0°	22.5°	45°
Sensitivity (fF/g)	25.85	25.20	24.61
Max. cross-sensitivity (%)	0.48	-	-
Nonlinearity (%)	3.7	2.6	1.8
Alignment error (°)	0.27	1.6	0.49
Resonance frequency (Hz)	1137	1137	1137

acceleration angles over the range from 0 g to 4 g. The sensitivity varies by a maximum of 1.24 fF across the angle range of  $45^\circ$ . Note that better sensitivity can be obtained by using larger device dimensions, beyond the targeted  $1\text{ mm} \times 1\text{ mm}$  size. The XY cross-sensitivity changes with the input acceleration, and its maximum value is 0.48% at a 3.7-g, as shown in Figure 4.9.

As shown above, the device is symmetric and has equal sensitivities in the X- and Y-axes. Note that the angles of  $0^\circ$  and  $90^\circ$  represent the positive X-axis and the positive Y-axis directions, respectively. When the acceleration angle changes, the nonlinearity decreases until it reaches its minimum at an angle of  $45^\circ$ , at which all the proof masses have the same displacement magnitude. This behavior stems from the fact that the nonlinearity is inherited from the capacitance and gap nonlinear relation. At a  $45^\circ$  angle of

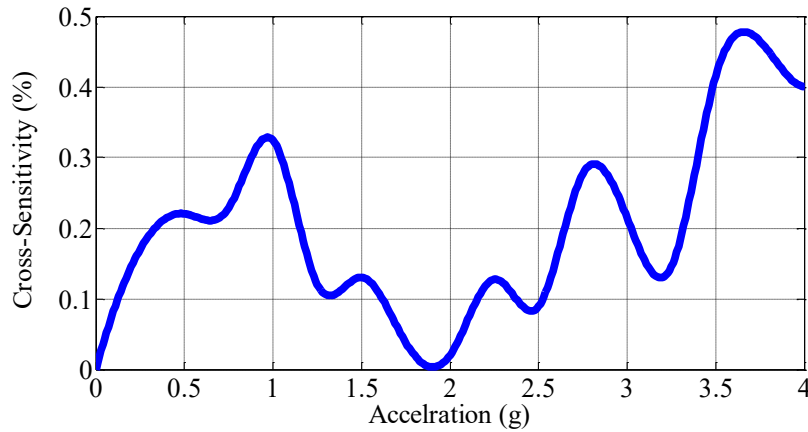


Figure 4.9: Simulated XY cross-sensitivity vs. acceleration at  $0^\circ$ .

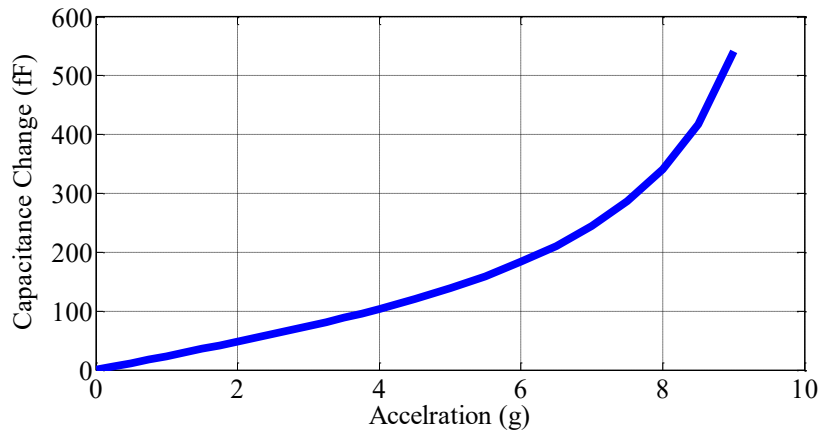


Figure 4.10: Simulated capacitance vs. acceleration at  $0^\circ$  acceleration.

acceleration, the acceleration force is exerted on four proof masses instead of only two when at a  $0^\circ$  angle. This results in a smaller gap change when at a  $45^\circ$  angle, and hence the device exhibits better linearity. The maximum alignment error is  $1.6^\circ$  at a  $22.5^\circ$  acceleration angle. If mismatches caused by fabrication conditions were (and could be) taken into consideration, the simulation results would have yielded better results.

The relationship between the input acceleration at  $0^\circ$  and the resulting differential capacitance is shown in Figure 4.10. Within the expected operating input acceleration range of 4 g, the device exhibits good linearity, because the gap change remains considerably small compared to the nominal gap. The linearity decreases beyond that range, as the capacitive gap becomes smaller due to higher displacement, because the capacitance change is inversely proportional to the capacitive gap. Notably, the nonlinearity is relatively low (i.e., a 3.7% maximum variation from a linear fit over the target input range of 4 g), and it starts to increase significantly at input accelerations larger than 6 g. Note that the capacitance changes at different angles have even better linearity, because off-axis accelerations result in smaller proof mass displacements.

Figure 4.11 shows the simulated displacements of the proof masses for different acceleration angles. The fixed or non-moving parts are shown in blue, and the parts with maximum displacement are red colored. It can be seen that the resulting deflection angle makes the displacement unequal at different points on the moving electrodes. The mechanical decoupling can be seen in Figure 4.11 (a) when the acceleration is at  $0^\circ$ . As

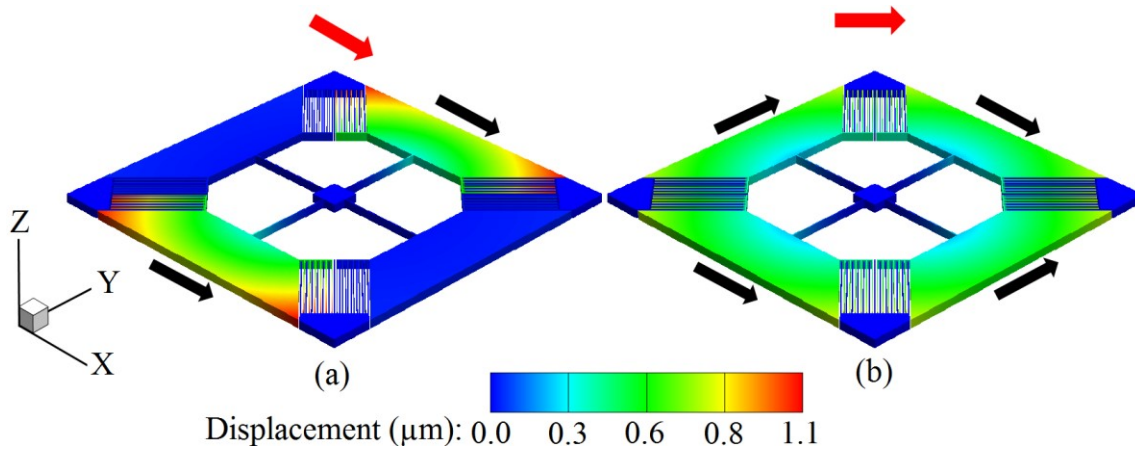


Figure 4.11: Displacement with a 4-g acceleration at (a)  $0^\circ$  and (b)  $45^\circ$ .

can be seen, the two proof masses in blue do not move, because their degrees of freedom are perpendicular to the direction of the acceleration. Figure 4.11 (b) shows the expected equal displacement of all proof masses when they experience acceleration at a  $45^\circ$  angle.

#### 4.4.2 The Test Setup and Digital Interface Integration

Figure 4.12 shows a block diagram of the dual-axis accelerometer SiP under investigation. The capacitance of each accelerometer axis is read by a CDC that sends the readings through an I<sup>2</sup>C interface to a digital multiplexer. The multiplexer sends both readings alternately to a microcontroller that is used to control the overall system. The microcontroller sends all the readings to the human interface device (HID), which can be a computer or a display.

The rotary motion simulator can provide angular velocity, which is used to simulate centripetal acceleration in the axis perpendicular to the rotation axis as [18]:

$$a = r\omega^2, \quad (4.10)$$

where  $r$  is the rotation radius and  $\omega$  is the angular velocity.

The accelerometer is wire-bonded to two CDCs in one leadless chip carried (LCC) package (Figure 4.13). Note that the die where the accelerometer is located includes other test structures not related to this work. The two CDCs sequentially communicate with the computer through a communication channel on the rotating stage to provide digital real-time readings of the accelerometer capacitance change in response to motion in both axes.

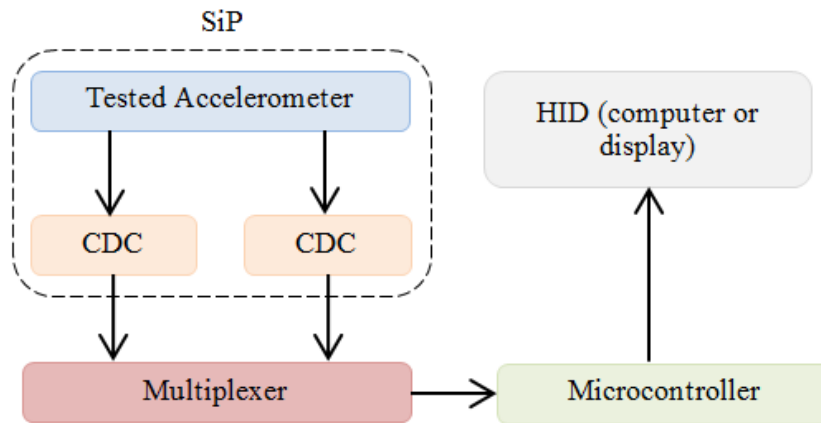


Figure 4.12: System block diagram.

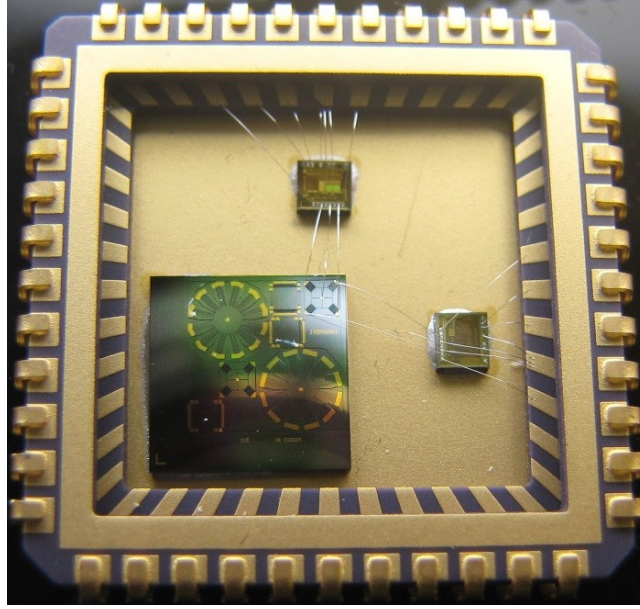


Figure 4.13: Accelerometer (bottom left die) and its two CDCs bonded inside the package.

The package including the CDCs and accelerometer is placed into a socket that lies within a protected chamber on the motion simulator to isolate the system while rotating.

Because the two CDCs send the excitation signal to the shared pad connected to all proof masses, they are controlled to prevent cross-talk. Whenever one of them is powered on, the other is turned off and vice versa. A short period of off-state is forced on both of them before and after their on-state to allow the excitation signal to fade away before the other CDC starts (Figure 4.14).

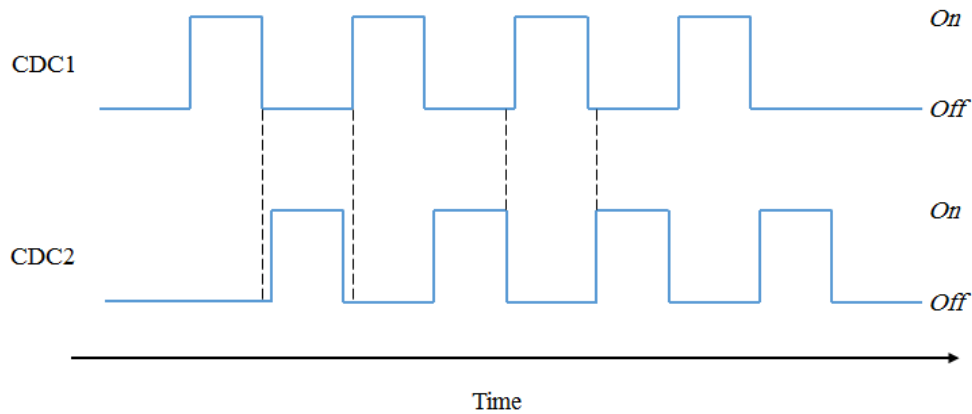


Figure 4.14: Time domain of the two CDC sensing intervals.

#### 4.4.3 Test Results

Figure 4.15 shows the measured output of one axis of the accelerometer, in digital counts from the CDC, and its equivalent capacitance change at different accelerations. The digital count is proportional to the capacitance change of the device, as measured by the CDC. Note that the output of the CDC changes by approximately 6 counts per fF capacitance change. The readings of the CDC were taken for accelerations ranging between 0 g and 7 g with 0.5 g increments. The measured equivalent sensitivity is lower than the simulated sensitivity, and the linearity of the device is somewhat reduced from that seen in simulation. This could be due to some fabrication process variations (e.g., gap size, beam dimensions) or to slightly different structural material properties of the fabricated devices compared to those used in simulations. Similar to the simulation results, the output is linear within the targeted range and, as predicted, the linearity starts to decrease significantly as the acceleration increases beyond 4 g.

The cross-sensitivity from 0 g to 7 g is shown in Figure 4.16. The cross-sensitivity values for the range between 0 g and 2 g are less than the minimum detectable signal by

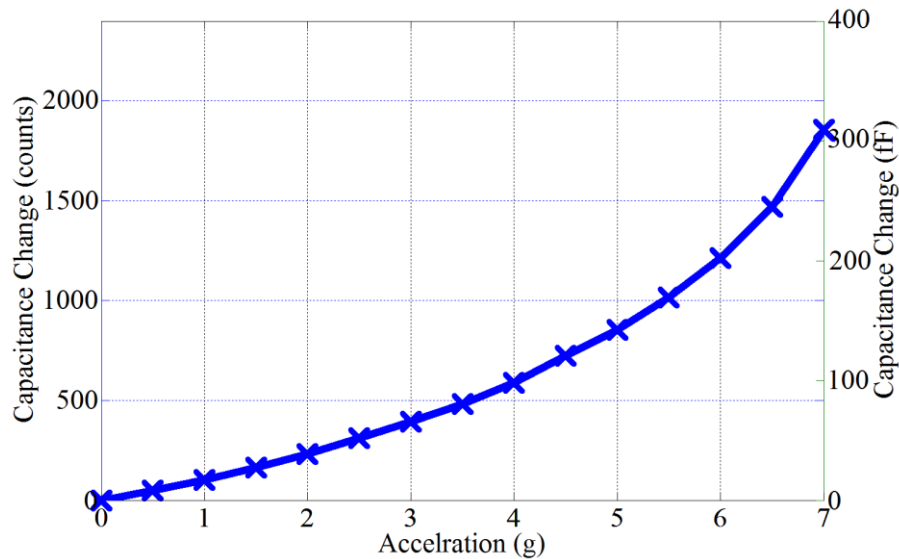


Figure 4.15: Measured CDC digital count change and its equivalent capacitance change versus acceleration.



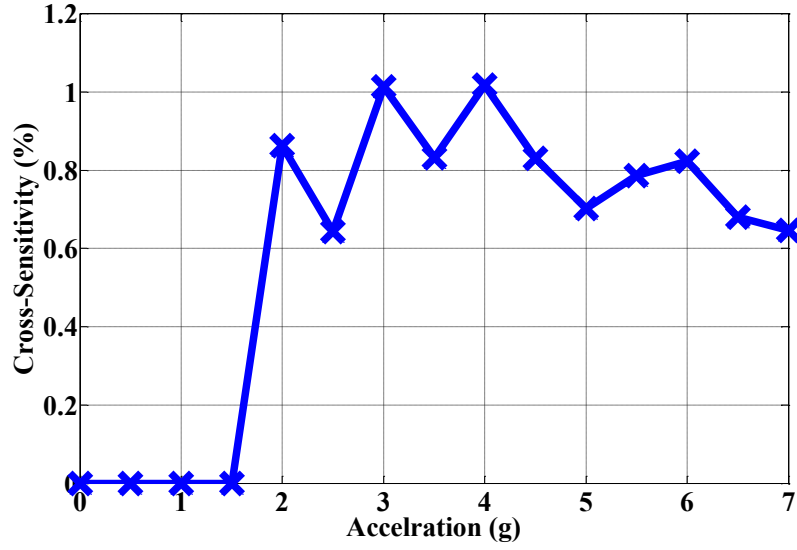


Figure 4.16: Measured cross-sensitivity versus acceleration.

the electronic CDC. The measured cross-sensitivity for the range from 2 g to 7 g is about twice as large as the one predicted in the simulation. The difference between the simulated and measured cross-sensitivities is attributed to mass and beam spring constant mismatches between the four accelerometer proof masses in the fabricated device, which were not accounted for during simulation. It should also be noted that the cross-sensitivity tends to decrease as the acceleration increases because the resulting capacitance in the acceleration axis increases nonlinearly. Nonetheless, the device cross-sensitivity remains lower than that of other reported multi-axis accelerometers, e.g. in [8, 10].

#### 4.5 Discussion

Table 4.3 summarizes the simulated and measured performance of the accelerometer introduced here, and compares it to other published devices. As can be seen, there is always a clear tradeoff between the number of axes and the minimum cross-sensitivity that can be achieved. Moreover, there is a tradeoff between the (g) range acceleration and the sensitivity. While the sensitivity of the structure proposed here is relatively lower than that of single-axis accelerometers, it is comparable to that of multi-axis devices [7, 8, 10]. The structure also exhibits a lower cross-sensitivity compared to that of other multi-axis devices. Note that reducing the widths of the beams to the technology's minimum (i.e. 2  $\mu\text{m}$ ) can increase the structure's sensitivity more than four



times (i.e.  $\sim 110$  fF/g vs.  $\sim 25$  fF/g), but this may result in alignment errors that can exceed  $10^\circ$ , depending on the acceleration and its angle. The linear range of the device could also be improved by increasing the beam width, but this would sacrifice sensitivity. Even though the targeted sensitivity per unit area was not achieved, the resulting value is still acceptable.

The sensitivity was measured using the CDC output in counts/g. It should be noted that the CDC's resolution was not sufficient to measure accelerations below 10 mg. Accordingly, the cross-sensitivity output was difficult to measure for accelerations below 2 g. Even though the proof mass shows a rotational displacement in its operation, this motion was shown in simulations to have an insignificant influence on the performance of the accelerometer. At constant rotational velocity, the proof masses will endure centripetal forces that will displace them away from the center of rotation of the device, but only at very high speeds (i.e. on the order of  $10^7$  °/s). Similarly, due to the relatively small beam lengths, significant capacitance changes on all axes appear only at very high constant rotational accelerations that can sufficiently bend the beams (i.e. on the order of  $10^5$  °/s<sup>2</sup>).

The structure is relatively robust to proof mass mismatches, as a simulated 2- $\mu$ m length mismatch in the proof masses resulted only in a 1.3% difference in the differential capacitance. The fabricated device had the same output in both axes, which means that the fabrication tolerance did not have much effect. However, mismatches may deteriorate the cross-sensitivity of the device, as shown in the measurement results. Leaving some of the bottom substrate material connected to the proof masses increases the sensitivity, but the

Table 4.3: Results comparison.

Parameter	This work				
	[7]	[8]	[10]	Simulated	Measured
Sensing axes	1	2	3	2	2
Device thickness ( $\mu$ m)	120	15	50	25	25
Range (g)	1	6	3.2	4	4
Sensitivity (fF/g)	150	30	7	25	16.83
Cross-sensitivity (%)	0.26	2.5	2.38	0.48	1.02
Minimum detectable signal (mg)	0.1	-	-	-	10
Sensor size (mm <sup>2</sup> )	6.6	-	1.5	1	1
Sensitivity per area (fF/mm <sup>2</sup> )	22.7	-	4.7	25	16.83

structure becomes much more sensitive to accelerations in the Z-axis, and the beams may touch down onto the substrate or even break much more easily.

Because of their high aspect ratios, the central beams are very stiff in the Z-axis. As such, the maximum deflection at the beam tip due to accelerations in the Z-axis is  $\sim 0.25$   $\mu\text{m}$  at 100 g, while the deflection limit is dictated by the tip touching down on the substrate, allowing for a maximum displacement of 2  $\mu\text{m}$ . This Z-axis robustness reduces the cross-sensitivity to that axis. In addition, under Z-axis accelerations, the capacitance change will be reduced by the same amount in all electrodes, which means that the accelerometer is unaffected by Z-axis accelerations. The maximum Mises stress in the structure at 100 g in the Z direction is about 30 MPa, which is much smaller than the 7 GPa yield strength of silicon [19]. This ensures safe device operation, even under large Z-axis accelerations. At high accelerations or shocks in the X- or Y-axis, each fixed electrode will also function as a shock-stop. The maximum Mises stress is less than 10 MPa when the proof mass is stopped by the fixed electrodes, and the device is thus expected to recover from such extreme accelerations.

#### 4.6 Conclusion

This chapter has reviewed a dual-axis capacitive accelerometer design, fabrication, and testing. While the performance of the device is reasonable, its sensitivity per area can still be improved, especially with the empty non-used area between the proof masses and their anchor. Nevertheless, the performance would degrade noticeably since the proof mass would decrease and the sensing axis stiffness would increase if the design was ported to the in-house 3D surface micromachined process described in [20, 21]. Based on several designs, edits, and simulations, it was found that the above design could be edited to integrate the out-of-plane into the sensed axes with acceptable results. However, the idea was abandoned because it would make the fabrication process more complicated. Instead, the focus is on multiple smaller-size and single-axis devices in a simple 3D process. This will make it possible to build the same number of sensing axes in the same area

## 4.7 References

- [1] C. J. Fisher, "Using an accelerometer for inclination sensing," *AN-1057, Application note, Analog Devices*, 2010.
- [2] P. Aggarwal, *MEMS-based integrated navigation*. Artech House, 2010.
- [3] D. Jurman, M. Jankovec, R. Kamnik, and M. Topič, "Calibration and data fusion solution for the miniature attitude and heading reference system," *Sensors and Actuators A: Physical*, vol. 138, no. 2, pp. 411-420, 2007.
- [4] H. Lau and K. Tong, "The reliability of using accelerometer and gyroscope for gait event identification on persons with dropped foot," *Gait & posture*, vol. 27, no. 2, pp. 248-257, 2008.
- [5] J. Chae, H. Kulah, and K. Najafi, "A monolithic three-axis micro-g micromachined silicon capacitive accelerometer," *Journal of Microelectromechanical systems*, vol. 14, no. 2, pp. 235-242, 2005.
- [6] D. Lapadatu, S. Habibi, B. Reppen, G. Salomonsen, and T. Kvisteroy, "Dual-axes capacitive inclinometer/low-g accelerometer for automotive applications," in *Micro Electro Mechanical Systems, 2001. MEMS 2001. The 14th IEEE International Conference on*, 2001, pp. 34-37: IEEE.
- [7] J. Chae, H. Kulah, and K. Najafi, "A CMOS-compatible high aspect ratio silicon-on-glass in-plane micro-accelerometer," *Journal of Micromechanics and Microengineering*, vol. 15, no. 2, p. 336, 2004.
- [8] M. Ferraresi and S. Pozzi, "MEMS sensors for non-safety automotive applications," in *Advanced Microsystems for Automotive Applications 2009*: Springer, 2009, pp. 355-367.
- [9] Y.-W. Hsu, J.-Y. Chen, H.-T. Chien, S. Chen, S.-T. Lin, and L.-P. Liao, "New capacitive low-g triaxial accelerometer with low cross-axis sensitivity," *Journal of Micromechanics and Microengineering*, vol. 20, no. 5, p. 055019, 2010.
- [10] H. Qu, D. Fang, and H. Xie, "A monolithic CMOS-MEMS 3-axis accelerometer with a low-noise, low-power dual-chopper amplifier," *IEEE Sensors Journal*, vol. 8, no. 9, pp. 1511-1518, 2008.
- [11] A. Cowen, G. Hames, D. Monk, S. Wilcenski, and B. Hardy, "SOIMUMPs design handbook," *MEMSCAP Inc*, pp. 2002-2011, 2011.
- [12] N. Yazdi, F. Ayazi, and K. Najafi, "Micromachined inertial sensors," *Proceedings of the IEEE*, vol. 86, no. 8, pp. 1640-1659, 1998.
- [13] S. Godha and M. Cannon, "Integration of DGPS with a low cost MEMS-based inertial measurement unit (IMU) for land vehicle navigation application," in *Proceedings of the 18th International Technical Meeting of the Satellite Division of the Institute of Navigation (ION GNSS05)*, 2005, pp. 333-345.
- [14] W. C. Young and R. G. Budynas, *Roark's formulas for stress and strain*. McGraw-Hill New York, 2002.
- [15] T.-R. Hsu, *MEMS and microsystems: design, manufacture, and nanoscale engineering*. John Wiley & Sons, 2008.
- [16] M. I. Younis, *MEMS linear and nonlinear statics and dynamics*. Springer Science & Business Media, 2011.
- [17] M. Elsayed, F. Nabki, and M. El-Gamal, "A 2000/s dynamic range bulk mode dodecagon gyro for a commercial SOI technology," in *Electronics, Circuits and*

- Systems (ICECS), 2011 18th IEEE International Conference on*, 2011, pp. 264-267: IEEE.
- [18] R. Serway and J. Jewett, *Physics for scientists and engineers with modern physics*. Nelson Education, 2013.
  - [19] K. E. Petersen, "Silicon as a mechanical material," *Proceedings of the IEEE*, vol. 70, no. 5, pp. 420-457, 1982.
  - [20] P.-V. Cicek, "Platforms and techniques for integration of microsystems above integrated electronic circuits," Ph.D. dissertation, Dept. of Elec. and Comp. Eng., McGill University, 2016.
  - [21] M. Elsayed, "Novel architectures for MEMS inertial sensors and resonators targeting above-IC integration," Ph.D. dissertation, Dept. of Elec. and Comp. Eng., McGill University, 2016.

---

# Chapter 5

## In-Plane Capacitive Accelerometer in a 3D Surface Micromachining Process

---

### 5.1 Introduction

Most of the commercial in-plane accelerometers available in the market today use 2D designs. They can be fabricated easily and provide robust performance for most applications. Still, one of the drawbacks of the conventional comb fingers capacitive accelerometers is the tradeoff between the capacitive area and the proof mass. This tradeoff limits the sensitivity and reduces the full employment of the accelerometer area. Even though there is a method to find the optimum value that results in the best sensitivity [1], the optimization does not bring significant improvement. That is due to the nature of the conventional 2D design, which does not allow for features to overlap. Furthermore, the capacitive gap feature size is restricted by the resolution of the mask printing step and the fabrication process. Concerning the surface micromachining, the limited layer thickness results in high stiffness in the lateral motion for the already small proof mass. Moreover, the structural layer material needs to be conductive, which limits the available options. The combination of these factors confines the building of capacitive accelerometers using surface micromachining in commercial products.

In 3D MEMS designs, two or more different layers are used to create complicated overlapping structures. Although they have a complex fabrication process, these designs enable the building of structures that would be impossible to build using 2D designs and fabrication processes. Using a 3D capacitive accelerometer design eliminates most of the 2D design limitations above, and even introduces more advantages. Besides fabrication complexity, these benefits come at the expense of the necessary precautions regarding the complicated design, e.g. avoiding possible short circuits in bending overlapping structures. The 3D designs are less common in building capacitive accelerometers due to fabrication

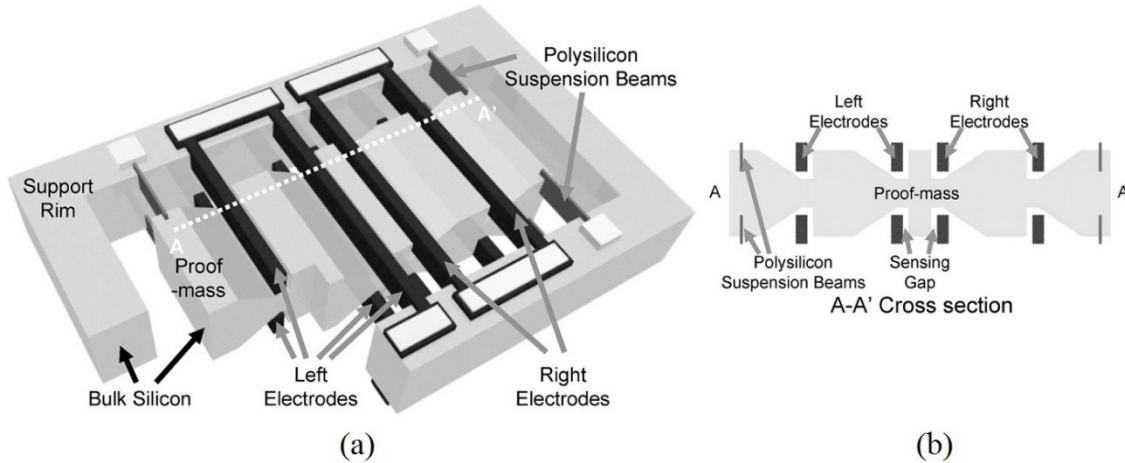


Figure 5.1: An in-plane capacitive accelerometer using a 3D process (a) isometric, and (b) cross-section view [4].

complexity and the available well-established models for the 2D designs. In 2003, Chae et al. introduced a bulk micromachined 3D in-plane capacitive accelerometer [2-4]. They used a six-mask double-sided process to fabricate a device with low noise density and high sensitivity (Figure 5.1). Tsai et al. used post-processing of the CMOS process to create a 3D out-of-plane capacitive accelerometer with low performance [5]. They then used the same post-process to create a three-axis accelerometer on the same chip with better performance in the lateral axes.

This chapter presents a novel design of an in-plane surface micromachined differential capacitive accelerometer. It is fabricated in a simple CMOS-compatible process to enable above-IC monolithic integration of a high-sensitivity capacitive accelerometer for fan-out packaging applications. The design is a 3D capacitive accelerometer that uses the whole area for both the proof mass and sensing electrodes simultaneously, thereby eliminating the mass and sensing area tradeoff. In this design, the fixed electrodes are built on a platform made of a non-conducting material that uses the entire design space width. After reviewing the working principle of the accelerometer, the chapter derives and explains its design model and novel design ideas. Then, the targeted specifications for motion tracking applications are set. After that, the testing results of the fabricated accelerometer are discussed, followed by a section detailing how the design can be improved. Finally, the chapter concludes with a summary of the design.

## 5.2 Accelerometer Design Model

Figure 5.2 shows top and isometric views of the accelerometer design. The design uses non-conductive material to create the structural layers, referred to a “platforms” here. On the sides of these platforms, two metal layers are built to form the bottom fixed electrodes, which are also extended on the platforms and in the trenches (Figure 5.2 (a)). The proof mass is a layer that covers most of the device area and is anchored at two opposite sides. It is placed on the top of the platforms and trenches and serves as a moving electrode, creating two differential capacitors with the bottom electrodes (Figure 5.2 (b)). Between the bottom electrodes and the top electrode, a capacitive gap is formed using a sacrificial layer. After etching that layer, the proof mass is released and it can move freely when input acceleration is present.

Assume that the accelerometer dimensions have lengths in the X-axis and widths in the Y-axis when looking at a top view. A cross-section of the accelerometer featuring the design parameters is shown in Figure 5.3. The proof mass, the platforms, and the trenches have the same length  $L$ . The platforms’ height (layer thickness) is given by  $h_p$  and their width

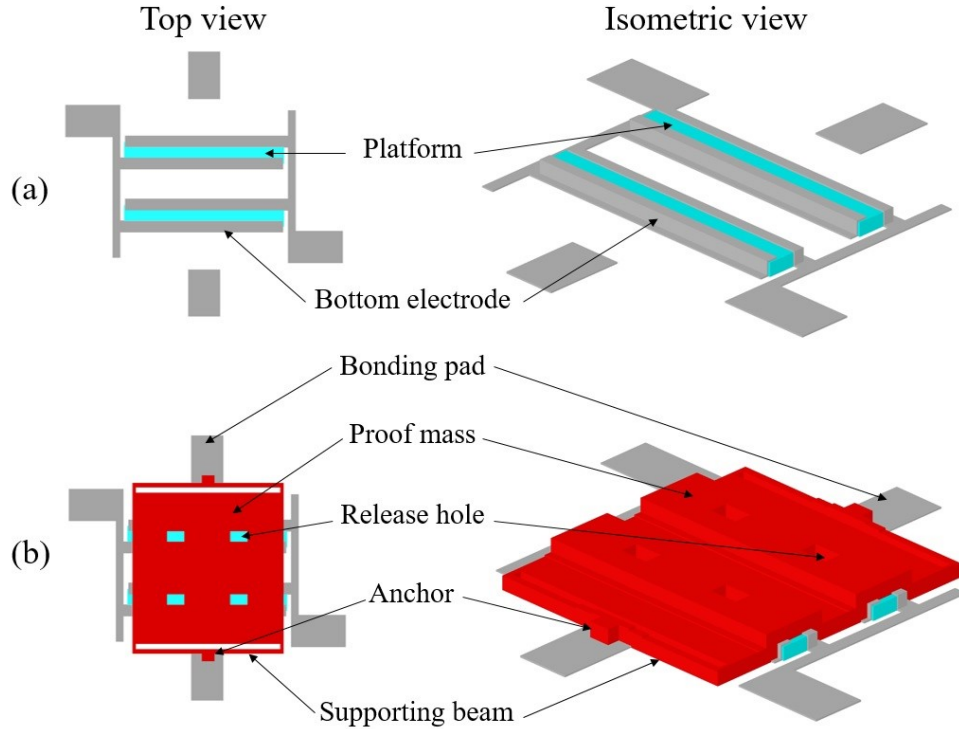


Figure 5.2: Top and isometric views of (a) platforms and bottom electrodes, and (b) final structure.

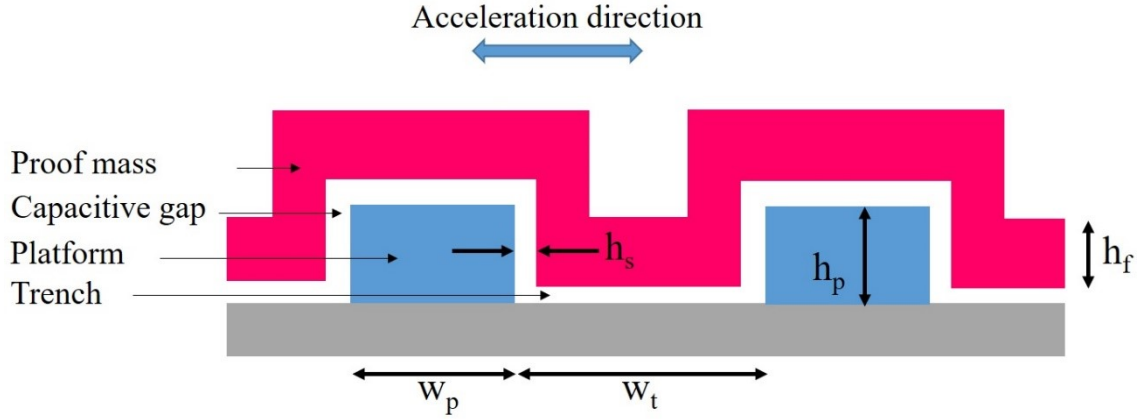


Figure 5.3: A cross-section view showing the accelerometer design parameters.

by  $w_p$ . The area between platforms is considered a trench width and is defined as  $w_t$ . The thickness of the proof mass layer and the sacrificial layer is  $h_f$  and  $h_s$ , respectively. The following subsections provide a detailed review of the design model to explain how each parameter affects the performance of the accelerometer. These subsections also describe how simulations were used to justify some design decisions.

### 5.2.1 Capacitances

The two bottom electrodes and the top electrode were designed to form two differential capacitances in the lateral direction. Due to the shape of the electrodes on the platform, each of them creates one horizontal and two vertical capacitors. The six capacitances on the two differential electrodes are shown in Figure 5.4. Regardless of the

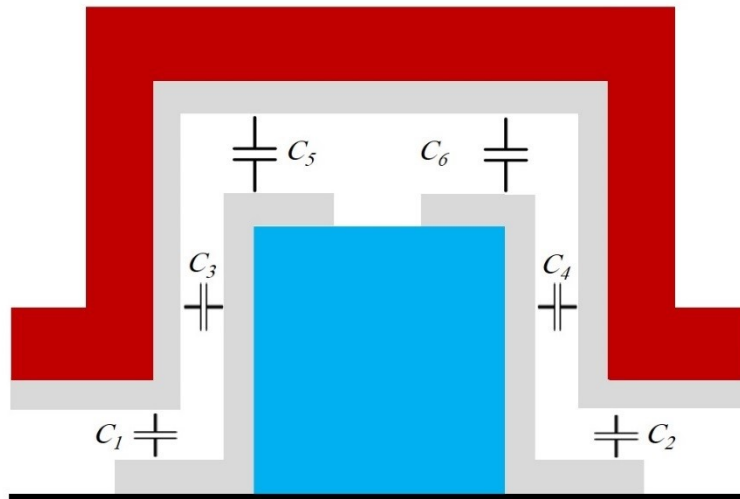


Figure 5.4: Capacitors formed by two differential electrodes.



electrodes and platform misalignments, the vertical capacitances always have the same value – that is:

$$C_1 + C_5 = C_2 + C_6, \quad (5.1)$$

which makes them cancel out when the differential capacitance between the two electrodes is measured. While the vertical cross-input changes these capacitance values, the ratio between the capacitance difference of the two sets does not change. The capacitance change,  $\Delta C$ , due to an  $x$  lateral displacement of the proof mass is given by:

$$\Delta C = C_3 - C_4 = \epsilon h_p L \frac{2x}{d^2 - x^2}. \quad (5.2)$$

### 5.2.2 Proof Mass and Sensitivity

Assuming the whole accelerometer area is utilized by platforms, the proof mass,  $m$ , for an accelerometer with length  $L$  and  $N_p$  number of platforms, is given by:

$$m = \rho L h_f \left( (N_p + 1) (w_t - 2(h_f + h_s)) + N_p (w_p + 2h_s) + 2N_p (h_p + h_f) - N_h A_h \right), \quad (5.3)$$

where  $\rho$  is the proof mass film density,  $N_h$  is the number of release holes, and  $A_h$  is the size of each release hole. Using the same layer thickness and size, the 3D design has **up to four times** more mass than the 2D design, which leads to larger deflection and hence better sensitivity. The accelerometer capacitive sensitivity per input acceleration,  $S$ , can be expressed as:

$$S = \frac{2\epsilon N_p L (h_p - h_s)}{h_s^2} \frac{ma}{k}, \quad (5.4)$$

where  $h_s$  is the capacitive gap,  $k$  is the total spring constant of the supporting beams, and  $a$  is the acceleration. To obtain the sensitivity in  $[F/g]$  unit, an approximate gravitational acceleration value of  $9.81 [m/s^2]$  can be used for  $a$ . Some of these parameters are correlated because they use the same value in their expressions, e.g.  $m$  and  $k$ , which raises the need for optimal and realistic design values.

To explore the improvement that can be achieved by using this 3D design, its sensitivity is compared to that of a conventional 2D design with similar design parameters. When both have the same size, spring constant, number of platforms or comb fingers, gap, and proof mass thickness, the sensitivity ratio is:

$$\frac{S_{3D}}{S_{2D}} = \frac{l_{3D}}{l_{2D}} \frac{m_{3D}}{m_{2D}}, \quad (5.5)$$

which can achieve *a minimum improvement of six times*, depending on the 2D design parameters. This comparison imposes the 2D design parameter limitations on the 3D design, e.g. the restrictions on the finger length-to-width ratio faced in the 2D designs. This ratio can be increased when the flexibility in the 3D design is exploited, e.g. by increasing the platforms' thicknesses and reducing their widths and spacings.

### 5.2.3 Enhanced 3D Suspension Beam

Surface micromachining processes offer many advantages, but this is at the price of easier bending in the z-axis, since the layer thicknesses are usually small. This issue worsens when the vertical gap is very small, which is the case in the 3D fabrication process. This requires the structural layer to be made thicker to increase the vertical stiffness, or the vertical gap to be increased, which degrades the performance of the device built using the 3D process. Therefore, the platforms technique is used here to enhance the vertical stiffness and prevent such problems. In addition, the lateral stiffness might also be reduced, which improves the performance at no cost, based on the layout.

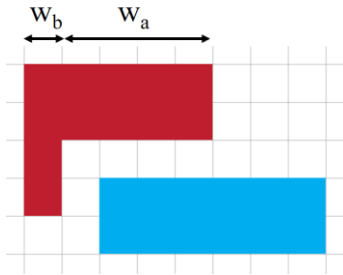
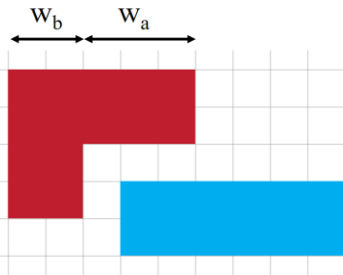
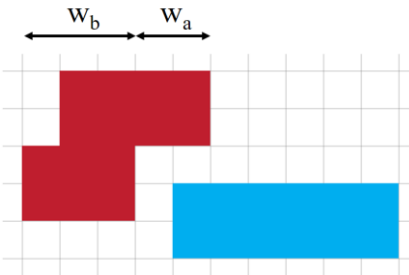
By placing part of the supporting beam on the platform, the cross-section can be either Z- or L-shaped depending on the beam platform overlap dimensions and the layer thickness. Assume a supporting beam with layer thickness  $h_f$  and width  $w_s$  that consists of two parts:  $w_a$  on top of the platform and  $w_b$  in the trench. Table 5.1 shows different scenarios when using a beam with the same width,  $w_s$ , where the red shape is the beam cross-section, the blue shape is the platform, and the space between them is the gap left after removing the sacrificial layer. A grid of squares was drawn to show the parameters' dimensions, where  $w_s$  is 5 units and  $h_f$  is 2 units. When  $h_f$  is equal to or larger than  $w_b$ , the cross-section becomes L-shaped; otherwise, the cross-section is Z-shaped. However, when  $h_f$  is larger than  $w_b$ , one of the L arms has a smaller width, which has an impact on the beam

stiffness. Intuitively, the Z-shaped cross-section can be transformed into an L-shaped one by decreasing the layer thickness and vice versa.

These shapes are not common in MEMS development, since rectangular cross-section beams are usually used. Thus, their corresponding stiffness in the vertical and lateral directions is derived below. For a proof mass suspended from opposite sides, each supporting beam has two boundary conditions:

1. The anchored side has no linear displacement nor angular displacement, and
2. The side attached to the proof mass has  $x$  linear displacement and no angular displacement.

Table 5.1: Supporting beam cross-section depending on the layout and thickness parameters.

Condition	Beam cross-section
$h_f > w_b$	
$h_f = w_b$	
$h_f < w_b$	

Thus, the supporting beam is of the clamped-guided type and the spring constant,  $k$ , for each beam is given by the Euler–Bernoulli beam theory [6, 7]:

$$k = \frac{12EI}{l^3}, \quad (5.6)$$

where  $E$  is Young’s modulus,  $I$  is the cross-section moment of inertia, and  $l$  is the beam length. Using the parallel axis theorem, the moment of inertia for a cross-section composed of multiple segments is given by [8, 9]:

$$I = \sum (\bar{I}_i + A_i d_i^2), \quad (5.7)$$

where  $\bar{I}$  is the moment of inertia of a segment,  $A$  is its area, and  $d$  is the distance between the segment center and the neutral axis of the shape centroid,  $C$ . For a rectangular segment with width  $a$  and height  $b$ , its moment of inertia,  $I$ , is [9]:

$$I = \frac{ab^3}{12}. \quad (5.8)$$

The distance of the centroid from a reference point also contributes to the moment of inertia and is given by [8]:

$$C = \frac{\sum A_i C_i}{\sum A_i}, \quad (5.9)$$

where  $A_i$  is the segment area and  $C_i$  is the distance between the segment centroid to the reference point.

#### 5.2.3.1 Derivation of the Moment of Inertia

Figure 5.5 shows the cross-sections of L- and Z-shaped beams. The moment of inertia is calculated by splitting the cross-sections into rectangular sections that have the known moment of inertia in (5.8). To obtain the minimum number of rectangular segments, the shape is broken into two segments using a vertical line. Using a horizontal line is also feasible, but the vertical line is used here to maintain consistency as the Z-shaped cross-section must be split using vertical lines (Figure 5.5 (b)). The Z-shaped cross-section is split into three segments vertically to keep the model valid when  $h_f$  is larger than  $h_p$ .

Assuming each segment has height  $h$  and width  $w$ , the cross-section centroid coordinates are given by:

$$C_x = \frac{h_1 w_1 \frac{w_1}{2} + h_2 w_2 \left( w_1 + \frac{w_2}{2} \right) + h_3 w_3 \left( w_1 + w_2 + \frac{w_3}{2} \right)}{h_1 w_1 + h_2 w_2 + h_3 w_3}, \text{ and} \quad (5.10)$$

$$C_y = \frac{h_1 w_1 \frac{h_1}{2} + h_2 w_2 \frac{h_2}{2} + h_3 w_3 \left( h_2 - \frac{h_3}{2} \right)}{h_1 w_1 + h_2 w_2 + h_3 w_3}.$$

Therefore, the supporting beam moments of inertia around the X-axis and the Y-axis in (5.7) become:

$$I_X = \frac{w_1 h_1^3}{12} + \frac{w_2 h_2^3}{12} + \frac{w_3 h_3^3}{12} + h_1 w_1 \left( C_y - \frac{h_1}{2} \right)^2 + h_2 w_2 \left( C_y - \frac{h_2}{2} \right)^2$$

$$+ h_3 w_3 \left( C_y - h_2 + \frac{h_3}{2} \right)^2, \text{ and}$$

$$I_Y = \frac{h_1 w_1^3}{12} + \frac{h_2 w_2^3}{12} + \frac{h_3 w_3^3}{12} + h_1 w_1 \left( C_x - \frac{w_1}{2} \right)^2 \quad (5.11)$$

$$+ h_2 w_2 \left( C_x - w_1 - \frac{w_2}{2} \right)^2$$

$$+ h_3 w_3 \left( C_x - w_1 - w_2 - \frac{w_3}{2} \right)^2.$$

By substituting the process and layout parameters into (5.6) and (5.8), the spring constant for vertical and lateral axes is obtained. To express the parameters in (5.10) and (5.11) in terms of the process and layout parameters, the following is used:

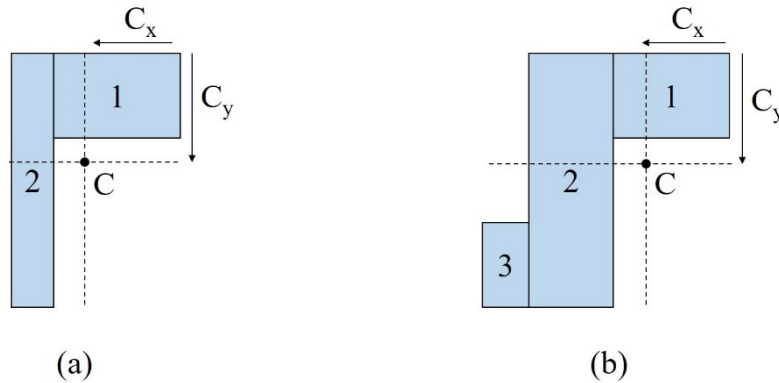


Figure 5.5: Cross-section of (a) L-shaped, and (b) Z-shaped beams.

$$\begin{aligned}
h_1 &= h_f, \\
w_1 &= w_a + h_s, \\
h_2 &= h_p + h_f, \\
w_2 &= \begin{cases} w_b - h_s, & w_b + h_s \leq h_f \\ h_f, & w_b + h_s > h_f \end{cases} \\
h_3 &= h_f, \text{ and} \\
w_3 &= w_b - h_f - h_s.
\end{aligned} \tag{5.12}$$

### 5.2.3.2 Spring Constant Simulations

To verify the effectiveness of this design, equal amounts of force were applied to four beams of 100  $\mu\text{m}$  length, 2  $\mu\text{m}$  film thickness, and 5  $\mu\text{m}$  width, with the platform having 2  $\mu\text{m}$  thickness. The cross-sections of the beams are flat rectangular-shaped: L-shaped with  $w_b < h_f$ , L-shaped with  $w_b = h_f$ , and Z-shaped where  $w_b > h_f$ , respectively. The verification was done both analytically and using finite elements simulation as shown in Table 5.2 and Figure 5.6. As depicted, using platforms to enhance the vertical stiffness decreased the vertical deflection at different percentages depending on the used cross-section down to 24% (from 3.12  $\mu\text{m}$  to 0.59  $\mu\text{m}$ ), which helped to increase the allowed input range in the vertical axis. Moreover, the Z-shaped cross-section yielded lower stiffness and hence better sensitivity in the lateral sensing axis. This improvement resulted from the fact that the sum of cubes was smaller than the cube of the sum in the beam

Table 5.2: Analytical and simulation results of applying the same force on beams with different cross-sections.

		Flat	$w_b < h_f$	$w_b = h_f$	$w_b > h_f$
Analytical	Lateral deflection ( $\mu\text{m}$ )	0.50	0.38	0.36	0.42
	Vertical deflection ( $\mu\text{m}$ )	3.13	0.98	0.65	0.59
	Ratio	0.16	0.39	0.56	0.70
Simulation	Lateral deflection ( $\mu\text{m}$ )	0.50	0.44	0.43	0.53
	Vertical deflection ( $\mu\text{m}$ )	3.12	1.15	0.77	0.76
	Ratio	0.16	0.39	0.56	0.70

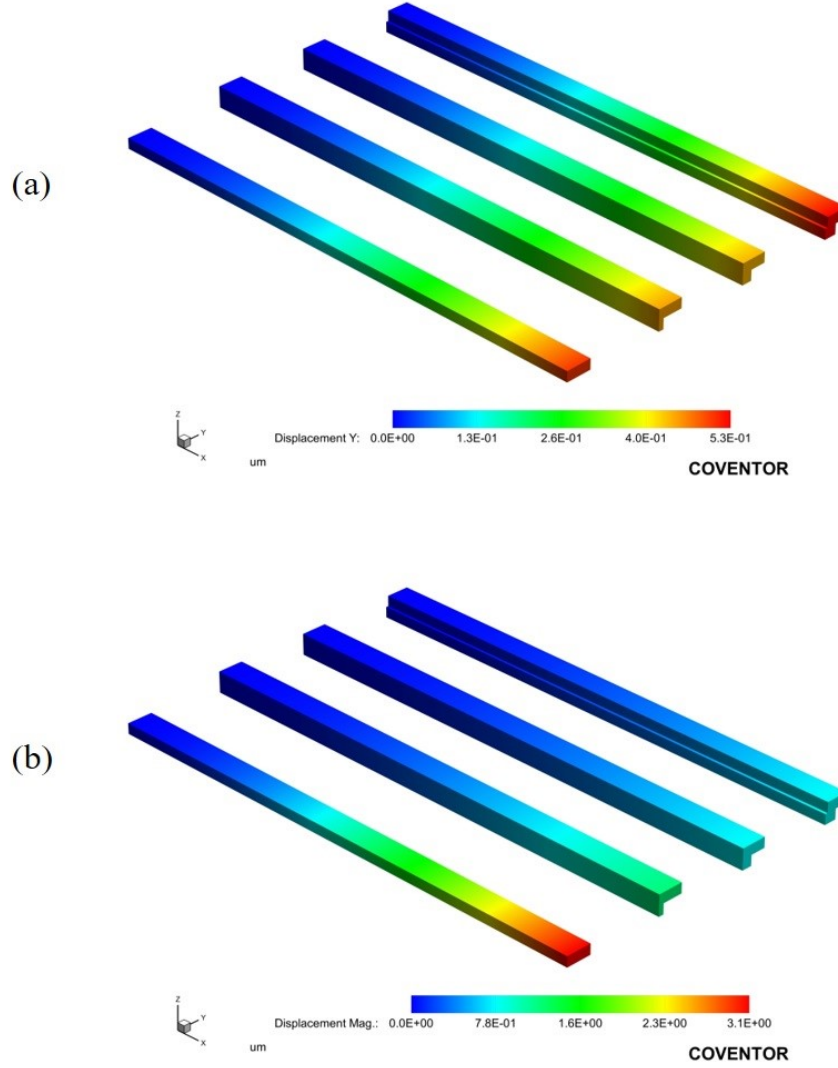


Figure 5.6: Deflection in the four beams' (a) lateral axis, and (b) vertical axis.

moment of inertia, i.e.  $w_a^3 + w_b^3 < (w_a + w_b)^3$ . For all cross-sections, increasing the film thickness or the beam width decreased the stiffness.

Table 5.2 compares the analysis and simulation deflection values of the beams in the lateral and vertical axes. The flat beam results agree with each other to a great extent in terms of both values and ratios. However, there are slight differences between the values in the L- and Z-shaped cross-sections. The error comes from the analytical results and is caused by the Euler–Bernoulli beam theory, which ignores the shear strain [10, 11]. This difference is not substantial in the case of the flat beam because of its symmetrical cross-section. Other theories give slightly more accurate predictions for asymmetric cross-

sections, but they have complex governing equations [12-14]. Nevertheless, the ratios and the value trends attest to the effectiveness of the design concept.

#### 5.2.4 Noise Analysis and Optimum Gap

While it seems intuitive that the capacitive gap should be reduced for better sensitivity, the following demonstrates that there is an optimal gap that should be used to obtain a decent performance. In capacitive MEMS accelerometers, two sources of noise resemble input accelerations and determine the minimum detectable signal (MDS): electrical and mechanical noises. The electrical noise is caused by the readout circuit, and is called circuit noise equivalent acceleration (CNEA). Although it does not introduce physical acceleration in the system, it defines the minimum acceleration that can be sensed using the readout circuit. This noise is given by [15]:

$$CNEA = \frac{\Delta C_{min}}{S}, \quad (5.13)$$

where  $\Delta C_{min}$  is the readout circuit resolution. The mechanical noise is a white noise caused by the thermomechanical motion of air molecules in the small air gaps used to sense the displacement. It is considered to be a damping force and when divided by the mass, it can be converted to acceleration noise, which is known as the BNEA [16]:

$$BNEA = \frac{\sqrt{4k_B T D}}{m}, \quad (5.14)$$

where  $k_B$  is the Boltzmann constant,  $T$  is the temperature, and  $D$  is the damping. The total noise equivalent acceleration (TNEA) can be expressed as:

$$TNEA = \sqrt{CNEA^2 + BNEA^2}. \quad (5.15)$$

Amini et al. developed a method to determine the optimum gap that causes the minimum noise for capacitive accelerometers working at atmospheric pressure [15]. They assumed a fixed effective viscosity of  $18.5 \times 10^{-6}$  for air in their model. This assumption holds for gaps larger than  $2 \mu\text{m}$  because of the small variations in the effective viscosity (Figure 5.7). However, it can be noticed that the effective viscosity decreases rapidly in smaller gaps, as the fluid flow changes from the transitional flow regime ( $0.1 < K_n < 10$ )



to the slip flow regime ( $0.01 < K_n < 0.1$ ) [17]. To obtain a more accurate model, the effective viscosity for small gaps is introduced into the model presented here.

The gas that fills the capacitive gap has a significant impact on the performance of the accelerometer. The mean free path  $\lambda$  is the average distance traveled by a molecule between successive collisions and is estimated to be  $65 \times 10^{-9}$  m for air at atmospheric pressure and room temperature in [18]. The Knudsen number  $K_n$  for a gap is given by [17, 19, 20]:

$$K_n = \frac{\lambda}{d}, \quad (5.16)$$

where  $d$  is the characteristic physical dimension, which in this case is the capacitive gap,  $h_s$ . The viscosity coefficient  $\mu$  of air is given by  $1.8523 \times 10^{-5}$  [21]. The effective viscosity  $\mu_{\text{eff}}$  can be approximated with  $\pm 5$  accuracy using the following equation [18, 22]:

$$\mu_{\text{eff}} = \frac{\mu}{1 + 9.638 K_n^{1.159}}. \quad (5.17)$$

In the in-plane axis, the squeeze film damping between two long strips with length  $l$  and gap  $h$  is approximated as [19]:

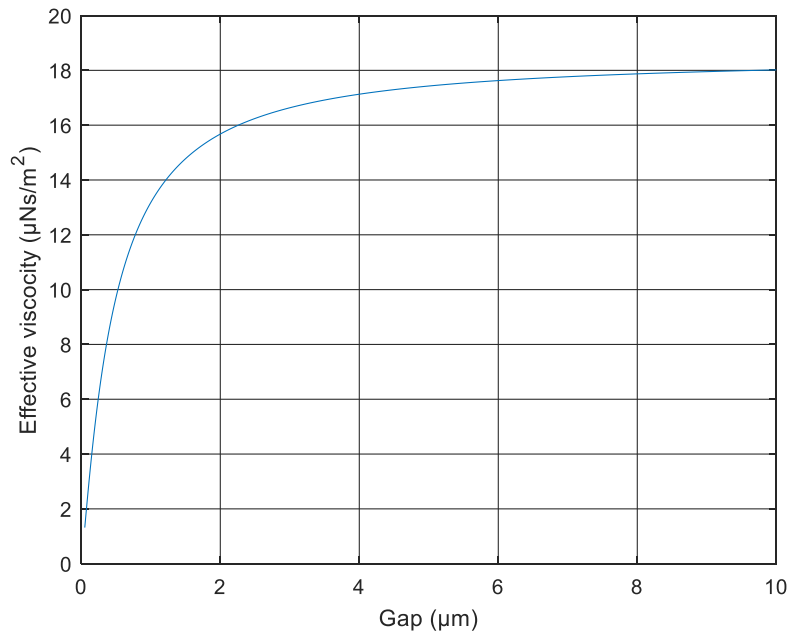


Figure 5.7: Air effective viscosity vs. the capacitive gap.

$$D = \mu_{\text{eff}} l \left( \frac{h}{d} \right)^3, \quad (5.18)$$

For the above capacitive accelerometer design, with  $N_p$  platforms, the damping can be expressed as:

$$D = N_p \mu_{\text{eff}} L \left( \frac{h_p - h_s}{h_s} \right)^3. \quad (5.19)$$

A squeeze film damping force also acts in the out-of-plane axis. This force is affected by the release holes and the cell area for each hole. Bao derived a model for the squeeze damping force in a thin hole-plate [19, 23]. Nevertheless, this force acts in an axis that is perpendicular to the sensing axis and is much smaller than the Brownian noise, so it can safely be neglected.

#### 5.2.5 Bandwidth and Damping Ratio

The accelerometer targeted frequency response or bandwidth is a major determining parameter in the mechanical design. The mechanical resonance frequency determines the upper limit of the frequency response, while its lower limit can reach DC response (0 Hz) for static sensing. The bandwidth can also be reduced by using a low-pass filter to prevent aliasing and enhance the output [24]. For a capacitive accelerometer with a mechanical spring constant  $k$  in the lateral axis and an electrostatic spring constant  $k_e$ , the natural resonance frequency,  $\omega_n$ , is given by [25]:

$$\omega_n = \sqrt{\frac{k + k_e}{m}}. \quad (5.20)$$

where  $k_e$  is a negative constant resulting from the electrostatic force applied in the opposite direction of the input acceleration force. Hence, using closed-loop control by introducing electrostatic force to the sensor reduces the resonance frequency of the mechanical structure. In addition, a larger bandwidth results in a smaller sensitivity, as there is a tradeoff between these two parameters. For an open-loop system,  $k_e$  is 0.

The damping ratio,  $\zeta$ , is a dimensionless measure that determines the speed at which the system stabilizes after a change in the input. The system is overdamped when  $\zeta > 1$ , critically damped when  $\zeta = 1$ , and underdamped when  $0 < \zeta < 1$ . Figure 5.8 shows the

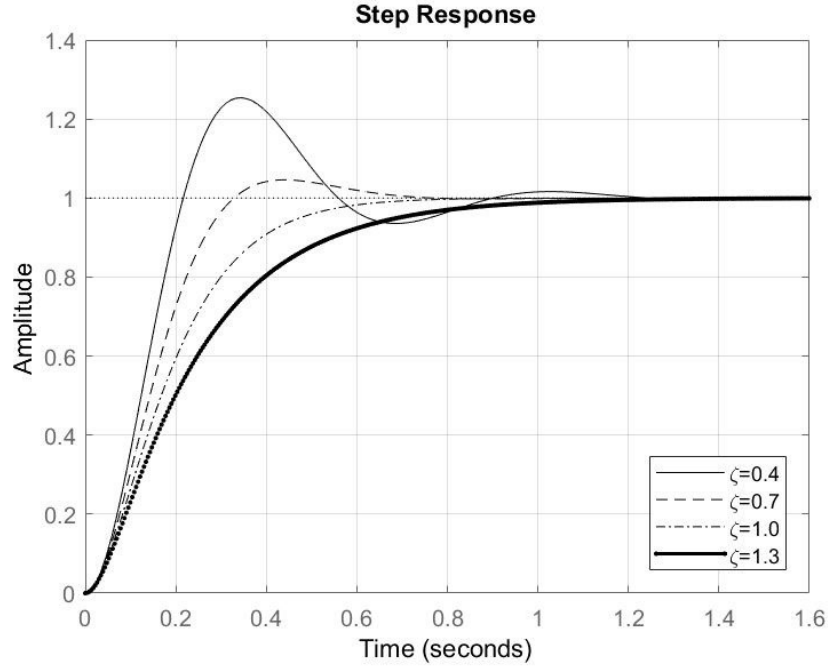


Figure 5.8: Step response for different damping ratios.

damping response for different damping ratios, where a tradeoff exists between the rise time and the settling time. The optimum damping ratio for an accelerometer that gives the largest bandwidth is equal to  $1/\sqrt{2}$  or 0.707 because it converges faster than other values [26-28]. Nevertheless, second-order systems like accelerometers are underdamped systems and have practical damping ratios between 0.6 and 0.8, which gives more room for design parameters [29, 30]. The damping ratio is expressed as [25, 31]:

$$\zeta = \frac{D}{2m\omega_n}. \quad (5.21)$$

For a second-order system, the bandwidth,  $\omega_{BW}$ , equals the system natural frequency when  $\zeta = 1/\sqrt{2}$ . Otherwise, it is given by [32]:

$$\omega_{BW} = \omega_n \sqrt{1 - \zeta^2}. \quad (5.22)$$

## 5.3 Accelerometer Design

### 5.3.1 Target Specifications

In general, the design process starts by determining the required performance for the application. The design proposed here could target a wide range of applications by adjusting its different parameters discussed earlier. To increase its competitive value, the focus here is on applications that represent future challenges for other conventional designs, i.e. fan-out above-CMOS accelerometers. One of these applications is motion tracking, where the accelerometer tracks the tilt or the acceleration of the platform held or worn by the user. This application usually requires moderate performance and miniature chips with small PCB footprints to cut down the needed area.

Researchers regularly report tracking body motion using commercial accelerometers within a set of other sensors [33-36]. For instance, Yun et al. used a 9-axis MARG sensor containing a 3-axis accelerometer to track body motion [37]. They applied Kalman filtering to improve the readings and obtained more than 2% static accuracy and 9% dynamic accuracy. The performance degradation in the dynamic accuracy was caused by the communication delay and not the accelerometer performance. To find the required specs for an accelerometer design that fits many applications, a survey of accelerometers used in final applications nowadays was conducted. Table 5.3 lists performance parameters in top-quality consumer applications released in 2016, for different categories. Firstly, the Fitbit Charge 2 is a wristband activity and exercise tracker. It extrapolates body motion by

Table 5.3: Performance comparison of accelerometers included in different devices.

Parameter	LIS2DH	BMI055	LSM6DSM
Range (g)	$\pm 2$ to $\pm 16$	$\pm 2$ to $\pm 16$	$\pm 2$ to $\pm 16$
Sensitivity at 2 g (mg/LSB)	1	0.977	0.061
Cross-axis sensitivity (%)	-	1	-
Noise density ( $\mu\text{g}/\sqrt{\text{Hz}}$ )	-	150	90
Bandwidth (Hz)	672	230	208
Max update rate (kHz)	5.3	2	6.664
Sensitivity change vs temperature (%/°C)	0.01	0.02	0.01

using an LIS2DH 3-axis accelerometer from STMicroelectronics to sense hand motion [38]. The high-performance mode specs are listed here since it uses that mode when tracking activities. Secondly, the Oculus Rift is a virtual reality headset that features a 6-axis BMI055 accelerometer and gyroscope chip from Bosch Sensortec [39]. Combined with a magnetometer, they provide real-time data to the computer about the user's head orientation, and the accelerometer is mainly used to detect the head tilt in 3D space. The high-performance specs of the accelerometer are listed here too, since the headset runs in that mode all the time, as it is powered by electrical wires instead of batteries. Finally, Apple's flagship iPhone 7 Plus is a high-end cellphone and it has two accelerometers onboard. The first one is a high-sensitivity power-hungry accelerometer that is used for optical image stabilization, while the second is manufactured by STMicroelectronics for motion tracking and it is contained within LSM6DSM, a 6-axis IMU that also encompasses a gyroscope [40]. Since the target here is a moderate performance, the specs of the second unit are used in the comparison. The accelerometer works in high-performance or normal mode. The cellphone uses the normal mode most of the time to preserve battery power, so the normal mode specs are listed in the table to give a fair comparison.

### 5.3.2 Design Process

The design presented here adopts a readout circuit that is capable of reading the accelerometer output and converting it to data that is sent to the processing or control unit. Sometimes the readout circuit needs to be tuned to match the performance of the MEMS sensor. Since the focus of this research is not on the readout circuit part, a commercial solution is used. The main requirement is for it to be able to read a differential capacitance with high resolution, then send the readings to the controller. Browsing the available readout chips on the market, the AD7746 from Analog Devices was chosen [41]. It has a high resolution down to 4 aF and can communicate with the controller in the I<sup>2</sup>C and SPI protocols, which makes the test setup design easier. On the other hand, it has a long capacitance conversion time, since it is not customized to the target design but a generic solution that covers a wide range of inputs. Moreover, it is limited to a 10 Hz to 90 Hz update rate, which confines the measured bandwidth, but is sufficient to test other performance parameters. However, this means that the bandwidth is not a primary target

here, since it should be less than the slow update rate in this specific case. Instead, the target is a combination of sensitivity, TNEA, and damping ratio.

Regarding the MEMS design, the 3D fabrication process has design limitations as well. The structural layer and the platform layer should be less than 3  $\mu\text{m}$  thick. To avoid protracted release times, the sacrificial layer thickness should not be less than 100 nm or more than 500 nm, in order to ensure satisfactory performance. The platform width is limited by the photolithography process to 9  $\mu\text{m}$ . The process limitations are discussed in detail in the next chapter, which describes the fabrication process. The design targets a device with a 500  $\mu\text{m} \times 500 \mu\text{m}$  size. Targeting larger sizes could cause problems in the structure out-of-plane bending and built-in residual stresses, while smaller sizes may not result in the required performance. The overall dynamic body acceleration of human beings during different activities is well within the  $\pm 2 \text{ g}$  range, which makes this range a realistic target [35]. The range is also restricted by the fact that an open-loop system is used here, which limits the range compared to a closed-loop system.

In most lateral sensing accelerometers, the rectangular proof mass is suspended using four supporting beams, with one in each corner. Such an arrangement reduces or eliminates the temperature and stress variations on the beams and ensures a stable structure. Nevertheless, using only two long beams to support the proof mass has been demonstrated previously in other MEMS devices, e.g. thermal imaging sensors [42]. If a film with good mechanical properties is used in the structural layer, this arrangement increases the accelerometer sensitivity as it decreases the structure stiffness. In this design, the supporting beam length was set to 435  $\mu\text{m}$ , leaving 65  $\mu\text{m}$  for the anchoring and bonding area, while its width was set to a 4  $\mu\text{m}$  Z-shaped beam. The structural layer thickness was set to 2  $\mu\text{m}$ , hence,  $w_a$  was 1  $\mu\text{m}$  and  $w_b$  was 3  $\mu\text{m}$ .

A mathematical model based on the design equations described in the previous section was used to determine the optimum gap that would result in the best sensitivity, the least noise, and the required bandwidth. Figure 5.9 (a) shows the resulting sensitivity and noise of the accelerometer based on the aforementioned design parameters, where the minimum TNEA is obtained when the gap is 350 nm. At that value, the damping ratio is 0.41, while the optimum damping ratio of 0.707 is achieved at 290 nm, as depicted in

Figure 5.9 (b). By targeting the optimum damping ratio, the TNEA increases by only 30  $\mu\text{g}/\sqrt{\text{Hz}}$ , which can be tolerated. Table 5.4 lists the targeted design parameters to achieve the required performance.

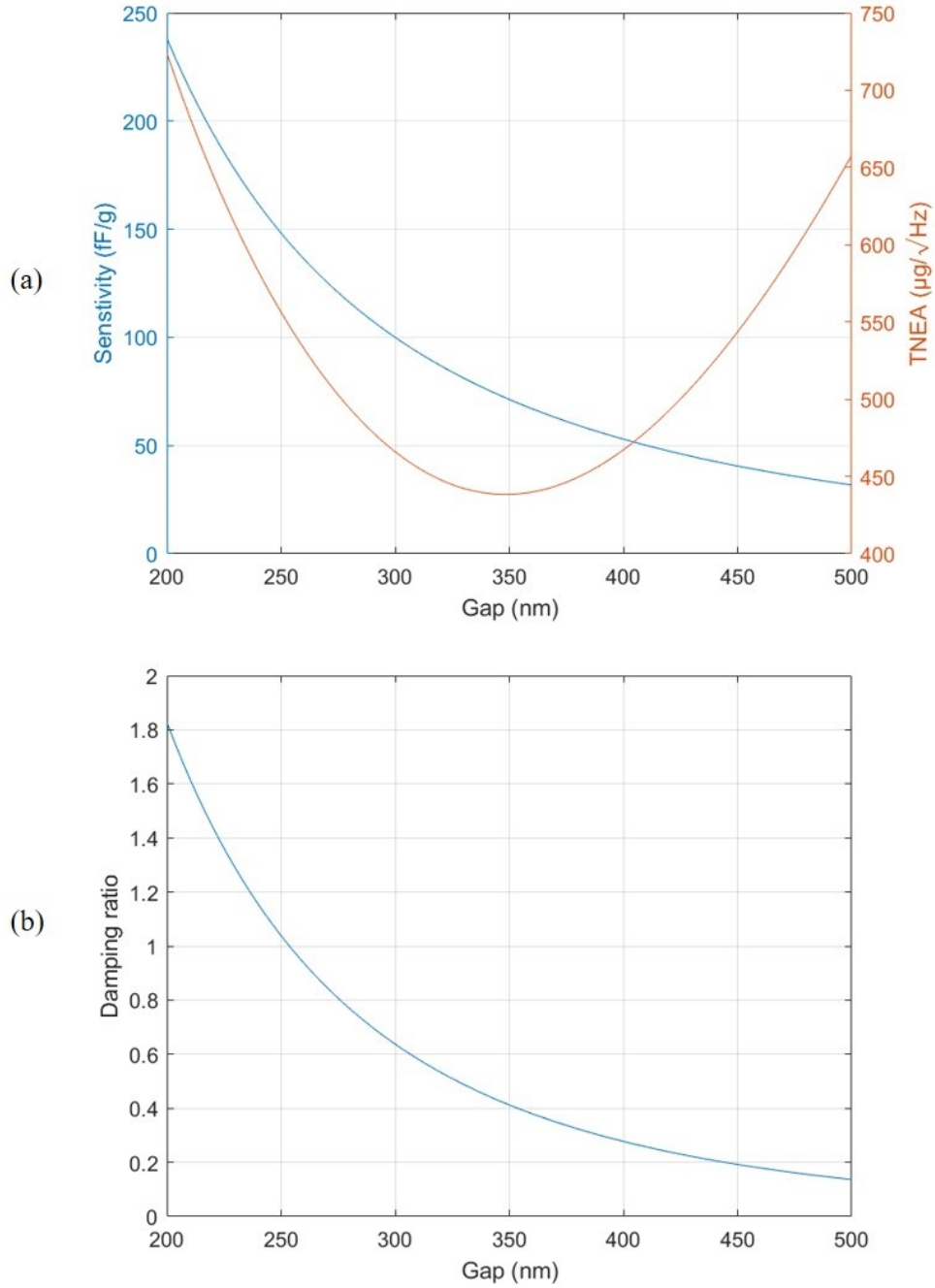


Figure 5.9: The sacrificial layer thickness for the target design based on curves of (a) sensitivity and TNEA, and (b) damping ratio versus gap.

Table 5.4: Targeted design specifications.

Parameter	Value
Device size (mm <sup>2</sup> )	0.5 × 0.5
Platform thickness (μm)	2
Structural layer thickness (μm)	2
Sacrificial layer thickness (nm)	290
Supporting beam length (μm)	435
Supporting beam width (μm)	$w_a=1$ $w_b=3$
Number of platforms	23
Platform length (μm)	480
Platform width (μm)	9

#### 5.4 Device Fabrication

After setting the target device parameters, the accelerometer was fabricated in a simple 3D process using non-conductive material to build the main structural parts. This process was developed specifically to meet the requirements of this accelerometer design. The platforms were created using polyimide, the bottom electrodes covering the platform sides were built using aluminum, and the proof mass and the top electrode were created using silicon nitride and aluminum layers. The gap was defined using a sacrificial layer created with a thin layer of parylene. This surface micromachining process is described in more details in the next chapter.

Figure 5.10 (a) presents an SEM image of the platforms with the bottom electrodes created on their sides. It is critical to ensure that the electrodes do not have any discontinuity on the platform sides, which in turn puts limits on the platform thickness. As seen in the image, each set of electrodes is electrically interconnected on one side of the accelerometer using the same layer that is used to fabricate the bonding pads. Figure 5.10 (b) shows the accelerometer after complete fabrication. The platforms are now covered with the proof mass that follows their shape. The proof mass contains multiple release holes distributed hexagonally to reduce the etching time needed to release the structure.



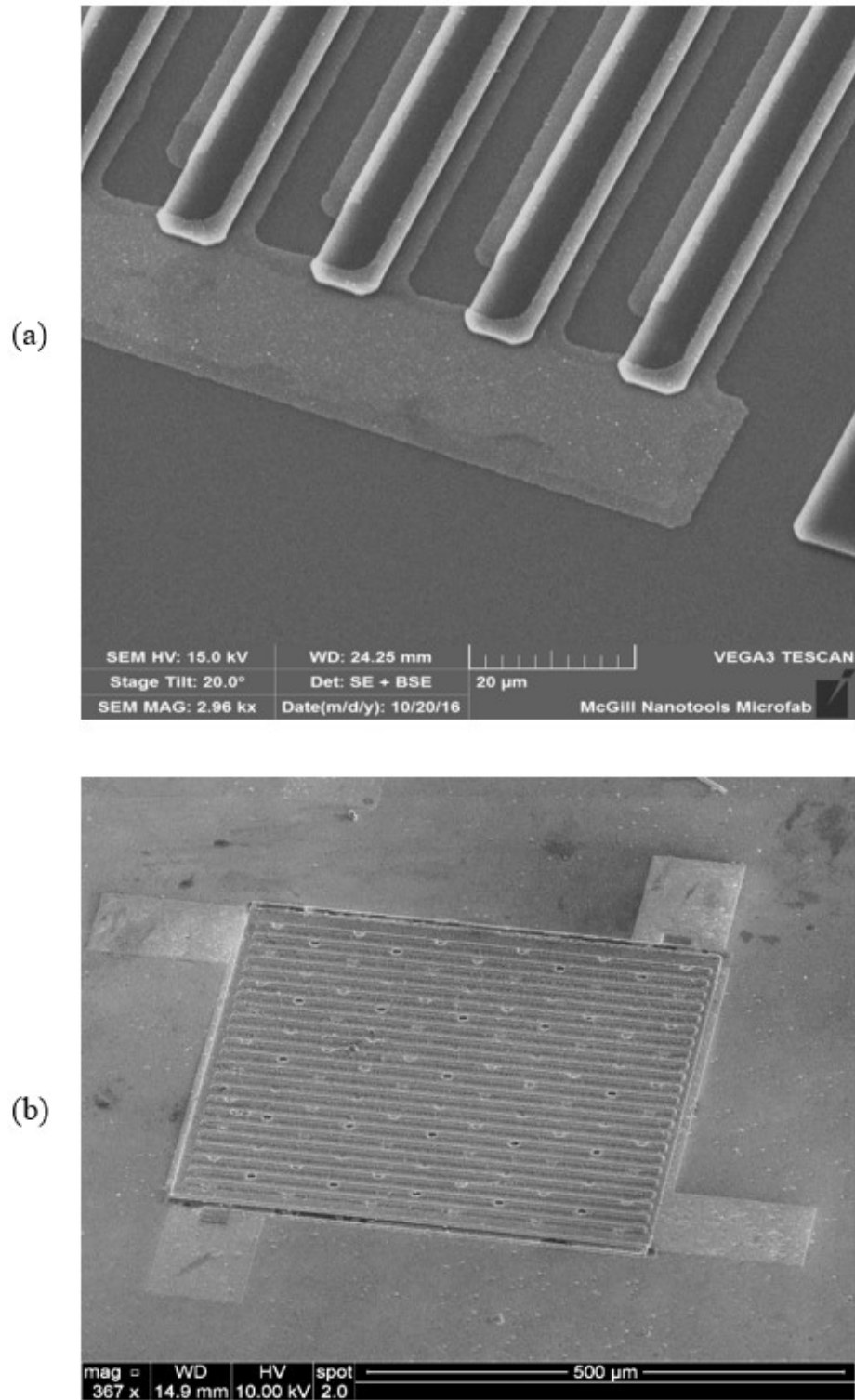


Figure 5.10: SEM images of (a) the platforms and the bottom electrodes only and (b) the final fabricated device.

Figure 5.11 (a) provides a zoomed-in view of a release hole through which the different design layers can be seen. The image shows the edge of the platform where the bottom electrode is visible. It also shows the gap created after etching the sacrificial layer. The top electrode can be recognized by its slightly brighter color just beneath the proof mass structural layer. The final thickness of the capacitive gap is 290 nm; this would result in a 0.7 damping ratio, which should be the optimum value for the accelerometer operation. Figure 5.11 (b) shows the resulting Z-shaped supporting beam, where  $w_a$  and  $w_b$  can be identified even though their sides are not smooth due to the etching process conditions. This is explained in the next chapter.

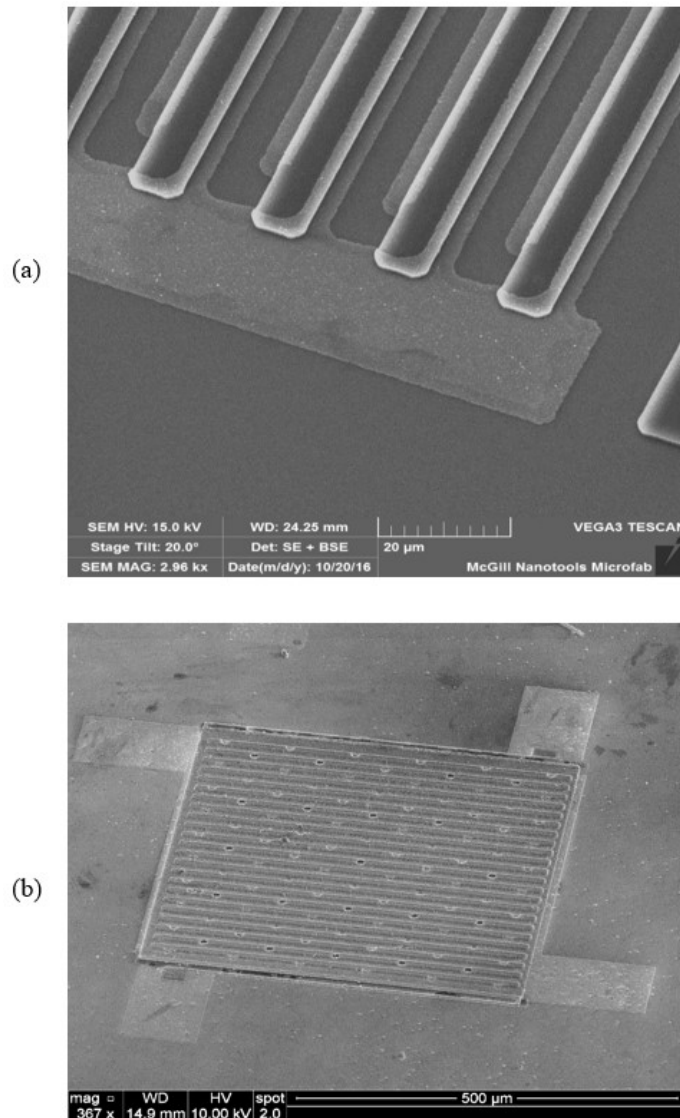


Figure 5.11: SEM image of (a) a release hole, and (b) the Z-shaped supporting beam.

## 5.5 Accelerometer Testing

The fabricated accelerometer was attached to a PCB where its differential capacitance was read by an AD7746 CDC and readings were calibrated against a commercial accelerometer (Figure 5.12). A gold surface finish was used in the PCB to enable direct wire-bonding from the bonding pads to the PCB. This strategy was employed to reduce the parasitic capacitance between the accelerometer and the PCB. The CDC was set to its smallest possible excitation voltage (0.41 V) on the electrodes when reading the capacitance to avoid pull-in of the proof mass. The accelerometer was tested using a rotary motion simulator that provided constant input acceleration. Further details about the test setup are provided in the appendix of the thesis. Ideally, a signal generator should be connected to one of the bottom electrodes and a signal analyzer should be connected to the proof mass top electrode to find the BNEA. The signal spectrum has to cover the frequency at which the accelerometer oscillates on a dynamic mechanical shaker. This test could not be done here since the used setup generates constant acceleration (0 Hz) and the available signal analyzer cannot go below 3 Hz. Therefore, the noise analysis for the accelerometer and the CDC was obtained using an AD4476 evaluation board, which outputs peak-to-peak capacitance noise. Although this method did not measure the TNEA directly, it represented a useful characterization parameter.

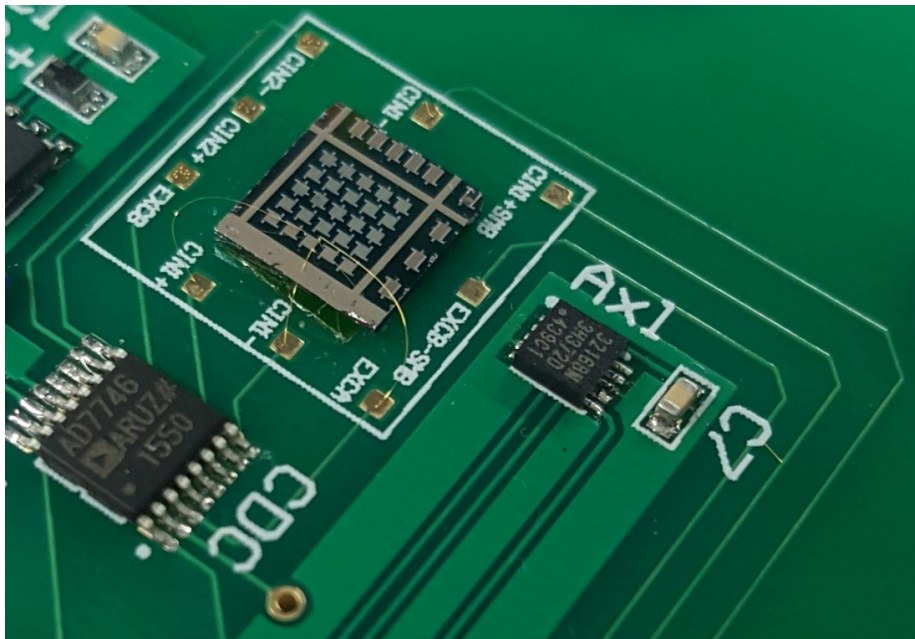


Figure 5.12: The fabricated accelerometer die onboard the testing PCB.

Figure 5.13 (a) shows a line of the best fit of the measured sensitivity instances versus the applied accelerations. The accelerometer outputs 58 fF per g over the full input range with about 2.8% full-scale nonlinearity. To maintain linear output, the maximum displacement should not exceed one-third of the initial capacitive gap [43, 44]. For a capacitive gap of 300 nm (250 nm air and 50 nm insulating layer), the maximum range that was tested was  $\pm 4$  g, which should result in about a 100 nm of displacement. A 4-g acceleration input was applied to the lateral axis perpendicular to the sensing axis, resulting in about 1.2% cross-sensitivity. The total noise of the accelerometer and the CDC is depicted in Figure 5.13 (b), which represents 500 samples collected while holding the PCB under constant 1 g acceleration. The measured peak-to-peak noise is 167 aF, which translates to 2.9 mg peak-to-peak acceleration noise at 0 Hz.

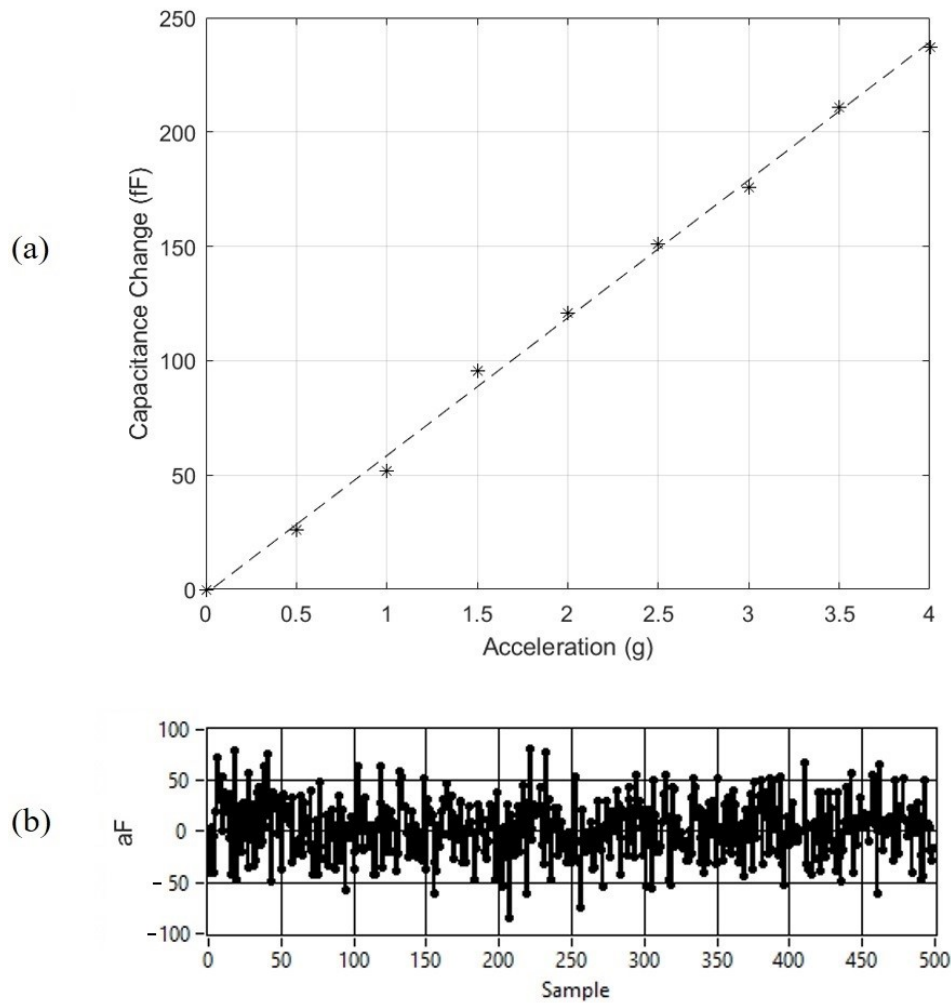


Figure 5.13: The measured (a) sensitivity, and (b) noise.

## 5.6 Discussion

Table 5.5 compares the performance of this work against lateral capacitive gap-closing accelerometers that have been fabricated using surface, SOI, and bulk fabrication methods. It can be seen that the work introduced here outperforms the surface micromachined accelerometers in terms of sensitivity, but falls behind the large SOI and bulk micromachined devices. This shows the benefits of using narrow capacitive gaps even when a thinner structural layer is used. However, the accelerometer sensitivity does not represent a fair metric since it is possible to increase the device size to obtain a higher sensitivity. As such, the sensitivity per unit area was added to the compared parameters to normalize the performance and show the benefits of the new design introduced here.

The accelerometer demonstrates excellent sensitivity with reasonable linearity even though the measured sensitivity is less than the expected value. Considering that the sacrificial layer thickness was characterized at the edge of the wafer away from the tested accelerometer located near the wafer center. Hence, a larger gap in the accelerometer die is most probably the cause of this difference. Ignoring the top electrode and the insulating layers when deriving the model might also affect the accuracy of the model. This high sensitivity can be credited to three main design choices: the increased capacitive area, the narrow gap, and the low-stiffness supporting beams. Even by adopting the four-beam configuration, the sensitivity would still be high compared to that of other surface micromachined accelerometers.

Table 5.5: Performance comparison with other lateral accelerometers.

	[45]	[46]	[47]	[48]	[4]	[49]	<b>This work</b>
<b>Fabrication method</b>	Surface	Surface	SOI	SOI	Bulk	Bulk	Surface
<b>Area (mm<sup>2</sup>)</b>	0.258	2.06	6.6	14	2.4	35	0.25
<b>Gap (μm)</b>	2.3	2	3.2	2	1.1	4.3	0.3
<b>Thickness (μm)</b>	9	5	120	40	500	500	4.5
<b>Sensitivity (fF/g)</b>	1.9	18	140	200	5600	35000	58
<b>TNEA (μg/√Hz)</b>	289	145	100	110	1.6	0.2	1440
<b>Range (g)</b>	±6	±10	±1	±1	±0.6	±0.03	±4
<b>Sensitivity per area (fF/g.mm<sup>2</sup>)</b>	7.4	8.74	21.2	14.29	2333	1000	232

As a disadvantage, this accelerometer shows sub-par noise floor performance, and the measured noise value is 3 orders of magnitude higher than the expected TNEA. Since the BNEA cannot reach such a value, it is assumed that most of that noise originates from the CDC rather than the MEMS accelerometer. By designing a customized closed-system readout circuit and increasing the device stiffness, the TNEA can be reduced to acceptable levels. While this would lessen the sensitivity, the benefits of the closed-loop system design would outweigh its drawbacks.

## 5.7 Design Improvements

The accelerometer design described in this chapter is an open-loop design implemented in a four-mask process. The design layout and the fabrication process are intended to be simple to avoid fabrication difficulties. Nevertheless, there are possible improvements that could be applied to enhance performance. Two possible improvements in the design and the fabrication process are suggested below.

### 5.7.1 Addition of Mechanical Stoppers

In the current design, an insulating layer is placed beneath the top electrode to prevent short-circuits when the accelerometer experiences high accelerations. The disadvantage of this method is the likelihood that the capacitance will exceed the input range. This may occur when the proof mass touches the platforms and the thin insulating layer is the only separation between the two electrodes (Figure 5.14 (a)). One solution is to add an extra mask that patterns an extra layer of the same sacrificial material used to define

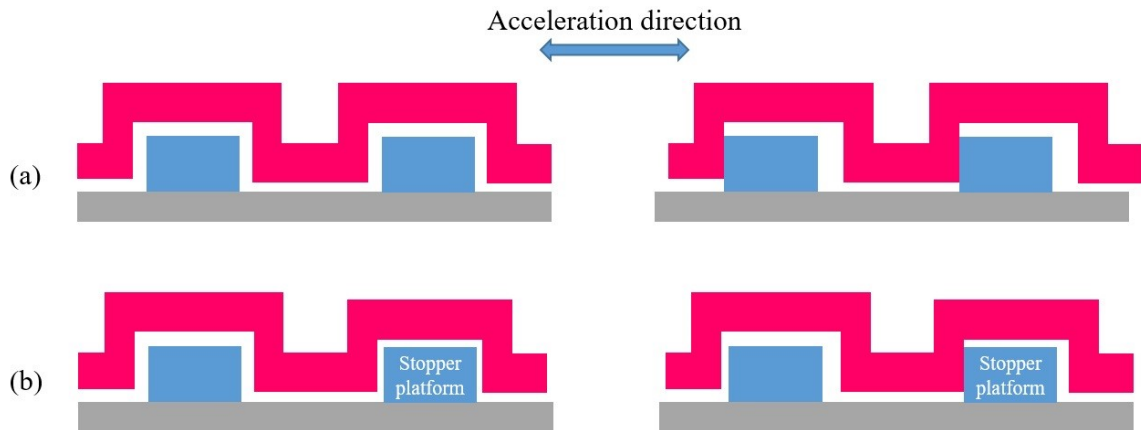


Figure 5.14: Gap under high accelerations (a) without and (b) with the stopper.

the gaps. This layer would be used to generate narrower gaps over dedicated stopper platforms with no electrodes on their surfaces, which stops the proof mass from touching the platforms with the electrodes, and prevents both vertical and lateral touches (Figure 5.14 (b)). The thickness of this extra layer determines the allowed displacement and also contributes to the final capacitive gap. Namely, if the allowed displacement is 100 nm and the target gap is 300 nm, the layers thicknesses would be 100 and 200 nm in sequence. By adding this layer, the need for the thin insulating layer is eliminated. It also prevents electrode damage due to frequent mechanical shocks.

### 5.7.2 Closed-Loop System Design

The focus in this thesis has been on demonstrating the proposed new design by developing it in an open-loop system, instead of the more sophisticated closed-loop system. Nevertheless, the closed-loop design can be realized easily by editing the design presented above. Such a design may be considered when a higher performance is needed, or to eliminate the vertical cross-input by actuation. Figure 5.15 shows the simplified design of the bottom electrodes for a the closed-loop system. For each side, the design employs three bottom electrodes instead of only one. The first electrode is used to sense acceleration, as shown for the open-loop design described above. The second electrode is mainly for horizontal actuation, and it is Z-shaped and positioned on the top and the side of the platform. Finally, the third electrode is placed on top of the platform or in the trench or both, but not on the platform sides. For control in both directions of the sensing axis, six electrode sets would be needed.

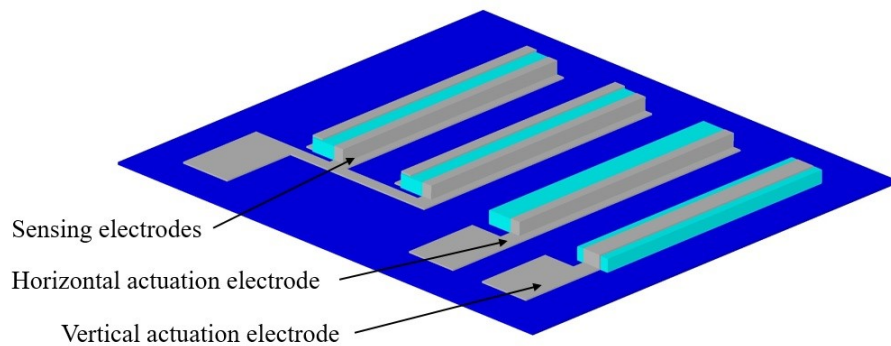


Figure 5.15: Simplified design of one set of the bottom electrodes for a closed-loop system.

When an input acceleration is experienced by the system, the capacitance read by the sensing electrodes changes. Then, an electrostatic force is applied between the horizontal actuation electrode and the proof mass. This force moves the proof mass horizontally to its neutral no-input position. Due to the shape of the horizontal actuation electrode, it also applies a vertical force on the proof mass, causing it to move vertically, which may alter the output readings. The role of the third electrode is then to apply an electrostatic force in the opposite vertical direction to keep the proof mass in its vertical neutral axis. Because of the small gaps, the voltage needed for the electrostatic force is small but needs precise control. To restore a proof mass to its neutral position, the electrostatic force must be equal to the force that bends the supporting beams [50]. The voltage,  $V$ , generating the needed electrostatic force can be derived as follows:

$$F_E = F_M, \quad (5.23)$$

$$\frac{\varepsilon AV^2}{2(d-x)^2} = kx, \text{ and} \quad (5.24)$$

$$V = \sqrt{\frac{2kx(d-x)^2}{\varepsilon A}}. \quad (5.25)$$

## 5.8 Conclusion

This chapter has presented a complete description of a novel acceleration sensor design. The design utilizes a 3D platform process with a narrow capacitive gap to create a high-sensitivity accelerometer. This is accomplished by using the entire area for sensing and for proof mass, instead of the tradeoff relation present in 2D designs. A unique feature of this design is its ability to control the capacitive area, stiffness, and proof mass independently, unlike the 2D design where they are all controlled by the same layer. Another advantage of this design is its ability to use non-conductive materials as structure layers. To overcome the vertical displacement problem caused by the narrow gap and large proof mass, a new Z-shaped supporting beam is used. The device was fabricated successfully in-house using a newly developed 3D surface micromachining process. The measured sensitivity was 58 fF/g, which surpasses any surface micromachined accelerometer, and it exhibited good linearity. The noise performance was not as expected,



however, as the TNEA reached about  $1440 \mu\text{g}/\sqrt{\text{Hz}}$ . This can be improved by changing the configuration of the supporting beams and using an optimized custom IC.

This design allows for building above-IC high-sensitivity accelerometers, or even for their integration in controller chip packages. Nevertheless, the IC surface will need to be polished before starting to build this accelerometer, in order to ensure that it has planar structures (platforms, proof mass, ...). Moreover, different sensitivities can be realized by changing the device width and readjusting the gap and the supporting beam designs. This design can also be used to build nano electro mechanical systems (NEMS) accelerometers with higher sensitivities, or for different IoT or wearable electronic applications.

## 5.9 References

- [1] A. Alfaifi, I. A. Alhomoudi, and M. N. El-Gamal, "Optimization of in-plane SiC capacitive accelerometers design parameters," in *New Circuits and Systems Conference (NEWCAS), 2016 14th IEEE International*, 2016, pp. 1-4: IEEE.
- [2] J. Chae, H. Kulah, and K. Najafi, "An in-plane high-sensitivity, low-noise micro-g silicon accelerometer," in *Micro Electro Mechanical Systems, 2003. MEMS-03 Kyoto. IEEE The Sixteenth Annual International Conference on*, 2003, pp. 466-469: IEEE.
- [3] J. Chae, H. Kulah, and K. Najafi, "A monolithic three-axis micro-g micromachined silicon capacitive accelerometer," *Journal of Microelectromechanical systems*, vol. 14, no. 2, pp. 235-242, 2005.
- [4] J. Chae, H. Kulah, and K. Najafi, "An in-plane high-sensitivity, low-noise micro-g silicon accelerometer with CMOS readout circuitry," *Journal of microelectromechanical systems*, vol. 13, no. 4, pp. 628-635, 2004.
- [5] M.-H. Tsai, C.-M. Sun, C. Wang, J. Lu, and W. Fang, "A monolithic 3D fully-differential CMOS accelerometer," in *Nano/Micro Engineered and Molecular Systems, 2008. NEMS 2008. 3rd IEEE International Conference on*, 2008, pp. 1067-1070: IEEE.
- [6] W. C. Young and R. G. Budynas, *Roark's formulas for stress and strain*. McGraw-Hill New York, 2002.
- [7] R. D. Blevins, *Formulas for Dynamics, Acoustics and Vibration*. John Wiley & Sons, 2015.
- [8] F. Beer, J. DeWolf, E. R. Johnston Jr, and D. Mazurek, "Mechanics of materials," 2014.
- [9] B. J. Goodno and J. M. Gere, *Mechanics of Materials*. Cengage Learning, 2016.
- [10] E. Oñate, *Structural analysis with the finite element method. Linear statics: volume 2: beams, plates and shells*. Springer Science & Business Media, 2013.
- [11] J. N. Reddy, *An Introduction to Nonlinear Finite Element Analysis: with applications to heat transfer, fluid mechanics, and solid mechanics*. OUP Oxford, 2014.
- [12] J. J. Allen, *Micro electro mechanical system design*. CRC Press, 2005.

- [13] G. Cowper, "The shear coefficient in Timoshenko's beam theory," 1966: ASME.
- [14] M. Levinson, "A new rectangular beam theory," *Journal of Sound and vibration*, vol. 74, no. 1, pp. 81-87, 1981.
- [15] B. V. Amini and F. Ayazi, "Micro-gravity capacitive silicon-on-insulator accelerometers," *Journal of micromechanics and microengineering*, vol. 15, no. 11, p. 2113, 2005.
- [16] T. B. Gabrielson, "Mechanical-thermal noise in micromachined acoustic and vibration sensors," *IEEE transactions on Electron Devices*, vol. 40, no. 5, pp. 903-909, 1993.
- [17] G. Karniadakis, A. Beskok, and N. Aluru, *Simple Fluids in Nanochannels*. Springer, 2005.
- [18] M. Tilli, T. Motooka, V.-M. Airaksinen, S. Franssila, M. Paulasto-Krockel, and V. Lindroos, *Handbook of silicon based MEMS materials and technologies*. William Andrew, 2015.
- [19] M. Bao and H. Yang, "Squeeze film air damping in MEMS," *Sensors and Actuators A: Physical*, vol. 136, no. 1, pp. 3-27, 2007.
- [20] S. FUKUI and R. KANEKO, "Analysis of ultra-thin gas film lubrication based on the linearized Boltzmann equation: influence of accommodation coefficient," *JSME international journal*, vol. 30, no. 268, pp. 1660-1666, 1987.
- [21] E. Lemmon and R. Jacobsen, "Viscosity and thermal conductivity equations for nitrogen, oxygen, argon, and air," *International journal of thermophysics*, vol. 25, no. 1, pp. 21-69, 2004.
- [22] T. Veijola, H. Kuisma, J. Lahdenperä, and T. Ryhänen, "Equivalent-circuit model of the squeezed gas film in a silicon accelerometer," *Sensors and Actuators A: Physical*, vol. 48, no. 3, pp. 239-248, 1995.
- [23] M.-H. Bao, *Micro mechanical transducers: pressure sensors, accelerometers and gyroscopes*. Elsevier, 2000.
- [24] N. J. Mansfield, *Human response to vibration*. CRC press, 2004.
- [25] M.-H. Bao, *Micro mechanical transducers: pressure sensors, accelerometers and gyroscopes*. Elsevier, 2000.
- [26] V. Kempe, *Inertial MEMS: principles and practice*. Cambridge University Press, 2011.
- [27] M. I. Younis, *MEMS linear and nonlinear statics and dynamics*. Springer Science & Business Media, 2011.
- [28] K. Kalantar-Zadeh, *Sensors: an introductory course*. Springer Science & Business Media, 2013.
- [29] P. Wang and Q. Liu, *Biomedical sensors and measurement*. Springer Science & Business Media, 2011.
- [30] S. Prosser, "Aerospace Sensor Systems and Applications," ed: IOP Publishing, 1998.
- [31] S. Levy and W. D. Kroll, "Response of accelerometers to transient accelerations," *Journal of Research of the National Bureau of Standards*, vol. 45, no. 4, pp. 303-309, 1950.
- [32] W. S. Levine, *The Control Handbook: Control System Fundamentals*. CRC press, 2010.

- [33] J. Musić, R. Kamnik, and M. Munih, "Model based inertial sensing of human body motion kinematics in sit-to-stand movement," *Simulation Modelling Practice and Theory*, vol. 16, no. 8, pp. 933-944, 2008.
- [34] E. Jovanov, A. Milenkovic, C. Otto, and P. C. De Groen, "A wireless body area network of intelligent motion sensors for computer assisted physical rehabilitation," *Journal of NeuroEngineering and rehabilitation*, vol. 2, no. 1, p. 6, 2005.
- [35] E. L. Shepard *et al.*, "Derivation of body motion via appropriate smoothing of acceleration data," *Aquatic Biology*, vol. 4, no. 3, pp. 235-241, 2008.
- [36] Y.-J. Hong, I.-J. Kim, S. C. Ahn, and H.-G. Kim, "Mobile health monitoring system based on activity recognition using accelerometer," *Simulation Modelling Practice and Theory*, vol. 18, no. 4, pp. 446-455, 2010.
- [37] X. Yun and E. R. Bachmann, "Design, implementation, and experimental results of a quaternion-based Kalman filter for human body motion tracking," *IEEE transactions on Robotics*, vol. 22, no. 6, pp. 1216-1227, 2006.
- [38] STMicroelectronics, "LIS2DH MEMS digital output motion sensor: ultra low-power high performance 3-axis "femto" accelerometer," 2011.
- [39] B. Sensortec, "BMI055 Small, versatile 6DoF sensor module," 2014.
- [40] STMicroelectronics, "LSM6DSM iNEMO inertial module: always-on 3D accelerometer and 3D gyroscope," 2016.
- [41] Analog Devices Inc., "24-bit Capacitance-to-Digital Converter with Temperature Sensor, AD7745/AD7746," 2005.
- [42] R. Wood, "High-performance infrared thermal imaging with monolithic silicon focal planes operating at room temperature," in *Electron Devices Meeting, 1993. IEDM'93. Technical Digest., International*, 1993, pp. 175-177: IEEE.
- [43] E. K. Chan and R. W. Dutton, "Electrostatic micromechanical actuator with extended range of travel," *Journal of microelectromechanical Systems*, vol. 9, no. 3, pp. 321-328, 2000.
- [44] C.-H. Han, D.-H. Choi, and J.-B. Yoon, "Parallel-plate MEMS variable capacitor with superior linearity and large tuning ratio using a leveraging structure," *Journal of Microelectromechanical Systems*, vol. 20, no. 6, pp. 1345-1354, 2011.
- [45] S.-H. Tseng, M. S. Lu, P.-C. Wu, Y.-C. Teng, H.-H. Tsai, and Y.-Z. Juang, "Implementation of a monolithic capacitive accelerometer in a wafer-level 0.18  $\mu\text{m}$  CMOS MEMS process," *Journal of Micromechanics and Microengineering*, vol. 22, no. 5, p. 055010, 2012.
- [46] I. E. Gonenli, Z. Celik-Butler, and D. P. Butler, "Surface micromachined MEMS accelerometers on flexible polyimide substrate," *IEEE Sensors Journal*, vol. 11, no. 10, pp. 2318-2326, 2011.
- [47] J. Chae, H. Kulah, and K. Najafi, "A hybrid silicon-on-glass (SOG) lateral micro-accelerometer with CMOS readout circuitry," in *Micro Electro Mechanical Systems, 2002. The Fifteenth IEEE International Conference on*, 2002, pp. 623-626: IEEE.
- [48] B. V. Amini and F. Ayazi, "A 2.5-V 14-bit/spl Sigma//spl Delta/CMOS SOI capacitive accelerometer," *IEEE Journal of Solid-State Circuits*, vol. 39, no. 12, pp. 2467-2476, 2004.

- [49] R. Abdolvand, B. V. Amini, and F. Ayazi, "Sub-micro-gravity in-plane accelerometers with reduced capacitive gaps and extra seismic mass," *Journal of microelectromechanical systems*, vol. 16, no. 5, pp. 1036-1043, 2007.
- [50] M. Tabib-Azar, *Microactuators: electrical, magnetic, thermal, optical, mechanical, chemical & smart structures*. Springer Science & Business Media, 2013.

---

# Chapter 6

## 3D Surface Micromachining Process for Above-IC Integration

---

### 6.1 Introduction

Capacitive MEMS surpass other types of sensing schemes, due to the multiple advantages of capacitive sensing discussed earlier. On the other hand, they need narrow capacitive gaps to deliver superior performance, and the capabilities of detecting miniscule displacements or body deformations. Fabrication processes can be classified based on the number of axes that can be sensed by sensors created in these processes. 1D processes usually use a material with good mechanical properties as the structural layer above a metallic layer. The latter forms the top electrode, which moves vertically [1]. In 2D processes, the structural layer is conductive and is used to sense the motion of the moving electrode in the two lateral axes [2]. Finally, 3D processes can create capacitive gaps to detect motion laterally and vertically [3]. This type of process usually has a complicated flow and requires multiple lithography steps to create the final structure and gaps.

The 1D and 2D surface fabrication processes provide relatively simple methods of sensing and actuation in a fabricated MEMS. Still, their limitations outweigh this gain when high-performance devices are needed. One of the major drawbacks in these processes is the fairly large lateral gaps that are obtained using ultra violet (UV) photolithography. While vertical gaps can be obtained by using thin sacrificial layers, lateral gaps are limited by the photolithography and etching steps. A high-resolution mask is needed to create sub-micrometer gaps using UV photolithography. Moreover, the photoresist type and thickness and the UV exposure dose also need to be finely tuned to define these narrow gaps. The required directional reactive ion etching (RIE) step also generates additional challenges in forming these gaps. Submicron lateral gaps have been previously demonstrated in various

2D processes [4-7]. However, these processes have high thermal budgets that prevents their integration above their ASIC's.

3D surface micromachining processes can be used to build complex shapes that are otherwise impossible to create. Such processes have been previously demonstrated, both commercially and in research labs. In 2D processes, lateral gaps are created by patterning conductive layers. On the other hand, lateral gaps in 3D processes are created by etching the sacrificial layer between two overlapping layers. An example of a 3D process is PolyMUMPs, which uses polysilicon and oxides to create the 3D structures with gaps in all axes [8]. As seen in Figure 6.1, narrow lateral gaps can be created by overlapping Poly2 with Poly1. When the second oxide is etched, it leaves a 750-nm capacitive gap, but the overlap height is limited to 750 nm. These processes are usually complicated, need many lithography print steps, and require conductive materials.

This chapter reviews the development of a CMOS-compatible 3D process for above-IC integration. This process can be used to create narrow lateral and vertical gaps, where it utilizes platforms (or structural layers) to create the required 3D shapes. One of the most important features of the process is its ability to use non-conductive materials with good mechanical properties as structural layers. The following section reports the reasoning behind the material selection based on the targeted shape. Next, the fabrication process is reviewed, and details are provided about each step in the process. The subsequent section describes the difficulties and problems faced during fabrication and how to solve them, and this is followed by a section that suggests further process parameter improvements. Subsequently, the process is compared to other similar state-of-the-art fabrication processes used to create narrow lateral gaps. Finally, a conclusion summarizes this chapter and the process potential in terms of creating other applications.

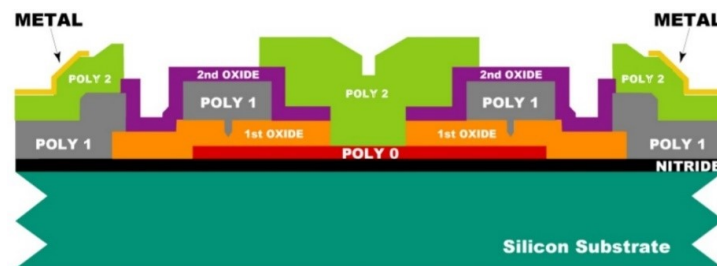


Figure 6.1: Cross-section of PolyMUMPs layers [8].

## 6.2 Materials Selection

The cross-section of the process final structure is shown in Figure 6.2. The structure is created using deposition or spinning (additive step), and it is then etched using dry or wet etching (subtractive step). To achieve the targeted specs, all additive and subtractive steps must have a process temperature of less than 400 °C. Each layer must be resistant to the subsequent process steps and, hence, the description here is from top to bottom. Directional dry etching steps are used whenever possible to prevent the degradation of the critical dimensions resulting from the wet isotropic etching.

The top layer should be able to reach thicknesses of more than 2 μm, in order to obtain a large proof mass as needed. Moreover, the top layer's deposition process must be conformal, and it must also have a bottom-conducting layer to implement one capacitive or electrostatic electrode. Such layers are deposited using sputtering or low-temperature plasma-enhanced chemical vapor deposition (PECVD). To prove the concept of the process in using non-conductive materials for capacitive sensing, silicon nitride was chosen as the structural layer. Silicon nitride has attractive mechanical properties when deposited at 300 °C using PECVD as it has been reported to create low-stress films with ~2.8 g/cm<sup>3</sup> density and ~200 GPa Young's modulus [9-11]. A low stress layer of silicon nitride was deposited using PECVD at 300° C. The deposition rate was about 9 nm/sec using the following gas flow rates: SiH<sub>4</sub>:N<sub>2</sub>:NH<sub>3</sub> 190:2000:50 sccm. The stress was characterized using laser measurement to find the surface radius of curvature (ROC). Table 6.1 shows the tensile stress measured for the silicon nitride film at different thicknesses. The film stress,  $\sigma_f$ , was calculated using Stoney's equation [12, 13]:

$$\sigma_f = -\frac{E_s}{6(1-\nu_s)} \frac{t_s^2}{t_f} \left( \frac{1}{R} - \frac{1}{R_0} \right), \quad (6.1)$$

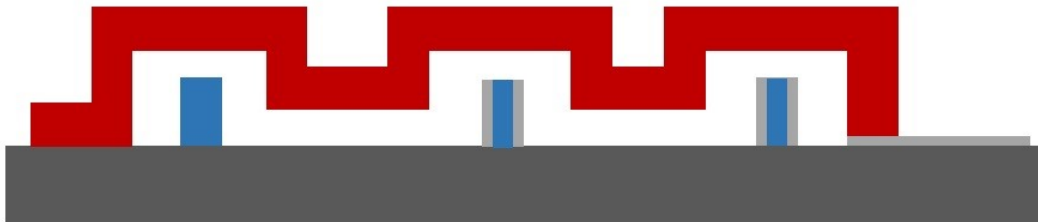


Figure 6.2: The targeted cross-section of the process final structure.

Table 6.1: Stress analysis of the silicon nitride film.

Film thickness ( $\mu\text{m}$ )	ROC ( $\mu\text{m}$ )	Stress (MPa)
0	0.07	-
0.5	0.06	38.6
1.0	0.16	29.9
1.5	0.56	49.3
2.0	0.75	43.9

where  $E_s$  is the Young modulus of the substrate,  $t_s$  is the substrate thickness,  $t_f$  is the film thickness,  $\nu_s$  is Poisson's ratio of the substrate, and  $R_0$  and  $R$  are the substrate radii of curvature before and after the film deposition. The silicon nitride is etched using RIE at a rate of 200 nm/min, with the etching gases having flow rates of  $\text{CHF}_3$ :Ar: $\text{CF}_4$  45:70:7 sccm. The top electrode is created beneath this layer, and this can be done using an aluminum layer that is sputtered at 17 nm/min using a DC of 1.0 A and  $22.55 \times 10^{-3}$  Torr chamber pressure. The layer can be conveniently wet etched in a hot bath of aluminum etchant type-A at a rate of 100 nm/min at a temperature of 30 °C. The thickness and properties of this layer determine the mass and strength of the moving structure. The structural layer thickness can be increased for devices that need a large proof mass or higher stiffness to enhance performance.

The capacitive gap is created using a sacrificial layer that must have good step coverage and deposition rate that can be controlled accurately in the nanometer range. Since the target thickness is in the submicron scale, the dry etching release step of the sacrificial layer should be used to avoid layers' stiction, which can happen when wet etching is used. Parylene is a polymer material that can be deposited using the chemical vapor deposition (CVD) process inside a chamber at room temperature. Since the film must sustain the PECVD temperature, parylene-N grade is used. It has a melting temperature of 410 °C, which makes it a better candidate than the more popular parylene-C, which starts melting at 290 °C [14, 15]. Parylene-N can be patterned using oxygen RIE and is etched in the oxygen plasma isotropic etching step to release the structure [16-18]. The thickness of this layer determines the capacitive gap, and it should take into consideration the voltage that will be applied between the electrodes.



The platforms should be made of a non-conductive material to enable the creation of the differential electrodes on both sides of each platform. Since it is the first layer to be created in the structure, the process restrictions are relaxed to match only those required by the ASIC wafer underneath it. The easiest way to create these platforms is to spin polyimide and cure it to make it able to survive the PECVD deposition temperature. The polyimide grade used here was PI-2555, since it creates 1.7 to 3.5  $\mu\text{m}$  thick layers in a simple spinning coating step [19]. It can also be patterned in oxygen plasma RIE. Next, the electrodes are created by depositing thin metallic films and patterning them. Aluminum serves as the best candidate, as this layer is also used as pads for probing or direct wire bonding. It is sputtered and patterned using the same process parameters described above. It is critical to adjust the deposition parameters of aluminum to generate a low-stress film, so that the aluminum layer does not peel off in the PECVD chamber later on. The thickness of this layer sets the capacitive area between the two electrodes. Table 6.2 summarizes the materials used in the process, with their deposition and etching methods. The number of different materials used in the process were kept to a minimum to reduce material compatibility issues.

### 6.3 Process Flow

The process went through several revisions in terms of layout design rules and process flow to ensure a simple fabrication process. The UV lithography steps were reduced to four to simplify the process further, and the used materials were also reduced to four. The photoresist used in the photolithography process is S1813 and is spun at 3000 rpm before it is soft baked at 115 °C for 60 seconds. The applied UV dose is 70 mJ in hard-contact mode, which is necessary to preserve the critical dimensions (CD) and obtain the best alignment results. The photoresist is then developed for 45 seconds before a hard bake step for 90 seconds at 90 °C.

Table 6.2: Deposition and etching conditions of process materials.

Layer	Deposition method	Step temperature	Etching type
Polyimide	Spinning	300	RIE
Aluminum	Sputtering	50	Wet
Parylene-N	CVD	25	RIE & plasma etching
Silicon nitride	PECVD	300	RIE

The process starts by dehydrating the wafer by either placing it inside a 150 °C oven for 30 minutes or using oxygen RIE for 5 minutes. This is followed by spinning and baking a VM-652 adhesion promoter on a bare silicon wafer to enhance the adhesion of the platform's polyimide layer. The polyimide is then spun on the wafer at 4000 rpm for 30 seconds to create a layer of 2.2  $\mu\text{m}$  thickness. It is crucial to ensure that the viscous polyimide dose has no air bubbles before spinning, as this would result in malformed platforms. The polyimide is then baked at 135 °C for 5 minutes, and subsequently cured in an air environment at 300 °C for 2 hours. The oven tolerance should be monitored, as curing the polyimide at temperatures higher than 320 °C will transition the layer into the glass phase, thereby preventing its patterning. Next, a 50-nm thin aluminum film is sputtered on top of the polyimide layer. The aluminum film is then patterned using photolithography steps and aluminum wet etchant, to create a hard mask for the polyimide. The full thickness of the polyimide is subsequently etched using oxygen RIE, and the aluminum hard mask is etched afterwards (Figure 6.3 (a)). Even using the adhesion promoter, the polyimide thin platforms might be detached because of the small connection area, especially when strong air-drying or fast flowing fluids are applied to the wafer. The polyimide is etched in the oxygen plasma asher used to release the device in the final step, leading to weak or defected hanging lower electrodes. To solve these two problems, a thin 300-nm conformal layer of silicon nitride is deposited using PECVD. This layer prevents polyimide platforms from final etching and it strengthens the thin platforms' connection to the wafer (Figure 6.3 (b)). The silicon nitride layer also provides electrical insulation between different electrodes, since a bare silicon wafer is used.

Next, the bottom electrodes are created on the polyimide platforms by sputtering a 300-nm aluminum layer. The layer is then patterned using the second photolithography step, which requires accurate alignment with the previous layer. A good and equal overlap distance between the differential electrodes and top of the platforms is required in this step (Figure 6.3 (c)). Notice that the platforms' dimensions will increase with the thicknesses of the aluminum and silicon nitride layers, and this must be taken into account when drawing the layout. This layer may also be used to create pads for wire bonding; here, its thickness should be at least 300 nm, although it may be made thinner if the layer is patterned to be connected to the pads of the ASIC of the device.

In the following step, the gap is defined with a thin sacrificial layer of parylene-N. The layer thickness is deposited at about 762 nm per hour using the CVD process. However, the layer final thickness depends on the dimer mass used, where 0.9 milligram results in 210 to 250 nm thickness depending on the wafer's vertical position inside the

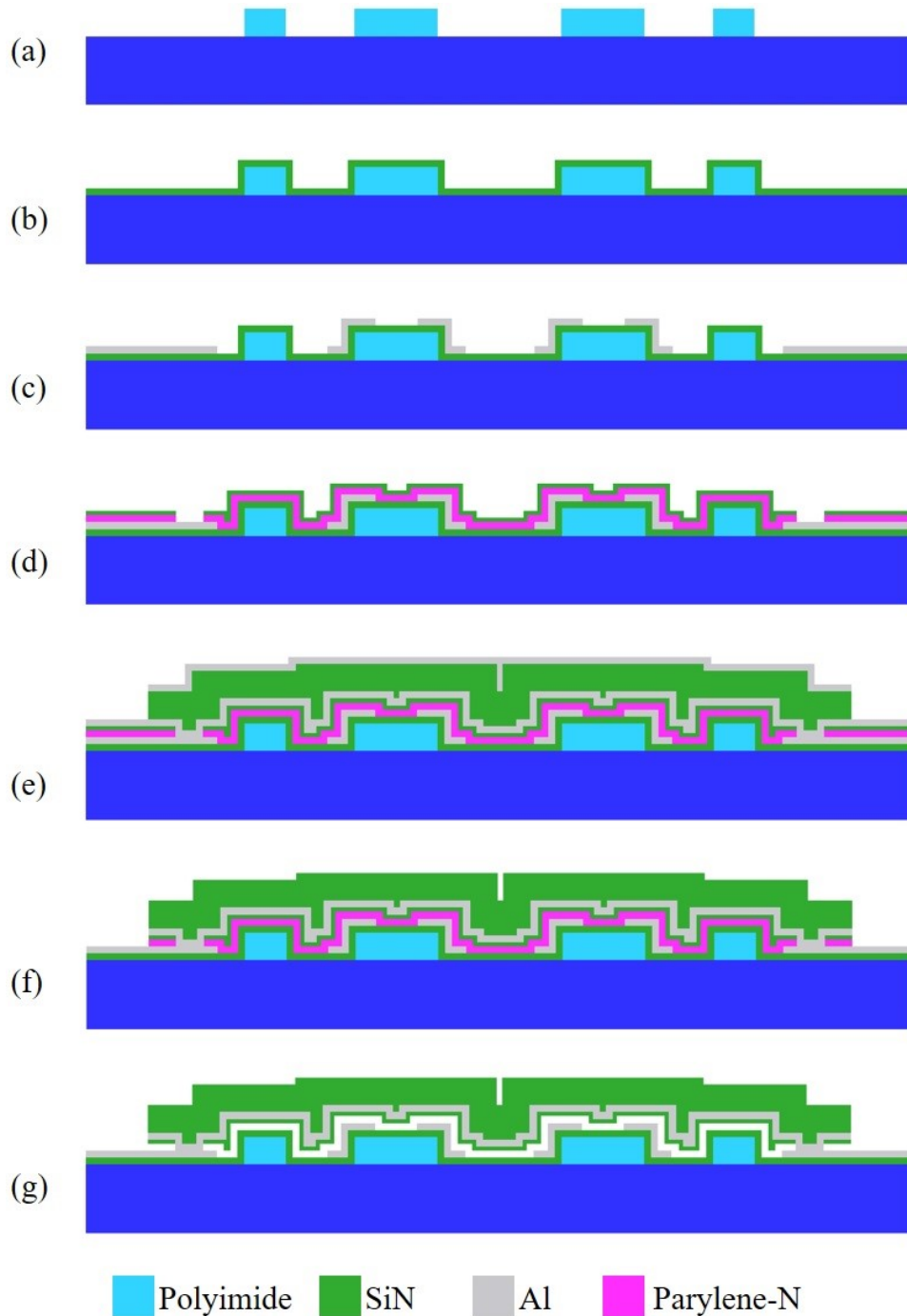


Figure 6.3: Cross-section of the process flow.

chamber. This is followed by a 50-nm layer of silicon nitride being deposited using PECVD. The purpose of this layer is to create an insulation between the top and bottom electrodes in case of high out-of-plane acceleration or proof mass collapse. This layer can be discarded if the design is rigid in the vertical axis and there is no concern regarding electrical short-circuit. Both layers are patterned in the third photolithography step using two subsequent RIE steps (Figure 6.3 (d)). This step defines both i) where the top electrode connects to its bonding pads, and ii) the anchors of the structural layer.

Next, aluminum, silicon nitride, and aluminum are deposited in sequence. The first aluminum layer is created by sputtering a 300-nm film used as the top electrode. A 2- $\mu\text{m}$  thick silicon nitride is then deposited using PECVD, followed by sputtering a 600-nm aluminum layer used as a hard mask. The final photolithography step is done to pattern the aluminum hard mask. This mask requires accurate alignment, if it has parts that overlap with the platforms, e.g. to form Z-shaped beams. The silicon nitride structural layer is then etched for a time equal to the silicon nitride and the polyimide thicknesses combined. As the main silicon nitride layer is etched, the top electrode aluminum layer becomes exposed, and it works as a mask for the rest of the structure (Figure 6.3 (e)). This step is explained in detail in the next section, as it is one of the major challenges in any 3D fabrication process. Subsequently, the aluminum hard mask and the exposed part of the top electrode are etched until the insulating silicon nitride layer is exposed. The silicon nitride and the parylene are then etched in two successive RIE steps; see Figure 6.3 (f). Finally, the structure is released by etching the parylene layer in oxygen plasma asher (Figure 6.3 (g)). The release step takes a long time because of the slow lateral etch rate of parylene [16].

Figure 6.4 provides optical images of the layers after each lithography step. In (a), the polyimide platforms can be seen just before the nitride protection layer is deposited, with the wide platform used to create the Z-shaped supporting beams. The bonding pad and the bottom two electrodes are shown in (b), where they cover both ends of the platforms. The anchoring area etched in the sacrificial layer can be seen in (c) right above the bonding pad, and the final structure layer is shown in (d). Because the trenches and the platforms have different fields of depth, two images were merged to provide a unified view in (c) and (d).

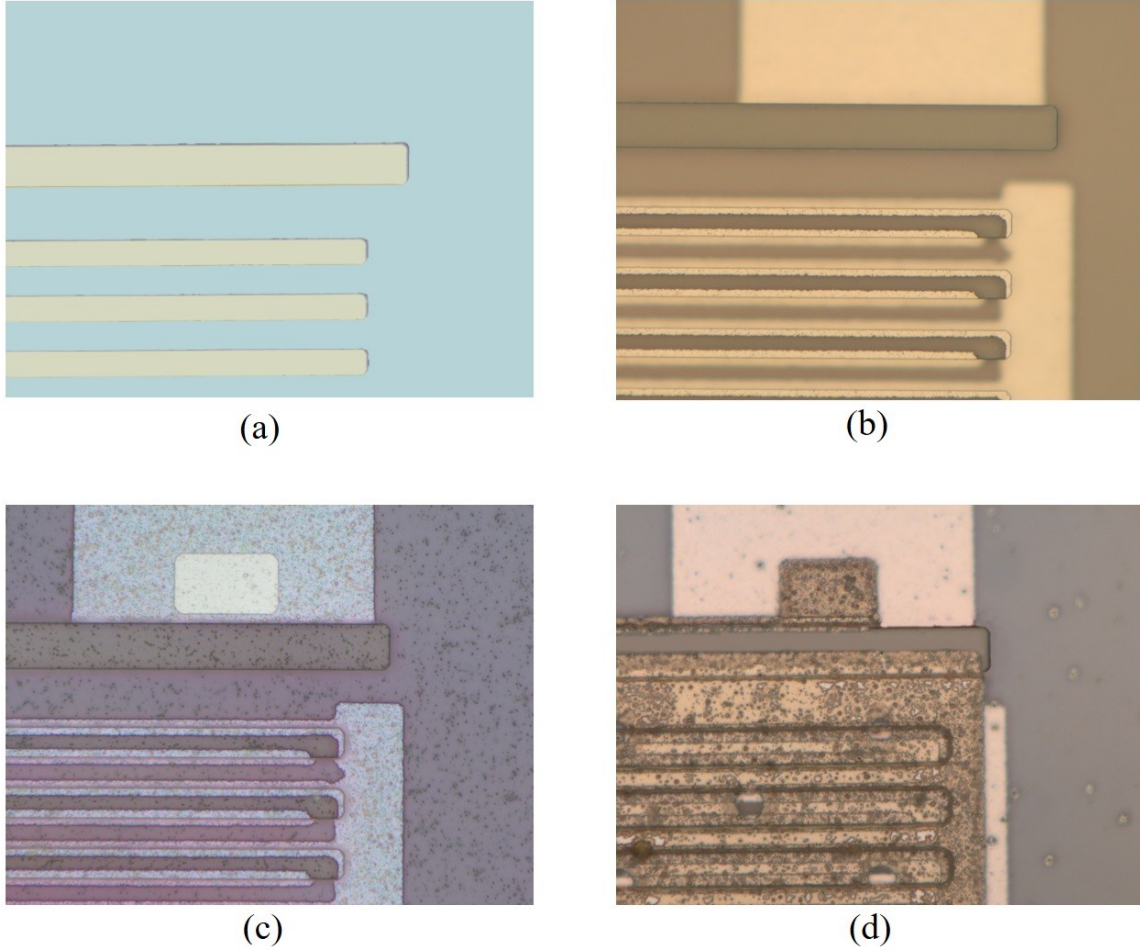


Figure 6.4: Optical images showing the different layers after each lithography step.

#### 6.4 Resolving Fabrication Challenges and Issues

As the devices were fabricated using the preliminary process flow, some issues were faced that caused device malfunction or underperformance. They were solved systematically and consecutively, resulting in the above process flow. Below is a discussion of some of these issues. This discussion clarifies that the real challenge in solving fabrication problems is to find the cause and not to create the solution. It also clarifies the motive behind some layer or values in the described process flow.

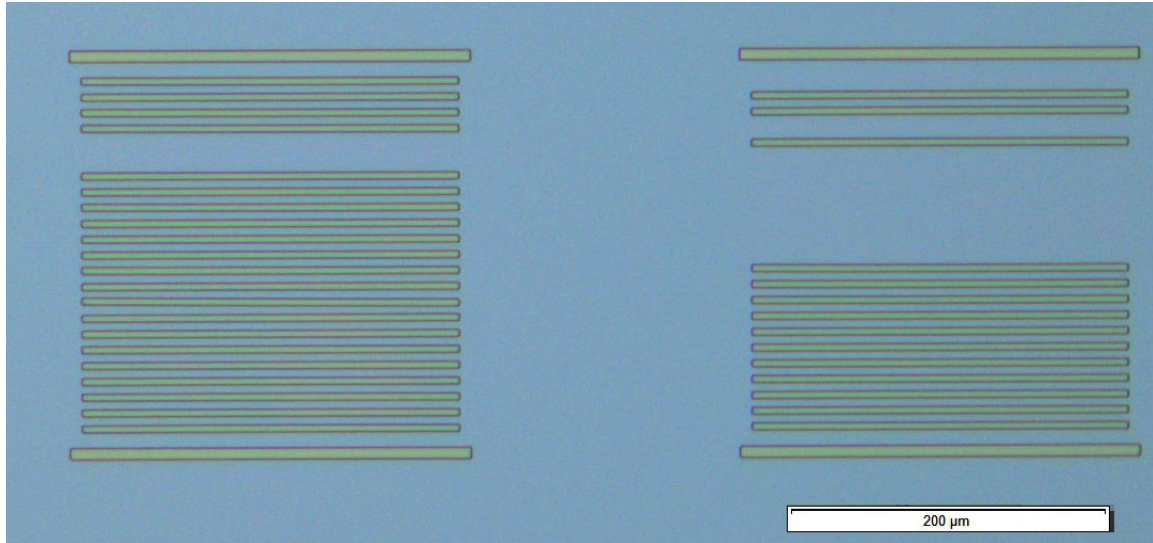


Figure 6.5: Optical image of devices with detached platforms.

#### 6.4.1 Platforms Detaching and Unwanted Etching

Initially, the polyimide layer was applied directly to the wafer, followed by a 50-nm silicon nitride protection layer. Since the platform widths are small, the connection area for each platform to the wafer was reduced, while the platform itself maintained a considerably large side area. To keep them attached to the wafer during different fabrication steps, the platforms' orientation was a main design consideration in the accelerometer's layout drawing step. They were placed in a direction parallel to the fluids' spreading out direction to reduce the force applied to them and also to prevent photoresist

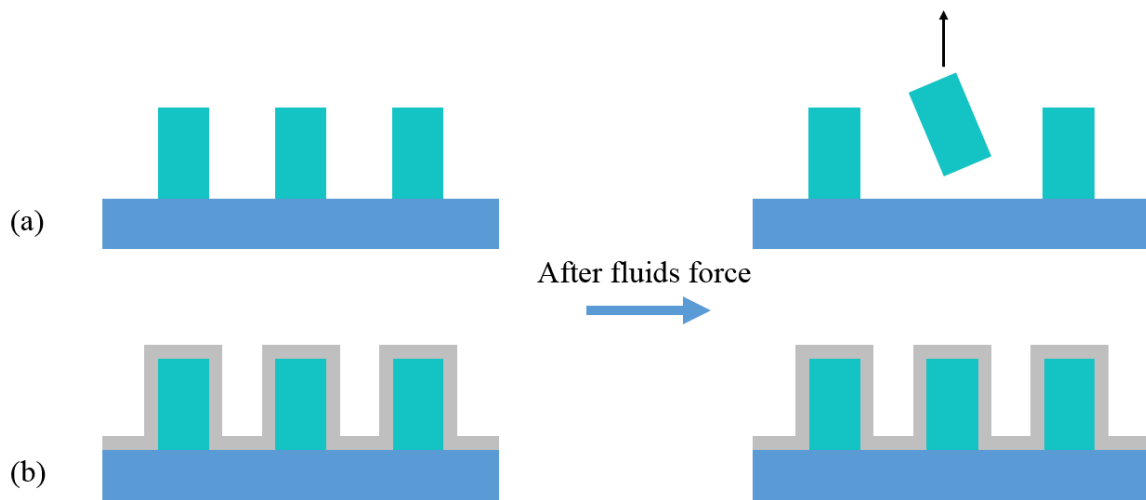


Figure 6.6: Air gun or fluids force effect on platforms (a) without, and (b) with a connection enhancement layer.

wedging. However, this was not effective in some steps, resulting in some platforms detaching (Figure 6.5). In some cases, the platforms were even etched in the final release step in some parts of the wafer, which indicated that the silicon nitride layer did not cover the entire wafer due to the short deposition time.

To enhance the polyimide connection to the wafer, a VM-652 adhesion promoter was applied to the entire wafer and left for 60 seconds before spinning it at 2500 rpm. It was then baked at 125 °C for 60 seconds on the hot plate before applying the polyimide. In addition, the thickness of the silicon nitride protection layer was increased from 50 nm to 300 nm to keep the platforms intact and ensure coverage of the wafer. This layer provided a continuous rigid connection between the platforms and the wafer in all directions (Figure 6.6). Those two steps provided decent results, and the platforms stayed attached even after going through the air gun drying or spin rinse dry steps.

#### 6.4.2 Unetched Structural Layer on the Platforms' Sidewalls

Because the structural silicon nitride is deposited conformally, its patterning step needs to etch higher thicknesses on the sidewalls of the platforms. There are two approaches to do this. The first is to add a planarization sacrificial layer to make the thickness equal everywhere, as reported by Cicek and Elsayed [20, 21]. The other option is to etch for a longer time until the sidewall layer is etched entirely. The first option adds an extra photolithography step and, if polyimide is used for planarization, the bottom electrode aluminum layer needs to be protected with another material, e.g. chromium. The long-time etch option requires protection for the layers exposed after etching silicon nitride, as the fluorine RIE step will continue to etch those areas if they are not exposed properly. Since the goal here was to simplify the process, the second option was adopted to avoid the extra deposition and print steps.

Figure 6.7 shows the time needed to etch different parts of the silicon nitride structural layer. Above the platforms and in the trenches, the etching time is proportional to the film thickness, i.e. 2  $\mu\text{m}$ . However, if the etch stops there, the film deposited on the sidewalls will remain unetched. The second step in etching the silicon nitride completely is to etch for extra time proportional to the platforms thickness. This etching step is of



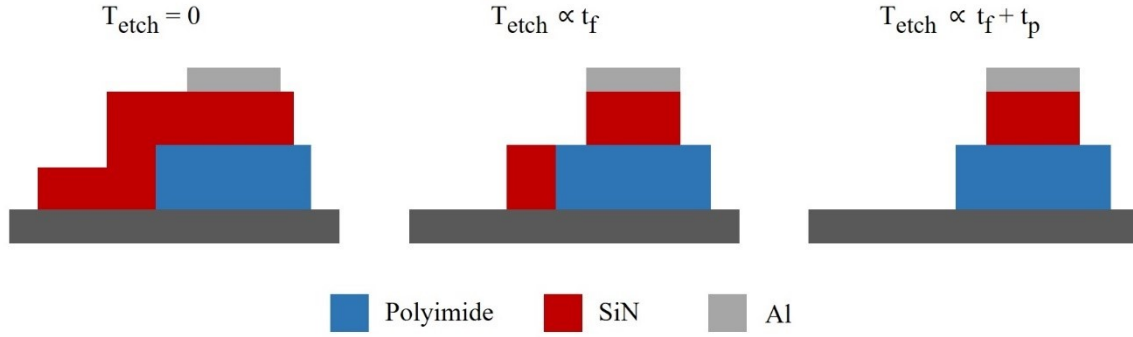


Figure 6.7: Silicon nitride formation on the platforms' sidewalls due to incomplete etch.

decisive importance and it must be verified before removing the hard mask and releasing the structure. Because this step is only time-controlled, it was challenging to verify that the structural layer deposited on the platforms' sidewalls was fully etched without using SEM images. Hence, the top electrode thickness was increased from initially 100 nm to 300 nm to work as a protection mask for the areas where silicon nitride was etched. Figure 6.8 depicts how the sidewalls were formed when the etching step fell short of complete removal of the sidewalls, and how it was solved with the extra etching time and the thicker protection mask.

Using metallic layers as hard masks in fluorine-based RIE has been reported to result in microroughness and micromasking problems. These are caused by the redeposition of hard mask molecules on the etched areas [22, 23]. Because aluminum is used here as a protection mask, the top mask was chosen to be aluminum as well instead

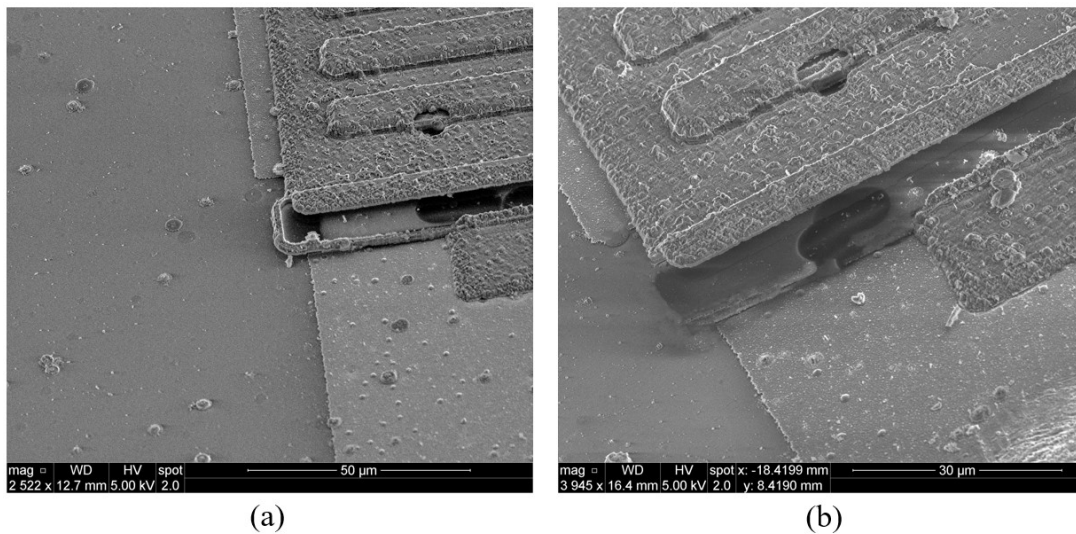


Figure 6.8: A platform with (a) un-etched, and (b) etched sidewalls.



of chromium, which has better selectivity. Thus, the redeposited microfilm, the protection mask, and the hard mask can be etched away in one step. It is also possible to use a hot bath of  $\text{H}_3\text{PO}_4$  acid to isotropically etch the silicon nitride film with a silicon dioxide hard mask [24]. However, the acid will also attack aluminum and cause CD degradation, thereby requiring some changes in the process and layout design rules.

#### 6.4.3 Increased Spacing on the Platforms and CD Degrade

Features' CD degradation is inevitable in this process; hence, the layout design must introduce enough tolerance for these differences. The degradation is caused by the masking photoresist UV exposure and development, and the isotropic etching of the metallic hard masks. Figure 6.9 (a) shows the bottom electrodes after being patterned using the Mask 1 photolithography step. The layout included a 3- $\mu\text{m}$  spacing between the two electrodes on top of the platform and a spacing of 5  $\mu\text{m}$  in the trench. The etched layer spacing in the trench had almost the same designed value after the isotropic etching step. However, the spacing on the platform increased by more than 50%, which could result in faulty devices if the alignment was not accurate. This issue was also noticed in the final patterning step, where the case worsened in the support beam which has less tolerance to misalignment as there is only between 1  $\mu\text{m}$  and 2.5  $\mu\text{m}$  overlap.

This problem was traced back and found to be caused by the thinner photoresist above the platform and the aluminum reflection of the UV light. A 1.4- $\mu\text{m}$  thick photoresist was originally used to pattern structures, but since the platforms are 2  $\mu\text{m}$  thick, the spun

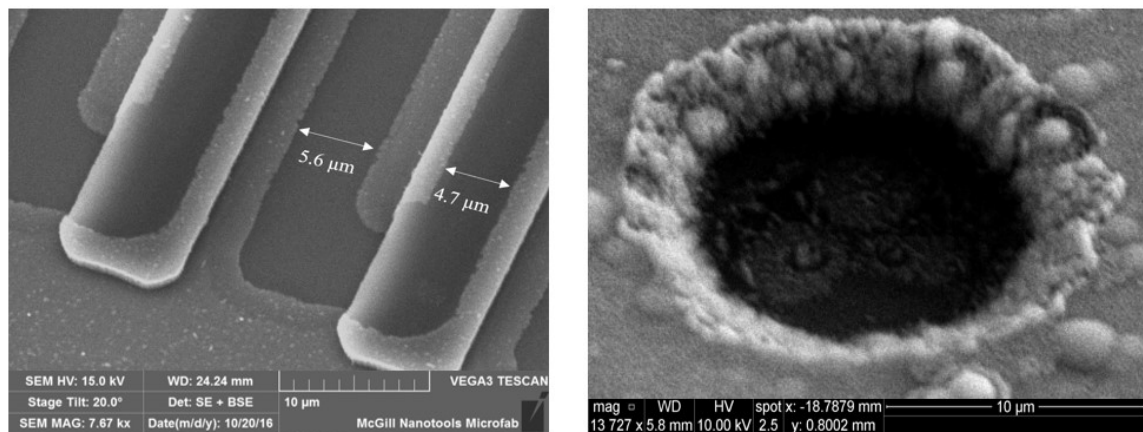


Figure 6.9: CD degradation in (a) electrodes spacing, and (b) structural layer holes.

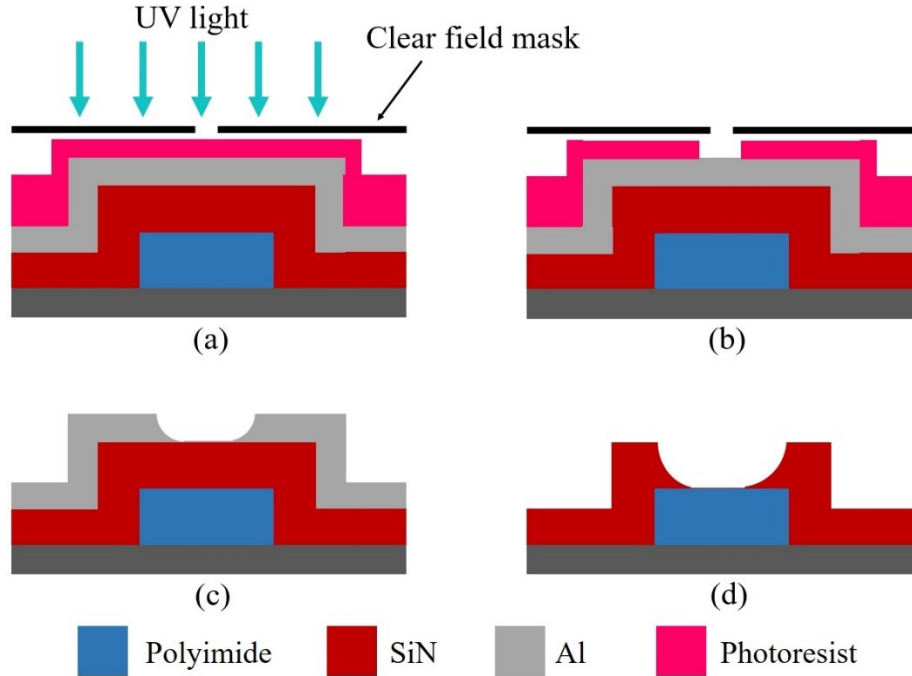


Figure 6.10: Degradation of dimensions in different steps.

photoresist on top of them was thinner than the photoresist in the trenches. The exposure dose customized for a 1.4- $\mu\text{m}$  thickness was too high for the thin layer of the photoresist on top of the aluminum on the platform. The aluminum's high reflectivity of the UV light caused the light to be scattered in the photoresist film. This exposed parts that were supposed to be dark, leading them to become soluble in the developer and resulting in the feature size retreat (Figure 6.10 (a) and (b)). To solve this problem, the photoresist thickness was increased to 2  $\mu\text{m}$ , leading to a thicker photoresist layer on the platform. Next, the UV dose was also optimized to reduce the overexposure effect on the platform while keeping it usable for the photoresist in the trenches. The photoresist developing and the isotropic aluminum etching time were also optimized to ensure that the required dimensions were as required by the end of this step. Even though this issue did not have a noticeable impact here since the electrodes were still formed, it will become challenging once the design is pushed to its maximum limits.

Figure 6.9 (b) shows the etched structural layer with its walls inclined from top to bottom. While this is not perilous in the formation of release holes, the stiffness of the supporting beams will be impacted by this change. In some cases where the beams were narrow, they were broken in the etching process. This pattern was created by the isotropic

wet etching of the aluminum hard mask that leaves thin edges and a vertical round cut. The thin edges are etched first, leading to a wider CD, and the round edge pattern is also transferred to the etched silicon nitride layer (Figure 6.10 (c) and (d)). To avoid this issue, a mask with higher selectivity to silicon nitride should be used. In this way, the hard mask would be thinner and the isotropic etching effect would be less notable.

## 6.5 Comparison with Other 3D Surface Micromachining Processes

Submicron gaps have been reported previously in different 2D and 3D surface micromachining processes. The main difference between the two approaches is that the gap is created using high-resolution lithography and directional etching in the 2D processes, and using a sacrificial layer in the 3D processes. This sacrificial layer adds at least one layout lithography step, which increases the process complexity. On the other hand, 2D processes require lithography and directional etching tools capable of reaching the targeted gap. Table 6.3 compares the process developed in this research to other recent state-of-the-art processes with submicron capacitive gaps. One common feature of the 3D processes is their ability to reach much lower gaps than the 2D processes can. As seen in the table, the process described in this chapter uses non-conductive materials to build a capacitive gap while the all others require conductive materials, which limits the choices

Table 6.3: Comparison of proposed process parameters to other recent works.

	Layer 1	Capacitive height ( $\mu\text{m}$ )	Sacrificial material	Gap (nm)	Release type	No. of masks	$T_{\text{max}}$ ( $^{\circ}\text{C}$ )	CMOS compatible
	Layer 2							
[25]	Poly-Si	2	$\text{SiO}_2$	68	Wet	6	1050	✗
[26]	Poly-Si	2	$\text{SiO}_2$	100	Wet	5	650	✗
	Gold							
[4]	SiGe	4	None <sup>1</sup>	500	Dry	3	450	✗
[27]	a-Si:H	3.2	None <sup>1</sup>	400	Wet	3	250	✓
[20, 21]	$\text{SiC}^2$	1.9	Parylene-C	100	Dry	7	200	✓
This work	Polyimide <sup>2</sup>	1.9	Parylene-N	300	Dry	4	300	✓
	$\text{SiN}^2$							

<sup>1</sup>: These are 2D processes where the gap is formed by direct patterning of the conductive layer.

<sup>2</sup>: Aluminum layers were used to create one or both electrodes in these processes.

or raises the thermal budget of the process. The capacitive height here can be increased if the sputtered aluminum covers the platforms sidewalls. The gap created in this process is relatively wide because it was chosen by design, as explained in the last chapter. Narrower gaps can be created if needed, with no alteration in the process steps except for a longer release time. Another distinctive feature of this process is the limited number of masks required compared to other 3D processes.

## **6.6 Process Improvement by Changing its Parameters**

Intuitively, performances can be enhanced by increasing the capacitive areas, which is controlled by the polyimide platform thickness. The PI 2555 polyimide used here provides about 3.8  $\mu\text{m}$  layer thickness when spun at 2000 rpm for 30 seconds [19]. Spinning at lower speeds will result in a thicker layer, but there will be areas with non-uniform thicknesses on the wafer. To create thicker uniform polyimide layers, spinning speeds higher than 3000 rpm are preferred. For future application with thicker platforms, the use of other polyimide grades is recommended, e.g. PI 2525 or 2574. To obtain layers with thicknesses lower than 5  $\mu\text{m}$ , these grades have to be mixed with a polyimide thinner chemical, e.g. the T-9039. It is also possible to use photosensitive polyimides to avoid the need for the aluminum hard mask, but the polyimide may not have straight sidewalls because of the standing-waves effect [28].

By increasing the platform thickness, the succeeding deposition steps should be optimized to ensure good step coverage on the platforms. Usually, the step coverage in the CVD process is good, but the step coverage depends on the process parameters regarding the sputtering and the PECVD systems [28]. Creating the metallic layers using the sputtering system runs higher risks of film discontinuity, because of their thin films. Furthermore, a shadowing effect may occur at the bottom of the platforms, unless careful attention is paid. If the sputtering system employs a collimator, it is recommended to use it when the aspect ratio of the features or platforms is higher than 4:1 [29]. The PECVD-deposited silicon nitride protecting the polyimide platforms and insulating the electrodes encounters challenges similar to the ones associated with the sputtering system, since these layers are also thin. It is possible to use other materials as sacrificial layers if they could be deposited conformally then dry etched, e.g. silicon which can be etched using  $\text{XeF}_2$ .

Regarding the top structural silicon nitride layer, the constraints relax because of the layer thickness. Increasing the thickness of this layer will create a larger proof mass, which will increase the sensitivity but will create larger vertical deflections. It is recommended to add the planarization layer when the combined thickness of the proof mass and platforms is larger than 6  $\mu\text{m}$ . This will reduce the etching time and the hard mask and stopper thicknesses. Moreover, it will also preserve the actual dimensions that degrade due to the isotropic etching of the hard masks at the cost of an additional photolithography step.

## 6.7 Conclusion

This chapter has introduced a 3D surface micromachining process. The process is CMOS-compatible and can be used to create narrow lateral gaps, as demonstrated in the previous chapter. Besides capacitive accelerometers, various other MEMS devices require narrow gaps for sensing, actuation, or both. Such devices can be built concurrently using the MEMS-last approach to create a hybrid MEMS and IC chip, e.g. a microcontroller with MEMS inertial sensors and resonators. An example of these devices is disk resonators, which require narrow gaps to generate deformations in the disk and to sense it. Another application example is flexural mode gyroscopes. Such devices were not fabricated here since they fall outside of the scope of this research. The process was completed using only four materials and four lithography steps, making it very simple compared to other similar processes. If this process is to be implemented on top of an IC, it is viable to use silicon nitride to mask the polyimide instead of aluminum. This will protect the IC exposed aluminum pads when the polyimide aluminum hard mask is removed.

## 6.8 References

- [1] F. Nabki, K. Allidina, F. Ahmad, P.-V. Cicek, and M. N. El-Gamal, "A highly integrated 1.8 GHz frequency synthesizer based on a MEMS resonator," *IEEE Journal of solid-state circuits*, vol. 44, no. 8, pp. 2154-2168, 2009.
- [2] H. Weinberg, "Dual axis, low g, fully integrated accelerometers," *Analog Dialogue*, vol. 33, no. 1, pp. 23-24, 1999.
- [3] H. Xie and G. K. Fedder, "A CMOS z-axis capacitive accelerometer with comb-finger sensing," in *Micro Electro Mechanical Systems, 2000. MEMS 2000. The Thirteenth Annual International Conference on*, 2000, pp. 496-501: IEEE.

- [4] A. R. Chaudhuri, S. Severi, M. A. Erismis, L. Francis, and A. Witvrouw, "SiGe MEMS accelerometers combining a large bandwidth with a high capacitive sensitivity," *Procedia Engineering*, vol. 47, pp. 742-745, 2012.
- [5] E. P. Quévy, S. A. Bhavé, H. Takeuchi, T.-J. King, and R. T. Howe, "Poly-SiGe high frequency resonators based on lithographic definition of nano-gap lateral transducers," *Technical Digest IEEE Hilton Head*, pp. 360-363, 2004.
- [6] L. C. Shao, M. Palaniapan, L. Khine, and W. W. Tan, "Micromechanical resonators with submicron capacitive gaps in 2 &#x003BC;m process," *Electronics Letters*, vol. 43, no. 25, pp. 1427-1428, 2007.
- [7] W.-T. Hsu, J. R. Clark, and C.-C. Nguyen, "A sub-micron capacitive gap process for multiple-metal-electrode lateral micromechanical resonators," in *Micro Electro Mechanical Systems, 2001. MEMS 2001. The 14th IEEE International Conference on*, 2001, pp. 349-352: IEEE.
- [8] A. Cowen, B. Hardy, R. Mahadevan, and S. Wilcenski, "PolyMUMPs design handbook," *Memscap Inc*, vol. 13, 2011.
- [9] H. Huang *et al.*, "Effect of deposition conditions on mechanical properties of low-temperature PECVD silicon nitride films," *Materials Science and Engineering: A*, vol. 435, pp. 453-459, 2006.
- [10] L. Liu, W.-g. Liu, N. Cao, and C.-l. Cai, "Study on the performance of PECVD silicon nitride thin films," *Defence Technology*, vol. 9, no. 2, pp. 121-126, 2013.
- [11] O. Tabata, K. Kawahata, S. Sugiyama, and I. Igarashi, "Mechanical property measurements of thin films using load-deflection of composite rectangular membranes," *Sensors and actuators*, vol. 20, no. 1-2, pp. 135-141, 1989.
- [12] J. Laconte, D. Flandre, and J.-P. Raskin, *Micromachined thin-film sensors for SOI-CMOS co-integration*. Springer Science & Business Media, 2006.
- [13] H. Baltes, O. Brand, G. K. Fedder, C. Hierold, J. G. Korvink, and O. Tabata, *CMOS-MEMS: Advanced Micro and Nanosystems*. John Wiley & Sons, 2008.
- [14] P. Garrou, C. Bower, and P. Ramm, *Handbook of 3d integration: volume 1-technology and applications of 3D integrated circuits*. John Wiley & Sons, 2011.
- [15] C. A. Harper and E. M. Petrie, *Plastics materials and processes: a concise encyclopedia*. John Wiley & Sons, 2003.
- [16] E. Meng, P.-Y. Li, and Y.-C. Tai, "Plasma removal of Parylene C," *Journal of Micromechanics and Microengineering*, vol. 18, no. 4, p. 045004, 2008.
- [17] E. Meng and Y.-C. Tai, "Parylene etching techniques for microfluidics and bioMEMS," in *Micro Electro Mechanical Systems, 2005. MEMS 2005. 18th IEEE International Conference on*, 2005, pp. 568-571: IEEE.
- [18] T. Standaert *et al.*, "High-density plasma patterning of low dielectric constant polymers: A comparison between polytetrafluoroethylene, parylene-N, and poly (arylene ether)," *Journal of Vacuum Science & Technology A: Vacuum, Surfaces, and Films*, vol. 19, no. 2, pp. 435-446, 2001.
- [19] HD MicroSystems, "Product bulletin PI 2525, PI 2555 & PI 2574 " 2012.
- [20] P.-V. Cicek, "Platforms and techniques for integration of microsystems above integrated electronic circuits," Ph.D. dissertation, Dept. of Elec. and Comp. Eng., McGill University, 2016.

- [21] M. Elsayed, "Novel architectures for MEMS inertial sensors and resonators targeting above-IC integration," Ph.D. dissertation, Dept. of Elec. and Comp. Eng., McGill University, 2016.
- [22] M. Shearn, X. Sun, M. D. Henry, A. Yariv, and A. Scherer, *Advanced plasma processing: etching, deposition, and wafer bonding techniques for semiconductor applications*. Intech, 2010.
- [23] M. Tilli, T. Motooka, V.-M. Airaksinen, S. Franssila, M. Paulasto-Krockel, and V. Lindroos, *Handbook of silicon based MEMS materials and technologies*. William Andrew, 2015.
- [24] W. Van Gelder and V. Hauser, "The etching of silicon nitride in phosphoric acid with silicon dioxide as a mask," *Journal of the Electrochemical Society*, vol. 114, no. 8, pp. 869-872, 1967.
- [25] J. Wang, Z. Ren, and C.-C. Nguyen, "1.156-GHz self-aligned vibrating micromechanical disk resonator," *IEEE transactions on ultrasonics, ferroelectrics, and frequency control*, vol. 51, no. 12, pp. 1607-1628, 2004.
- [26] J. R. Clark, W.-T. Hsu, M. A. Abdelmoneum, and C.-C. Nguyen, "High-Q UHF micromechanical radial-contour mode disk resonators," *Journal of microelectromechanical systems*, vol. 14, no. 6, pp. 1298-1310, 2005.
- [27] A. Gualdino, J. Gaspar, V. Chu, and J. P. Conde, "Sub-micron gap a-Si: H thin film Lamé-mode resonator processed at low temperature on a glass substrate," in *Solid-State Sensors, Actuators and Microsystems (TRANSDUCERS & EUROSENSORS XXVII), 2013 Transducers & Eurosensors XXVII: The 17th International Conference on*, 2013, pp. 1484-1487: IEEE.
- [28] S. Franssila, *Introduction to microfabrication*. John Wiley & Sons, 2010.
- [29] J. Sarkar, *Sputtering Materials for VLSI and Thin Film Device*. William Andrew, 2010.

---

# Chapter 7

## Conclusion

---

This research focused on the improvement of the design and fabrication of MEMS capacitive accelerometers for above-IC integration. This chapter concludes the thesis by presenting a summary of the performed research, along with insight into possible future developments and improvements.

### 7.1 Summary

This thesis described various methods to enhance and build above-IC capacitive accelerometers. Chapter 2 introduced a general overview of accelerometers' sensing mechanisms, applications, and their present markets, with a comprehensive focus on MEMS accelerometers. Chapter 3 then showed the optimization method of 2D capacitive accelerometers to produce the highest possible sensitivity within the device area for conventional designs. This optimization is done by finding the lengths of the sensing electrodes that maximize the performance given that there is a tradeoff between the sensing area and the mass within a certain area. Subsequently, the design of a dual-axis accelerometer fabricated in the MUMPs process was detailed in chapter 4. This novel design uses four proof masses and supporting beams to enable the sensing of the accelerations differentially and independently in two input axes perpendicular to each other. This design enables the cross-sensitivity between the sensing axes to be reduced, while maintaining decent sensitivity. The characterization and analysis of the performance were also discussed in details. Next, chapter 5 presented a novel 3D design of a single-axis differential capacitive accelerometer using a platform fabrication process. It also included the developed model for using the platforms to create supporting beams that are stiffer in the non-sensing axis to overcome the vertical narrow gap. Its performance characterization was discussed and compared to other conventional designs using 2D fabrication processes.



Finally, chapter 6 demonstrated a simple 3D fabrication process that can be used to fabricate different MEMS devices. The process was developed in a four-mask version, which meets the needs of devices with thin structural layers. The chapter also discussed possible process parameter changes and other potential MEMS applications for this process.

As outlined in chapter 1, the major contributions of this research are as follows: (i) an optimization method for 2D capacitive accelerometers, (ii) a novel design of a dual-axis accelerometer with low cross-axis sensitivity in a commercial process, (iii) a novel design of a high-sensitivity 3D capacitive accelerometer, and (iv) a CMOS-compatible 3D fabrication process for above-IC MEMS integration.

## **7.2 Future Development**

This research aimed to develop simple and efficient solutions to build high-sensitivity capacitive accelerometers. As the research progressed, new ideas and possible improvements arose, but they were not investigated as this would have been beyond the scope of the project. Nevertheless, they remain appealing for consideration in future research projects.

### **7.2.1 2D Single-Axis Capacitive Accelerometers**

The single-axis accelerometer design process was optimized to its limits in the described methodology. Nevertheless, some design aspects can still be adjusted to meet the application requirements or the available readout circuitry specifications. For example, the sensing fingers' width is affected by the applied electrical potential, and the fingers should be stiff enough to resist bending and collapsing towards each other. In the designs investigated in this study, values with safe margins were used, but they could still be lowered to improve the accelerometer outputs.

### **7.2.2 2D Dual-Axis Capacitive Accelerometers**

The dual-axis accelerometer showed reasonable performance, but its sensitivity-to-area ratio was low due to the large unused area. To improve this, the unused area could be exploited by adding a vertical sensing axis and making it a tri-axis accelerometer. To do

this, the process must be changed to enable differential sensing in lateral and vertical directions. The capacitive gap also needs to be reduced to enable the accelerometer size to be decreased while maintaining performance. Moreover, the proof mass and the number of sensing combs must be further optimized. A prime process candidate is the fully tri-axis differential process patented by El-Gamal et al. [1].

### 7.2.3 3D Single-Axis Capacitive Accelerometers

The design used in this research takes into consideration the challenges emerging from reaching the minimum achievable dimensions in the UV lithography process. A minimum overlap and clearance value of 3  $\mu\text{m}$  was used, even though it would have been feasible to go to 2  $\mu\text{m}$  using the same mask resolution and process. Thus, a larger number of platforms and more flexible supporting beams could be created by reaching the mask and process minimum resolutions. This would enable the building of accelerometers with even higher sensitivities, or the creation of NEMS accelerometers with 100 nm side dimensions. Moreover, if both the accelerometer design and fabrication process are improved, bioMEMS and bioNEMS applications could be further developed, e.g., accelerometer usage in cardiology [2]. Another improvement with great potential would be to add feedback electrostatic electrodes on some platforms. This would increase the range and the linearity of the accelerometer, at the cost of partially reduced sensitivity or increased area.

### 7.2.4 3D Fabrication Process

While the four-mask 3D fabrication process described in the previous chapter provides satisfactory performance, there still is room for improvements and changes to that process. For example, the sacrificial layer material is one aspect of the process that has room for improvement. Using a CVD-deposited parylene layer enabled the release of the devices in a CMOS-compatible step, i.e. the oxygen plasma etching. The inconsistent deposited thickness of parylene, however, may affect the final performance, especially for large-scale production. One solution to solve this problem would be to calibrate the devices in the test phase using a feedback system in the readout circuit, which may introduce more complexity to the system. Another solution could be adopted if CMOS compatibility is not

needed or if the IC area is completely protected by a passive layer, e.g. the nitride layer that protects the polyimide platforms. In that solution, other materials could be used as sacrificial layers. The most important characteristic of such materials would be their ability to be etched using dry etching methods to prevent the stiction of the top layer.

Because the sacrificial material is covered by other layers, the etching process must be isotropic. Winters et al. showed that xenon difluoride ( $\text{XeF}_2$ ) can be used to etch silicon isotopically at relatively high etch rates [3]. This dry etching process is vacuum-based and does not require any plasma activation of the etching gas. To keep the thermal budget low, the silicon layer could be deposited using a PECVD process, where the layer thickness could be accurately controlled. The importance of this change would increase when the sacrificial layer thickness is below 100 nm, when used for example with resonators or NEMS accelerometers. The platforms step coverage would not be an issue here, since it would be the same system used to deposit the silicon nitride film. This process has high selectivity to all of the other materials used in the same process, namely silicon nitride, silicon carbide, and aluminum. By controlling the temperature in the chamber, sputtered titanium and tungsten layers could be used as sacrificial layers, which would widen the choice of materials.

### 7.3 References

- [1] E.-G. Mourad, M. Elsayed, P.-V. Cicek, and F. Nabki, "Microelectromechanical bulk acoustic wave devices and methods," U.S. Patent 20,140,230,547 Aug 21, 2014.
- [2] V. Gemignani *et al.*, "Assessment of cardiologic systole and diastole duration in exercise stress tests with a transcutaneous accelerometer sensor," in *Computers in Cardiology, 2008*, 2008, pp. 153-156: IEEE.
- [3] H. Winters and J. Coburn, "The etching of silicon with  $\text{XeF}_2$  vapor," *Applied Physics Letters*, vol. 34, no. 1, pp. 70-73, 1979.

---

# Appendix A

## Characterization and Test Setup of the Capacitive Accelerometers

---

### A.1 Introduction

There are two main methods to measure the outputs of capacitive accelerometers: closed-loop and open-loop systems. In closed-loop systems, the sensed signal is fed to a circuit that controls actuators that reposition the proof mass to almost the rest state and determines the input acceleration by using the control signal value (Figure A.1) [1, 2]. These systems are suitable for high-range applications. Moreover, they demonstrate better linearity and can use the feedback to reduce the BNEA to a minimum, when the accelerometer needs to be operated in vacuum-sealed packaging. The drawback of these systems is that they need the device to include actuation parts, which increases the device's size. They also consume more power, and require higher headroom voltage in the circuit and more complicated control circuitry. Some of these limitations can be reduced or

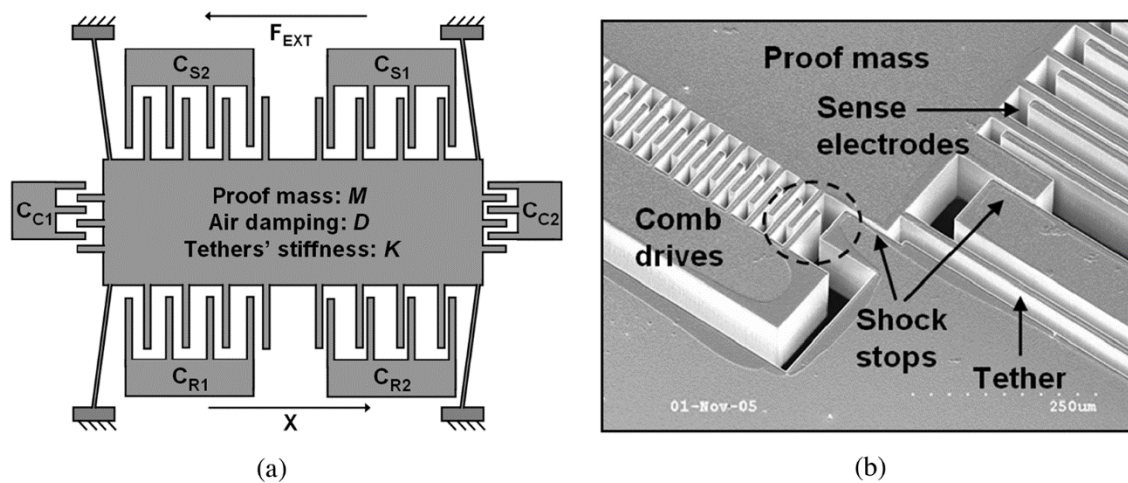


Figure A.1: Closed-loop capacitive accelerometer (a) simplified model and (b) SEM image [1].

eliminated by adopting digital circuits. Open-loop systems, on the other hand, detect the position of the proof mass displacement and convert the capacitance change to voltage. They have a simpler design in terms of the MEMS device layout and sensing circuit, and they usually yield decent results for applications that do not require high accelerations or bandwidth. Yet, they suffer from the sensitivity-linearity tradeoff, and they might also need to be tuned to adjust for MEMS fabrication changes to deliver the required performance [2-4].

The capacitance is the amount of electric charge stored between two conductive plates sandwiching a non-conductive medium. To measure that charge, it is transferred to a circuit where it is converted to a form that can be measured. The most common method to sense the differential capacitance in open-loop systems is to apply different voltages at the inputs of the two capacitors and to measure the resulting voltage in their common point after amplifying it [5-8] (Figure A.2). Even though this method can provide a customized solution for each specific design, different gains for different works make it impossible to compare one work to another when the sensitivity, for example, is reported in mV/g. This issue was considered when this characterization setup was being designed and built to make it possible to compare the results to other works and to commercial accelerometers with known performances.

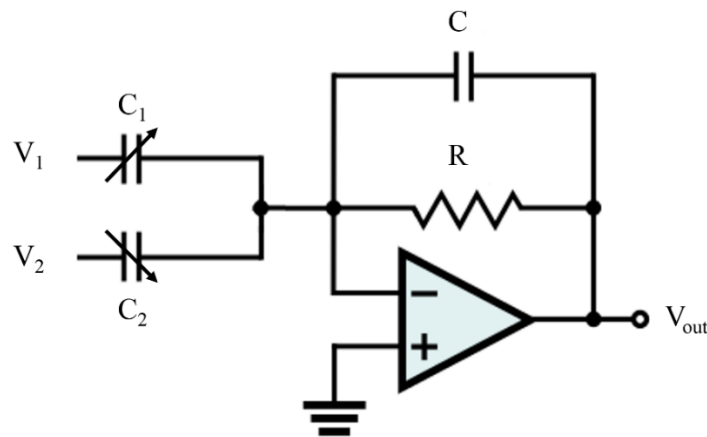


Figure A.2: Differential capacitance amplifying circuit.

## A.2 System Overview

Few methods are used to simulate acceleration on the device under test (DUT). Many companies in the industry use an electrodynamic shaker that moves vertically due to an oscillating signal. It can be used to simulate low-g vibrations and test the resulting bandwidth. However, such a setup is costly and more suitable for large manufacturers. Unlike the electrodynamic shaker, a motion simulator can be used to apply a fixed acceleration while the data is read. This enables the collection of as many data as needed at a given acceleration, whereas the electrodynamic shaker keeps reversing the acceleration direction because of its operation principle. Figure A.3 shows how the rotatory motion simulator can be used to simulate the acceleration by applying a centripetal force,  $F_c$ , on the DUT [9]:

$$F = ma_c = mr\omega^2, \text{ and} \quad (\text{A.1})$$

$$a_c = r\omega^2. \quad (\text{A.2})$$

where  $a_c$  is the simulated acceleration,  $m$  is the proof mass,  $r$  is the rotation radius, and  $\omega$  is the angular velocity.

The electromagnetic interference (EMI) can distort the electric field around the sensing capacitors in the CDC, leading to unstable or even incorrect readings. The rotary motion simulator uses a direct-drive brushless motor that reduces EMI but does not eliminate it. Thus, the design should include protection against EMI to ensure that the CDC is operated at the required electromagnetic compatibility (EMC) levels [10]. The first

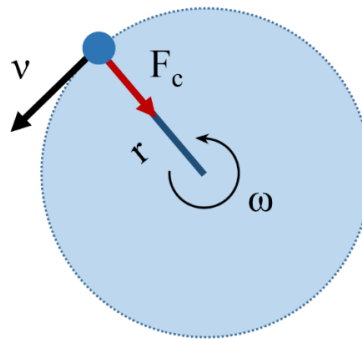


Figure A.3: Centripetal force resulting from rotary motion.

option was to design an external filter according to the AD7746 application note [11]. However, that design would not protect the DUT that is also a capacitive sensor and needs protection from EMI. Moreover, the characterization is made at atmospheric pressure and a humidity tolerance that changes the capacitor's relative permittivity,  $\epsilon$ . In addition, air waves resulting from the rotation movement could distort the results if the DUT was open to air. The optimal solution was to use a small Faraday cage setup that covered the PCB area where the chips and the DUT were located.

Figure A.4 (a) shows the block diagram and a photo of the system. It consists of an Aerotech ARMS-200 single-axis rotary motion simulator, with arms that hold two

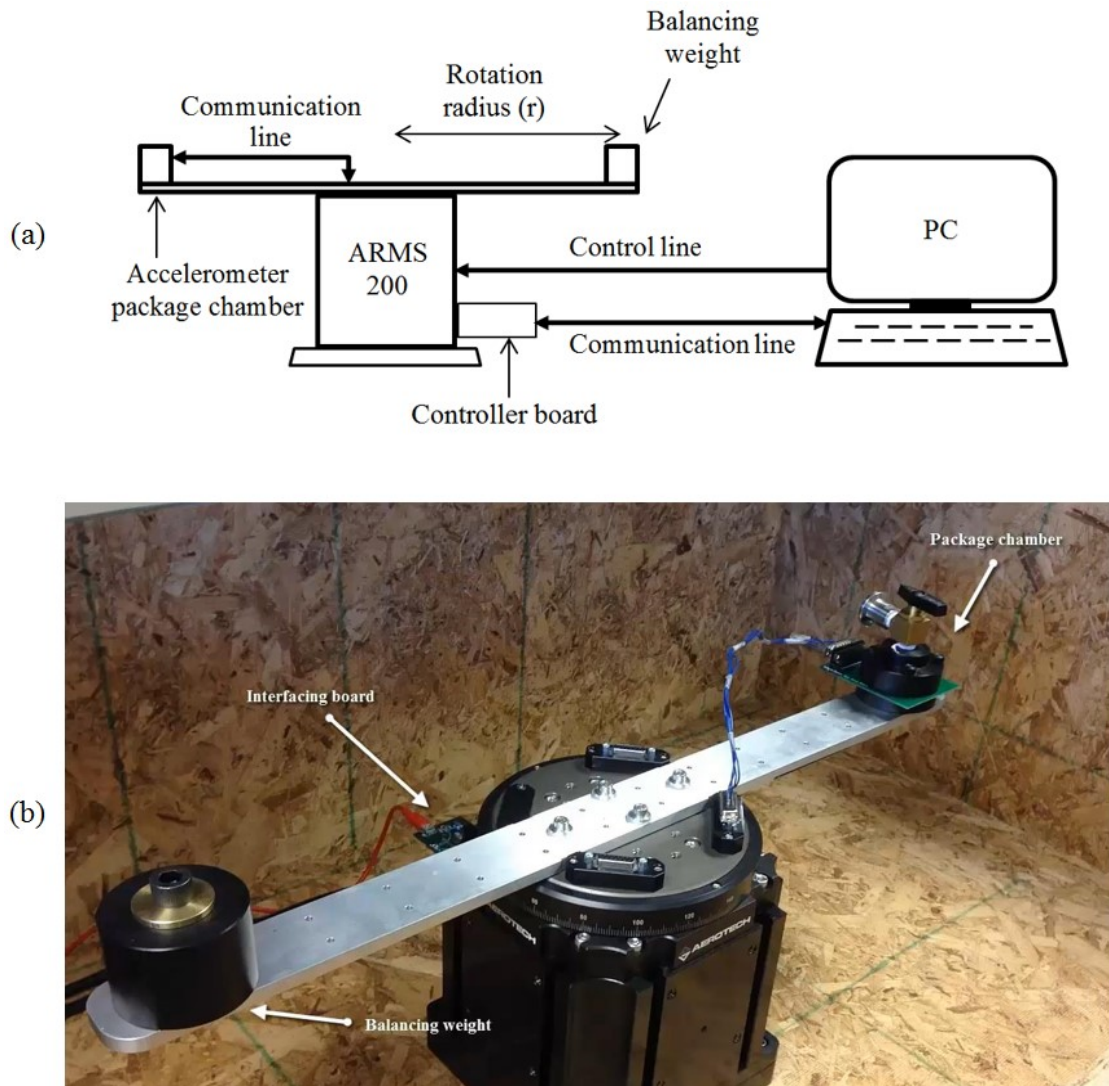


Figure A.4: The characterization system (a) block diagram and (b) photo.

chambers (Figure A.4 (b)). This simulator has a resolution of  $0.002^\circ/\text{s}$ , which translates to  $0.1\text{ }\mu\text{g}$  when a 30-cm arm is used. The DUT is on a PCB located in one chamber (or a Faraday cage) at one end of the arm, while a counter weight that keeps the motion simulator arm balanced is placed on the other end. The rotating stage is controlled by a personal computer (PC) via a control line. An Arduino Uno microcontroller board was selected to control the setup and initiate all the communications with the computer and the characterization chips.

### A.3 System Design

The system consists of several parts, some of which were provided by the part supplier, e.g. the rotary motion simulator. However, the communications and logging tool, the PCB design, data filtering, and the controller code had to be customized to automate and test the DUT as required. A detailed description of those parts and the reasoning behind their design or selection is given below.

#### A.3.1 PC Communications and Logging Tool

The PC uses serial protocol to communicate with the Arduino controller. There are multiple ways to display the output and log it. The *Serial Plotter* included in the Arduino programming environment was used, but it can plot only one variable and it does not log the received data for later processing. Matlab code was also used to communicate with the controller, but it is not the ideal solution since the user needs a more friendly and interactive interface for changing the chip register values initializing the communications. F. Farahbod has published an open-source Java tool that can be customized to communicate, plot, and log the data, and the end-user does not need to know any programming language to use it [12].

The tool was customized to display the filtered readout of the CDC and the three axes of the calibration accelerometer (Figure A.5). The CDC data reflects the reading from the X-axis input acceleration, and the sample rate was reduced to 10 Hz, since the conversion time used in the CDC is 122 ms. The received data from the CDC and the calibration accelerometer were logged continuously and used later for in-depth analysis of the performance.



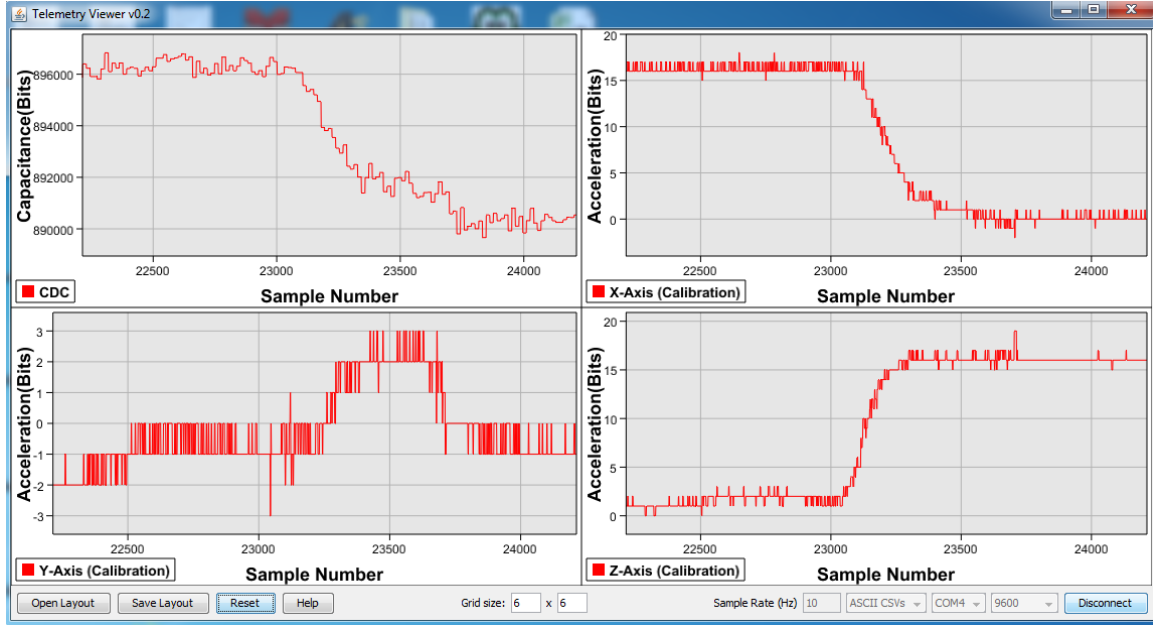


Figure A.5: Data display in the customized user interface.

The motion simulator could also be programmed to introduce the required acceleration for any specified interval. It was programmed to apply different acceleration values in multiple steps using the AeroBasic programming language [13]. This is helpful when different readouts are logged for later processing. However, it would be more convenient to set fixed acceleration and measure the output for each acceleration level individually.

### A.3.2 PCB Design

The main components of the PCB are the DUT, the CDC, and the calibration accelerometer. An mCube MC3216 state-of-the-art commercial 3-axis accelerometer was chosen to provide an accurate assessment of the fabricated accelerometers. It can reach 14-bit resolution for a maximum range of  $\pm 16$  g with less than  $200 \mu\text{g}/\sqrt{\text{Hz}}$  noise [14]. It can also communicate using the I<sup>2</sup>C protocol with the controller board. The AD7746 was selected as the CDC because it provides high resolution for differential capacitive changes down to 4 aF per LSB, with low  $2 \text{ aF}/\sqrt{\text{Hz}}$  output noise. Both chips share the same I<sup>2</sup>C communication lines to the controller. The PCB also includes a direct connection method to the fabricated accelerometer if a direct signal is needed. The passive components on the

PCB use the values recommended by chips manufacturers to condition the voltage signal or as pull-up resistors for the communication lines.

In the initial PCB design, the board was powered using the 3.3 V line from the Arduino board. The DUT was fixed inside an LLC package placed in a through-hole mounted chip carrier socket. This design led to an upsurge in the noise density of the CDC to values higher than the anticipated performance, making it impossible to read low capacitance changes. Consequently, the PCB components and layout were redesigned to create lower noise density. The new design feeds the 5 V line from the Arduino board to a high-accuracy 3.3 V regulator that powers up that PCB components [15]. The socket was replaced by pads with an electroless nickel immersion gold (ENIG) surface finish to enable direct wire bonding to the DUT.

All the components were placed on one side of the PCB to keep it flat at the bottom, thereby facilitating the wire bonding process. The calibration accelerometer and the DUT space were placed at the same level on the board to guarantee that both would undergo the same acceleration. The CDC also had to be as close as possible to the DUT to minimize the parasitic capacitances rising from the connection lines.

### A.3.3 Data Filtering

Since the DUT has low bandwidth and was tested at fixed acceleration, filtering the high-frequency noise resulting from the CDC would enhance the data quality. Depending on the sampling rate, the moving average and the median filtering methods were attempted to eliminate the noise, but they either introduced noticeable delays or resulted in underperformance. Next, a simplified version of Kalman filtering was used. This led to decent results after adjusting the filter parameters. The Kalman filter model used here was a simplified version of the original Kalman filter that is applied to scalar data. The model equations are listed below [16].

Time update equations:

$$\hat{x}_k^- = \hat{x}_{k-1}, \text{ and} \quad (\text{A.3})$$

$$P_k^- = P_{k-1} + Q . \quad (\text{A.4})$$

Measurement update equations:

$$K_k = \frac{P_k^-}{P_k^- + R} , \quad (\text{A.5})$$

$$\hat{x}_k = \hat{x}_k^- + K_k(z_k - \hat{x}_k^-) , \text{ and} \quad (\text{A.6})$$

$$P_k = (1 - K_k)P_k^- . \quad (\text{A.7})$$

Figure A.6 shows how random acceleration data was filtered using the Kalman filter. As depicted, the CDC noise can be jittery but when the filter is optimized, satisfactory results are obtained. The initial values for  $P$ ,  $K$ , and  $x$  were 0.00155, 0.0644, and  $2^{24}/2$ , respectively. The used values for  $Q$  and  $R$  were set to  $1 \times 10^{-4}$  and 0.0225. These values were obtained using trial and error based on the best results from logged data analysis, and then the filter was included in the microcontroller code.

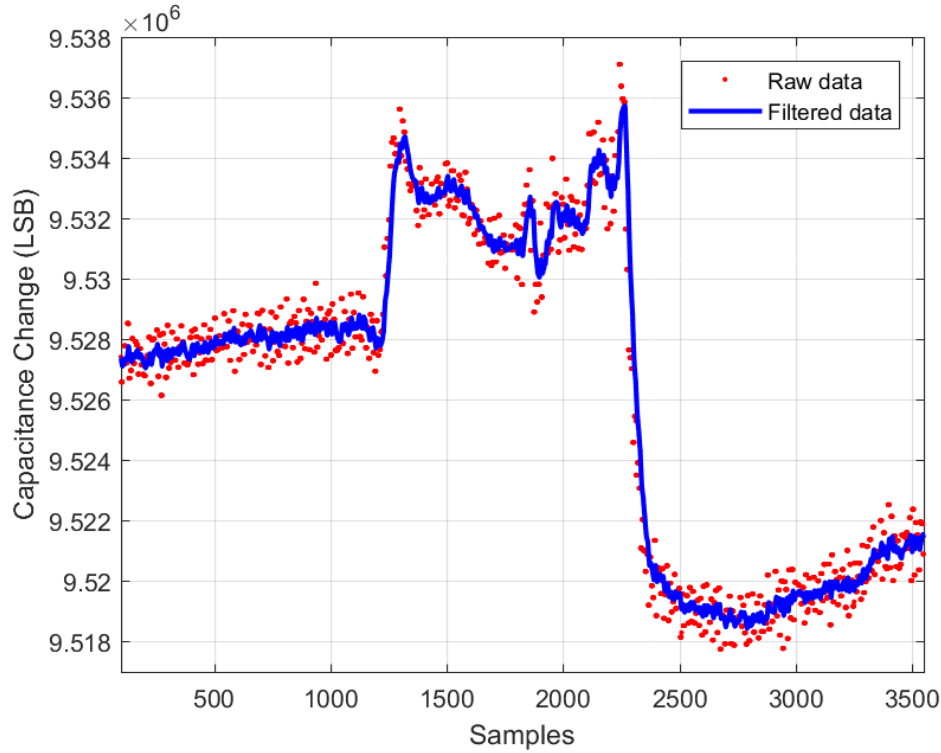


Figure A.6: Filtering the CDC data using the Kalman filter.

#### A.3.4 Arduino Code

The Arduino controller initiates the I<sup>2</sup>C communication as a master, while the other chips are slaves. The Arduino built-in I<sup>2</sup>C library does not support the “repeated start” function as specified in the protocol guidelines [17, 18]. While this does not represent an issue for most recent devices, AD7746 does not communicate correctly when that library is used. Hence, another community library that complies with the guidelines was used to communicate with both chips [19].

The Arduino code consists of two main parts: the setup and the loop. The setup is used to initialize the calibration accelerometer, and the CDC is executed once. In that step, the required settings and configuration registers are set to sense and send the values at specific resolutions and ranges (Table A.1). For example, to set the calibration accelerometer to read accelerations within a  $\pm 2$  g range at 14-bit resolution, a hex value of (0x05) is sent to the configuration register (0x20) at the accelerometer address (0x4C). The loop part continues to run as long as the controller is powered, and it reads the accelerometer and CDC outputs and sends them to the computer frequently via the Arduino controller. The CDC is reset before it begins the conversion process to verify ideal performance. To simplify the data display and logging step for later processing, the data is sent raw and then converted to gravitational acceleration units, i.e. g or  $9.81 \text{ m/s}^2$ . The used code is given below along with the used recursive functions and comments to clarify the steps.

Table A.1: Initialization values for the chip registers.

Chip	Register	Address pointer	Value
<i>AD7746</i> (0x48)	Cap setup	0x07	0xC0
	EXC setup	0x09	0x23
	Configuration	0x0A	0x39
<i>MC3216</i> (0x4C)	Mode control	0x07	0x01
	Output configuration	0x20	0x05

#### A.4 References

- [1] B. V. Amini, R. Abdolvand, and F. Ayazi, "A 4.5-mW Closed-Loop  $\Delta$  Sigma  $\Delta$  Micro-Gravity CMOS SOI Accelerometer," *IEEE Journal of Solid-State Circuits*, vol. 41, no. 12, pp. 2983-2991, 2006.
- [2] J. J. Allen, *Micro electro mechanical system design*. CRC Press, 2005.
- [3] P. Zwahlen *et al.*, "Open-loop and closed-loop high-end accelerometer platforms for high demanding applications," in *Position, Location and Navigation Symposium (PLANS), 2016 IEEE/ION*, 2016, pp. 932-937: IEEE.
- [4] M.-H. Bao, *Micro mechanical transducers: pressure sensors, accelerometers and gyroscopes*. Elsevier, 2000.
- [5] N. Yazdi, H. Kulah, and K. Najafi, "Precision readout circuits for capacitive microaccelerometers," in *Sensors, 2004. Proceedings of IEEE*, 2004, pp. 28-31: IEEE.
- [6] J. Wu, G. K. Fedder, and L. R. Carley, "A low-noise low-offset capacitive sensing amplifier for a 50- $\mu\text{g}/\sqrt{\text{Hz}}$  monolithic CMOS MEMS accelerometer," *IEEE Journal of Solid-State Circuits*, vol. 39, no. 5, pp. 722-730, 2004.
- [7] H. Rödjegård and A. Löf, "A differential charge-transfer readout circuit for multiple output capacitive sensors," *Sensors and Actuators A: Physical*, vol. 119, no. 2, pp. 309-315, 4/13/ 2005.
- [8] H. Leuthold and F. Rudolf, "An ASIC for high-resolution capacitive microaccelerometers," *Sensors and Actuators A: Physical*, vol. 21, no. 1-3, pp. 278-281, 1990.
- [9] R. A. Serway and J. W. Jewett, *Physics for scientists and engineers with modern physics*. Nelson Education, 2013.
- [10] Analog Devices Inc., "24-bit Capacitance-to-Digital Converter with Temperature Sensor, AD7745/AD7746," 2005.
- [11] H. Grothe and M. McCarthy, "EMC Protection of the AD7746," 2010.
- [12] F. Farahbod, "TelemetryViewer," *GitHub repository*, 2016.
- [13] Aerotech Inc. (2016). *Ensemble Motion Composer IDE*. Available: <https://www.aerotech.com/product-catalog/software.aspx>
- [14] mCube Inc., "MC3216 3-Axis Accelerometer," 2014.
- [15] Analog Devices Inc., "High Accuracy anyCAP™ 200 mA Low Dropout Linear Regulator," 2014.
- [16] N. Kovvali, M. Banavar, and A. Spanias, "An introduction to kalman filtering with matlab examples," *Synthesis Lectures on Signal Processing*, vol. 6, no. 2, pp. 1-81, 2013.
- [17] NXP Semiconductor, "The I2C-Bus Specification," 2014.
- [18] D. Paret and C. Fenger, *The I2C bus: from theory to practice*. John Wiley & Sons, Inc., 1997.
- [19] W. Truchsess, "Arduino I2C master library," *GitHub repository*, 2011.